Resonant Ultrasonic System Design, and Measurements of Critical Behaviour and Flux-Line Elasticity in High Temperature Superconductors.

by

Jørgen Nyhus

Thesis submitted in partial fulfillment of the requirements for the
Norwegian academic degree *Doktor Ingeniør.*

Department of Physics
Norwegian University of Science and Technology

August, 2000

Abstract

Design and construction of a resonant ultrasonic system based on the continues wave method by Bolef *et al.* (D. I. Bolef and J. G. Miller, Physical Acoustics Vol. **VIII**, 95 (1971)) is presented. The system is used for measurements of critical behaviour and flux-line lattice (FLL) elasticity in High temperature superconductors.

A theoretical background for the experimental method and the measurements is presented. This includes calculations of elastic constants for crystals of orthorhombic symmetry, theory of piezoelectric transducers, thermodynamic relations for elastic constants at a phase transition, the original theory of the continues wave method, elastic theory of flux lines in type-II superconductors, and a short review on the critical behaviour near the superconducting phase transition in High temperature superconductors.

Two ultrasonic measurement systems for measurements at low temperatures in magnetic fields up to 5 T have been constructed. The main system includes a two chamber cryostat inserted into a 5 T superconducting magnet, radio-frequency circuits, and computer programs controlling the measurements. The continues wave method has been extended to measurements on very small samples.

Single crystalline samples of $La_{1.85}Sr_{0.15}CuO_4$, $Bi_{2.2}Sr_{1.8}CaCu_2O_x$, and $Nd_{1.03}Ba_{1.97}Cu_3O_x$ have been characterized by magnetic susceptibility and magneto-optical measurements, prior to the ultrasonic measurements.

Calculations of the resonant behavior of the ultrasonic Transducer-Bond-Sample-Bond-Transducer composite including attenuation and bonding are made. The calculations explain features not encountered in the

original linear theory, with frequency pulling as the most apparent effect.

The apparatus is shown to have a frequency resolution less than $\Delta f/f \sim 10^{-8}$. The resolution of the actual experiments is lower than this due to problems with crystal quality, and the bonding. For measurements on $La_{1.85}Sr_{0.15}CuO_4$ the resolution in the relative change of elastic moduli with temperature was $\Delta C_{ii}/C_{ii} \sim 10^{-4} - 10^{-6}$. The absolute accuracy is in the $1 - 3$ % range.

Reflection measurements are shown to give detailed information of bond breaks or similar causes of failure.

Two crystals of $La_{1.85}Sr_{0.15}CuO_4$ have been extensively studied. The measurements of C_{33}, C_{44}, C_{55}, and C_{66} are consistent with similar published data measured on other $La_{2-x}Sr_xCuO_{4-y}$ crystals. The crystals have been detwinned by a uniaxial stress of approximately 4 MPa applied along the tetragonal [110]-axis during the measurements. A distinct minimum near T_c is observed for the first time in measurements of C_{44} and C_{55}. A minimum is also measured for C_{66} as observed earlier. The observed minimum is ascribed to critical fluctuations.

Critical scaling of the C_{33} data has been done. Consistency with 3D-XY critical exponents is shown.

The modulus C_{33} has been measured in the frequency range from 16 - 214 MHz. A signature of dynamic behavior near T_c is found. This has not been observed before and more investigations could give valuable information about the physics of the phase transition.

For the low temperature behavior of C_{33} in magnetic fields from 0 to 5 T parallel to the crystal c-axis, an elastic softening, linear in B-field, is observed. The phenomenon is not related to the elasticity of the FLL. A distinct explanation of the surprising effect was not yet found.

Attempts to measure the complete softening of the FLL shear modulus c_{66}^h at the melting transition were unsuccessful. It is argued that this is impossible to measure in the crystals available up to now.

Measurements of the FLL tilt modulus c_{44} at temperatures near T_c are consistent with published data and theories found in the literature. At low temperatures the measurements consistently show an extra stiffness, which is unexplainable by the linear elastic theory of the FLL.

Preface

This thesis is submitted to the Norwegian University of Science and Technology (NTNU) in partial fulfillment of the requirements for the Norwegian academic degree *Doktor Ingeniør*.

All the work has been carried out at the Department of Physics at NTNU. During my employment period, lasting from August 1996 to August 2000, I have also spent a total of one year taking courses and one year assisting in the teaching of undergraduate students. In addition to these 'duties' I have been the main supervisor of five project students and one diploma student in our lab. I have also partly supervised four other project student and two diploma students. I have been participating in two NATO ASI summer schools, in July 1996 and July 1998. The work which is presented here started in April 1997.

The results presented in the thesis have not yet been published. This is due to the fact that publishable results came first in the very end of the work period, mainly due to sample problems. One or two papers will be written based on results presented here. Some more measurements are needed to make some of the other results publishable. My colleague Ulrik Thisted will start this work in October this year.

Acknowledgments

First of all I would like to thank my supervisor Professor Kristian Fossheim. I would like to thank him for accepting me as a graduate student in his lab and for giving me the opportunity to go to two NATO ASI summer schools. I would like to thank him for a very challenging project and for always having time for me. I would also express deep gratitude for an incredible friendliness and for many good moments at his home and at his cottage. I am also grateful for corrections and comments to the thesis.

I will express my deep gratitude to Professor Takashi Suzuki for invaluable advice and collaboration. This work could not well have been accomplished without his experienced answers to my many questions. I will also thank Dr. Fumihiko Nakamura and Dr. Naoki Kikugawa for a fruitful collaboration.

The crystal growers Dr. Naoki Kikugawa, Dr. Thomas Wolf, Dr. Kunihiko Oka and Dr. Andreas Erb receive a special thank for the supply of single crystals. A special thank to Dr. Kikugawa for much valuable advice.

I would like to thank all the project and diploma student which I have fully or partly supervised; Mattias Ericsson, Håvard Alnes, Kristin Nergaar Berg, Inge Fløan, Axel Gjellestad, Sean Erik Foss, Kjartan Haugen, Mikkjell Rommetveit, Ivar Værnhus, Anders Frøseth and Rune Kristian Steinseth. They are all thanked for their contributions. It has been a pleasure to work with them. I will in particular thank Mattias Ericsson and Håvard Alnes for many inspiring discussions and important contributions to my work.

I would like to thank the technical staff at the Department of Physics, who have done very important work for me. A special thank to Arnolf Bjølstad and his excellent staff, Rolf Dahl, Kjell Ramsøskar, and Arne Moholt and his staff.

I would like to thank my colleagues and friends at the superconductivity research group, during the years, for many inspiring discussions and good moments. Dr. Sai Kong Chin, Dr. Anh Kiet Nguyen, Dr. John Ove Fjærestad, Joakim Hove, Sjur Mo, Ulrik Thisted, Dr. Oleg Ivanov, Dr. Kate Christova, Dr. Sun-Li Huang, Dr. Giuseppe G. N. Angilella, and Professor Asle Sudbø have all been important for me. Ulrik Thisted receives a special thank for his comments to the thesis.

I would like to thank Professor Tom Henning Johansen for providing the magneto optical films. There are also others to thank. Though not all are mentioned, nobody is forgotten.

In the end I would like to give my warmest thanks to my mother Turid, my father Sverre, my sister Kathrine, and to all my friends who have all given me support and much joy these years. A special thank to my friends in the Aikido club and the Tango club, and to my dear friend Snorre Farner.

Trondheim, August 2000

Jørgen Nyhus

Contents

Chapter 1

Introduction

The sensational discovery of superconductivity in a lanthanum based copper oxide perovskite, $La_{2-x}Ba_xCuO_4$, by Bednorz and Müller [1], marked the beginning of an exiting research area. The new materials were named High temperature superconductors (HTSs), due to their high transition temperatures. The materials were interesting not just because of their high T_c's, but they were clearly a completely new class of superconductors with great potential. The HTS materials all have characteristic copper oxide planes which are found to dominate the superconducting properties. In between the planes are ions like La, Y, Ba or Th which serve as charge reservoirs. The materials are, with very few exceptions, hole doped antiferromagnetic insulators which become metallic upon doping. There are different structural families of HTSs. Among the most studied are the La-214 materials exemplified by $La_{2-x}Sr_xCuO_4$ (LSCO), the 123 materials such as $YBa_2Cu_3O_{7-x}$ (YBCO), and the 2212 materials with $Bi_2Sr_2CaCu_2O_{8+x}$ (BSCCO) as an example. The HTSs all have either a tetragonal or an orthorhombic structure, often with structural transitions between the two. The degree of layerednes are very different in the different families and the anisotropy is doping dependent. Also the transition temperature changes with doping, being maximum at some optimal doping.

The high temperature superconductors have always been very interesting from a fundamental point of view. The work presented here is related to one of the bigger research fields; 'Vortex physics in high temperature superconductors'. Extensive reviews can be found in [2, 3, 4]. There is at present no accepted microscopic theory explaining high temperature superconductivity, but on the phenomenological level the anisotropic Ginsburg-Landau (GL) model [5] gives a good description. The HTSs have a very rich magnetic field versus temperature phase diagram compared to the classical superconductors. Depending on the anisotropy and the amount of pinning in the sample, many different phases have been suggested (see for example [4]). Much of the debate in the field has been on which of these are 'real' phases and of which order the transitions are, or if the transitions are just crossovers. Critical fluctuations in HTS materials is another subject of much debate, and likewise the melting of the flux-line lattice (FLL). These developments have given our motivation for building a system for measurements of elastic behavior of the FLL. A true determination of the physics of melting requires measurement of elastic properties.

Many experimental methods have been, and are still, used in the investigations of HTS materials. The work presented here involves ultrasonic measurements of elastic constants both for the superconductors and for the FLL. Ultrasonic measurements were among the most important methods used for the investigations of low temperature superconductors (LTS) and were also significant for the development of the BCS theory (see [6] and references therein). Ultrasonic measurements are interesting because they probe both static and dynamic aspects of structural and electronic properties. For HTSs also measurements of FLL elasticity have been done. Much work was put into ultrasonic investigations of HTSs in the late 80's and early 90's, mainly on polycrystalline samples, and mainly concentrated on structural phase transitions[7]. This was natural since the structure of the materials are so characteristic.

We have chosen a resonant ultrasonic method developed by Bolef *et al.* in the 1960's [8]. Resonance methods have generally very high resolution, and this together with the simple relations between resonances, phase velocities, and attenuation in the method made it seem like a good choice.

The outline of the thesis is as follows: In Chapter 2 we present the relevant theoretical background for the discussions of the ultrasonic method and for the experimental results presented later. Chapter 3 contain a rather detailed presentation of the single crystals we have investigated and the measurements systems we have built. In Chapter 4 experimental results are presented together with a detailed discussion of the ultrasonic method and our apparatus. We show measured results for the HTS crystals and discuss among other things critical behavior near T_c and elastic moduli for the FLL. The conclusions are given in Chapter 5.

Chapter 2

Theoretical background

For a deeper understanding of the measurements presented in the following chapters, several different theoretical aspects need to be investigated. The theories presented in this chapter should be understood as a reminder or a rough presentation. The presentation represent our own understanding of work done by others, nothing more. We have tried to use the same notation all trough out the thesis, and symbols are mainly explained in this chapter as they appear. Standard notations like Einstein's summation convention [9] will be used.

2.1 Elasticity and ultrasonics

2.1.1 Ultrasonics

Ultrasonics is the name given to the study and application of sound waves of frequencies higher than those to which the human ear can respond (about 16kHz)[1]. One can divide ultrasonics into two categories; one dealing with low amplitude vibrations, the other with high intencity. In the first category are areas like non destructive testing (NDT), medical diagnostics, and

---

[1] With 'sound' is usually understood longitudinal acoustic waves. Also transverse waves (in solids) are called ultrasound when they are in the same frequency range as longitudinal ultrasonic waves.

measurements of elastic constants. The first use of ultrasonics was made around the beginning of the 20th century[2]. Most of the early techniques were standing wave techniques. This changed after the developement of the radar during World War II. Pulse techniques took completely over, opening up many new areas. In NDT and elasticity measurements resonant techniques have experienced a revival in recent years. This is mainly due to the development of a technique called resonant ultrasound spectroscopy (RUS)[10, 11]. In elasticity measurements variations over the pulse echo technique, like the so called phase comparison method (PCM)[12, 13], have been shown to be very useful.

In most low amplitude ultrasonic techniques one is really just measuring the phase velocity, v, and/or the attenuation, α, in the medium under consideration. These informations are measured and presented in many different ways depending on what is interesting for the user. In a classical pulse-echo experiment v is determined by the time between successive (reflected) pulses and α can be deduced from the decay of the pulse height. A sketch of pulses as measured on an oscilloscope is shown in figure 2.1.

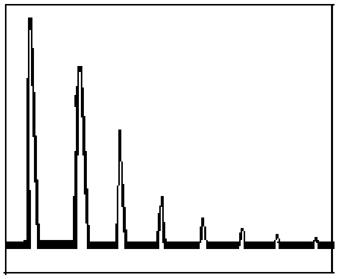

Figure 2.1: Sketch of pulses measured on an oscilloscope in a classical pulse-echo experiment.

---

[2] Examples are Galton's high-frequency whistle (1883) for testing the upper frequency response of the human ear, and Langevin's work on underwater soundings during World War I.

2.1.2 Hook's law and the elastic moduli

Under the assumption of small strains Hook's law states that the applied stress, σ_i, on a material is proportional to the resulting strain, ε_j:

$$\sigma_i = C_{ij}\,\varepsilon_j \quad i,j = 1..6 \tag{2.1}$$

The proportionality is represented by the elastic matrix containing 36 constants C_{ij} which are called elastic stiffness constants or moduli of elasticity. We will use the standard definitions for the numbers i and j:

$$1 \equiv xx; \quad 2 \equiv yy; \quad 3 \equiv zz; \quad 4 \equiv yz; \quad 5 \equiv zx; \quad 6 \equiv xy \tag{2.2}$$

The stress σ_4 $(= \sigma_{yz})$ denotes a force applied in the y direction to a plane whose normal lies in the z direction, and so on. The inverse relation of equation 2.1 also exist and is often used. The proportionality constants are then called the elastic compliances s_{ij}.

For a crystal of orthorhombic symmetry (Like the HTS crystals we have studied) there are nine independent elastic moduli:

$$\mathbf{C}^{ortho} = \begin{bmatrix} C_{11} & C_{12} & C_{13} & 0 & 0 & 0 \\ C_{12} & C_{22} & C_{23} & 0 & 0 & 0 \\ C_{13} & C_{23} & C_{33} & 0 & 0 & 0 \\ 0 & 0 & 0 & C_{44} & 0 & 0 \\ 0 & 0 & 0 & 0 & C_{55} & 0 \\ 0 & 0 & 0 & 0 & 0 & C_{66} \end{bmatrix} \tag{2.3}$$

HTS materials are often considered as quasi tetragonal since the a- and b-axis are of almost equal length. With $x = y$ (or $a = b$) $C_{11} = C_{22}$, $C_{13} = C_{23}$, and $C_{44} = C_{55}$. Thereby reducing the nine elastic moduli to six. For even higher symmetries this number is further reduced to five for the hexagonal symmetry, three for the cubic and two for isotropic materials.

Here we will look at propagation of elastic waves in orthorhombic crystals, extending a calculation given by Kittel [14] for the case of cubic symmetry. These calculations are the core of all elastic measurements using ultrasonic techniques. We have not found these calculations carried out for tetragonal or orthorhombic symmetries in the literature, so we will therefor give the detailed calculations here. The analysis treats infinitesimal strains only, and no distinction is made between isothermal and adiabatic deformations.

Imagine three orthonormal vectors $\hat{x}$, $\hat{y}$ and $\hat{z}$ embedded in the unstrained solid. After a uniform deformation of the solid the axes are distorted in orientation and length. The new axes $\vec{x}\,'$, $\vec{y}\,'$ and $\vec{z}\,'$ may be written in terms of the old axes as:

$$\begin{aligned} \vec{x}\,' &= (1+\tilde{\varepsilon}_{xx})\hat{x} + \tilde{\varepsilon}_{xy}\hat{y} + \tilde{\varepsilon}_{xz}\hat{z}\ ; \\ \vec{y}\,' &= \tilde{\varepsilon}_{yx}\hat{x} + (1+\tilde{\varepsilon}_{yy})\hat{y} + \tilde{\varepsilon}_{yz}\hat{z}\ ; \\ \vec{z}\,' &= \tilde{\varepsilon}_{zx}\hat{x} + \tilde{\varepsilon}_{zy}\hat{y} + (1+\tilde{\varepsilon}_{zz})\hat{z}\ . \end{aligned} \tag{2.4}$$

The coefficients $\tilde{\varepsilon}_{\alpha\beta}$ define the deformation; they are dimensionless and have values $\ll 1$. After such a uniform deformation a point (or atom) originally at $\vec{r} = x\hat{x} + y\hat{y} + z\hat{z}$ will be at the position $\vec{r}\,' = x\vec{x}\,' + y\vec{y}\,' + z\vec{z}\,'$. The displacement $\vec{u}$ of the deformation is defined by

$$\vec{u} \equiv \vec{r}\,' - \vec{r} = (x\tilde{\varepsilon}_{xx} + y\tilde{\varepsilon}_{yx} + z\tilde{\varepsilon}_{zx})\hat{x} + (x\tilde{\varepsilon}_{xy} + y\tilde{\varepsilon}_{yy} + z\tilde{\varepsilon}_{zy})\hat{y} + (x\tilde{\varepsilon}_{xz} + y\tilde{\varepsilon}_{yz} + z\tilde{\varepsilon}_{zz})\hat{z} \tag{2.5}$$

In a more general form the displacement is given by

$$\vec{u}(\vec{r}) = u(\vec{r})\hat{x} + v(\vec{r})\hat{y} + w(\vec{r})\hat{z}, \tag{2.6}$$

defining u, v and w which we will use in the definitions and calculations in the following. The symmetric strains are defined by

$$\varepsilon_{xx} \equiv \tilde{\varepsilon}_{xx} = \frac{\partial u}{\partial x}; \quad \varepsilon_{yy} \equiv \tilde{\varepsilon}_{yy} = \frac{\partial v}{\partial y}; \quad \varepsilon_{zz} \equiv \tilde{\varepsilon}_{zz} = \frac{\partial w}{\partial z}. \tag{2.7}$$

The non-symmetric strains are correspondingly defined by

$$\begin{aligned} \varepsilon_{xy} &\equiv \vec{x}\,' \cdot \vec{y}\,' \simeq \tilde{\varepsilon}_{yx} + \tilde{\varepsilon}_{xy} = \frac{\partial u}{\partial y} + \frac{\partial v}{\partial x}; \\ \varepsilon_{yz} &\equiv \vec{y}\,' \cdot \vec{z}\,' \simeq \tilde{\varepsilon}_{zy} + \tilde{\varepsilon}_{yz} = \frac{\partial v}{\partial z} + \frac{\partial w}{\partial y}; \\ \varepsilon_{zx} &\equiv \vec{z}\,' \cdot \vec{x}\,' \simeq \tilde{\varepsilon}_{zx} + \tilde{\varepsilon}_{xz} = \frac{\partial u}{\partial z} + \frac{\partial w}{\partial x}; \end{aligned} \tag{2.8}$$

The equations of motion in the x, y and z directions read:

$$\begin{aligned} x:\ \rho\frac{\partial^2 u}{\partial t^2} &= \frac{\partial\sigma_{xx}}{\partial x}+\frac{\partial\sigma_{xy}}{\partial y}+\frac{\partial\sigma_{xz}}{\partial z}\\ y:\ \rho\frac{\partial^2 v}{\partial t^2} &= \frac{\partial\sigma_{yx}}{\partial x}+\frac{\partial\sigma_{yy}}{\partial y}+\frac{\partial\sigma_{yz}}{\partial z}\\ z:\ \rho\frac{\partial^2 w}{\partial t^2} &= \frac{\partial\sigma_{zx}}{\partial x}+\frac{\partial\sigma_{zy}}{\partial y}+\frac{\partial\sigma_{zz}}{\partial z} \end{aligned} \tag{2.9}$$

Under the assumption that the total torque on any unit volume must be zero it follows that

$$\sigma_{yz}=\sigma_{zy};\quad \sigma_{zx}=\sigma_{xz};\quad \sigma_{xy}=\sigma_{yx} \tag{2.10}$$

Equations 2.9 combined with Hooks' law (Eq. 2.1) in the case of orthorhombic symmetry then reads

$$\begin{aligned} x:\ \rho\frac{\partial^2 u}{\partial t^2} &= C_{11}\frac{\partial\varepsilon_{xx}}{\partial x}+C_{12}\frac{\partial\varepsilon_{yy}}{\partial x}+C_{13}\frac{\partial\varepsilon_{zz}}{\partial x}+C_{55}\frac{\partial\varepsilon_{zx}}{\partial z}+C_{66}\frac{\partial\varepsilon_{xy}}{\partial y}\\ y:\ \rho\frac{\partial^2 v}{\partial t^2} &= C_{12}\frac{\partial\varepsilon_{xx}}{\partial y}+C_{22}\frac{\partial\varepsilon_{yy}}{\partial y}+C_{23}\frac{\partial\varepsilon_{zz}}{\partial y}+C_{44}\frac{\partial\varepsilon_{yz}}{\partial z}+C_{66}\frac{\partial\varepsilon_{xy}}{\partial x}\\ z:\ \rho\frac{\partial^2 w}{\partial t^2} &= C_{13}\frac{\partial\varepsilon_{xx}}{\partial z}+C_{23}\frac{\partial\varepsilon_{yy}}{\partial z}+C_{33}\frac{\partial\varepsilon_{zz}}{\partial z}+C_{44}\frac{\partial\varepsilon_{yz}}{\partial y}+C_{55}\frac{\partial\varepsilon_{zx}}{\partial x} \end{aligned} \tag{2.11}$$

Using the definitions for the strains Eq. 2.7 and 2.8 gives us the final tree relations:

$$\begin{aligned} \rho\frac{\partial^2 u}{\partial t^2} &= C_{11}\frac{\partial^2 u}{\partial x^2}+C_{66}\frac{\partial^2 u}{\partial y^2}+C_{55}\frac{\partial^2 u}{\partial z^2}+(C_{12}+C_{66})\frac{\partial^2 v}{\partial x\partial y}+(C_{13}+C_{55})\frac{\partial^2 w}{\partial x\partial z}\\ \rho\frac{\partial^2 v}{\partial t^2} &= C_{66}\frac{\partial^2 v}{\partial x^2}+C_{22}\frac{\partial^2 v}{\partial y^2}+C_{44}\frac{\partial^2 v}{\partial z^2}+(C_{12}+C_{66})\frac{\partial^2 u}{\partial x\partial y}+(C_{23}+C_{44})\frac{\partial^2 w}{\partial y\partial z}\\ \rho\frac{\partial^2 w}{\partial t^2} &= C_{55}\frac{\partial^2 w}{\partial x^2}+C_{44}\frac{\partial^2 w}{\partial y^2}+C_{33}\frac{\partial^2 w}{\partial z^2}+(C_{13}+C_{55})\frac{\partial^2 u}{\partial x\partial z}+(C_{23}+C_{44})\frac{\partial^2 v}{\partial y\partial z} \end{aligned} \tag{2.12}$$

With piezoelectric transducers (discussed in section 2.1.3) one can send longitudinal (L) or transverse (T) waves into the material. Plane wave propagation along the crystal principal axes can be described mathematically as follows below. We will use the notation

$$L_\alpha:\quad \vec{k}||\vec{u}||\alpha;\quad T_{\alpha\beta}:\quad \vec{k}||\beta\quad \vec{u}||\alpha \tag{2.13}$$

Here $\vec{k}$ is the wave vector, $\vec{u}$ the displacement vector, and $\alpha,\beta=x,y,z$. Using the [100]-plane as an example we get

$$L_x: u=u_0e^{i(kx-\omega t)};\quad T_{yx}: v=v_0e^{i(kx-\omega t)};\quad T_{zx}: w=w_0e^{i(kx-\omega t)} \tag{2.14}$$

Similar expressions for [010] (y) and [001] (z) follow in a straightforward manner.

Which elastic moduli that will be measured by which applied stress wave is then found by combining the equations 2.12 with the 'transducer equations' 2.13. One example is given here, the rest are shown in table 2.2. Substituting $w = w_0 e^{i(kz-\omega t)}$ into the last equation in 2.12 gives $\omega^2 \rho = C_{33} k^2$, thus the velocity ω / k of the longitudinal wave along the [001] direction is:

$$v_{33} = (C_{33}/\rho)^{1/2} \tag{2.15}$$

Similar simple relations (of the form $v_{ii} = (C_{ii}/\rho)^{1/2}$) can be found for all the symmetric elastic moduli, as shown in table 2.2. To measure non-symmetric elastic moduli (C_{ij} with $i \neq j$) waves have to be sent along other axes like the [110]- or [111]-axis. This will in general not probe only one elastic moduli, but a combination of two or more [14]. In solids phase velocities are typically of the order of km/s and elastic moduli typically in the GPa range. For a given solid material longitudinal phase velocities are typically twice as high as the transverse ones.

2.1.3 Piezoelectricity and transducers

Acoustic waves are generated and received by a device called a transducer; this converts energy from one form to another. There are various kinds of transducers working in different frequency intervals. These include: Crystal oscillators (utilizing the piezoelectric effect), Magnetostrictive oscillators, purely mechanical generators and receivers (like whistles and sirens), electromagnetic transducers, electrostatic transducers, ultra high frequency transducers and thermal, chemical and optical transducers. Here we will take a short look at the piezoelectric effect and the $LiNbO_3$ (lithium niobate) transducers used in the experiments. For further information about transducers we will refer to the literature [15, 16].

The piezoelectric effect[3] occurs in crystals having one or more polar axes, or generally lacking a center of symmetry. A slab or disc of such a

---

[3] First discovered by the Curie brothers in 1880

crystal, cut with its parallel surfaces normal to a polar axis, will on subjecting it to a mechanical stress build up equal and opposite electrical charges on the parallel surfaces. The converse effect is also present so piezoelectric transducers are said to be reversible. Some materials which are not piezoelectric in the paraelectric state can be made to act as piezoelectrics by cooling them from above their Curie temperature in the presence of a strong electric field. We will not distinguish between the two in the following.

A transducer is made from a piezoelectric crystal by attaching electrodes to the parallel surfaces. Because the piezoelectric effect can occur only when opposite charges appear on the electrodes only odd harmonics can be generated. See figure 2.2.

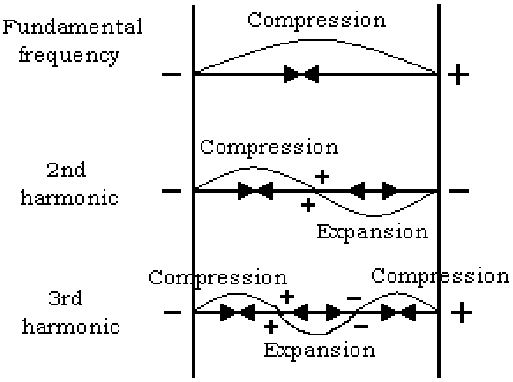

Figure 2.2: The first three harmonics of a piezoelectric transducer. Opposite charges appear on the electrodes only for odd harmonics.

Piezoelectricity can be described by combining elasticity and electrostatics according to the Onsager relations[15]:

$$\begin{aligned} D_i &= d_{ih}\sigma_h + \epsilon_{ij}E_j; \\ \varepsilon_h &= s_{hk}\sigma_k + d_{ih}E_i \end{aligned} \tag{2.16}$$

Here E_i and D_i are the electric field and the electric displacement in the i-direction, and ε and σ are the strain and stress fields. Equations 2.16 define the following material parameters: The electric permittivity ϵ_{ij}, the elastic compliance s_{ij}, and the piezoelectric strain constants $d_{ih} = d_{hi}$. Eliminating the stress in the equations above, and dropping tensor notation for convenience, gives:

$$D = Sd/s + \epsilon E(1 - d^2/\epsilon s) \equiv e\varepsilon + \epsilon E(1 - k_c^2) \tag{2.17}$$

Here $e \equiv d/s$ is called the piezoelectric stress constant. More important is $k_c \equiv d^2/\epsilon s$ the electro-mechanical coupling factor, which is a measure of the efficiency of the transducer. If W_m is the mechanical energy stored in the transducer when an applied force produces a strain and W_e is the electrical energy supplied to the transducer, then [15]:

$$W_m/W_e = k_c^2 \tag{2.18}$$

In our experiments we have used so called 41° X-cut (Shear) and 36° Y-cut (quasi longitudinal) $LiNbO_3$ transducers from Valpey Fisher. All data needed about the transducers are taken from Valpey Fisher's home pages on the Internet [17]. In table 2.1 some useful characteristics of $LiNbO_3$ transducers are listed.

The transducer crystals have fundamental frequencies which are inversly proportional to the thickness of the crystals. The proportionality constants can be found in [17].

Calculations of transducer responce for a single transducer or as a part of an ultrasonic system, is most conveniently done using equivalent circuits. Two types are needed for the discussions in following sections. The simplest equivalent circuit is a lumped circuit like the one shown in figure 2.3. This is based on the equation of motion of a forced 'spring';

$$M\frac{d^2x}{dt^2} + R_m\frac{dx}{dt} + \frac{1}{C_m} = F \tag{2.19}$$

Table 2.1: Characteristics of $LiNbO_3$ transducer crystals

Density (g/cm^3):	4.64
crystal class:	Rhombohedron

Orientation	*Wave type*	Wave speed	Coupling factor
36^o Y-cut	Quasi-longitudinal	7340 m/s	0.485
Z	Longitudinal	7316 m/s	0.162
41^o X-cut	Shear	4795 m/s	0.684
10^o Y-cut	Quasi-shear	4271 m/s	0.436

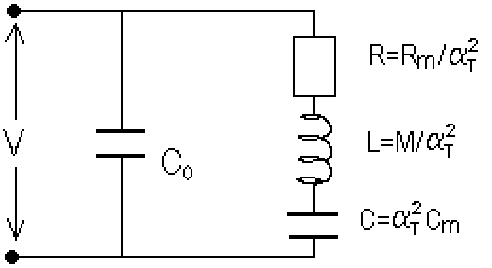

Figure 2.3: Lumped circuit equivalent of a ultrasound transducer. Symbols are explained in the text.

or equivalently an RLC circuit as shown in the figure. Here M is the oscillating mass equivalent to the induction L, R_m the mechanical resistance and C_m the inverse of the spring constant. The capacitance C_0 in figure 2.3 is due to the transducer itself acting as a plate capacitor. The constant α_T in figure 2.3 is termed the transformation factor and is given by the following relation between the area, A, the thickness, l, and the piezoelectric stress constant, e, of the transducer:

$$\alpha_T = Ae/l \tag{2.20}$$

The lumped circuit is convenient in defining quantities like resonance frequency and quality factor (also called Q, Q-factor or Q-value). The transducer has two different Q-factors, one mechanical and one electrical.

The other kind of equivalent circuit we will use is a transmission line equivalent as shown in figure 2.4. The figure is shown here only for illustration. Details of the circuit can be found in [16]. The transmission line equivalent is most useful for transient analysis of the transducer behavior. Assuming a sinusoidal applied voltage the transducer crystal will, in

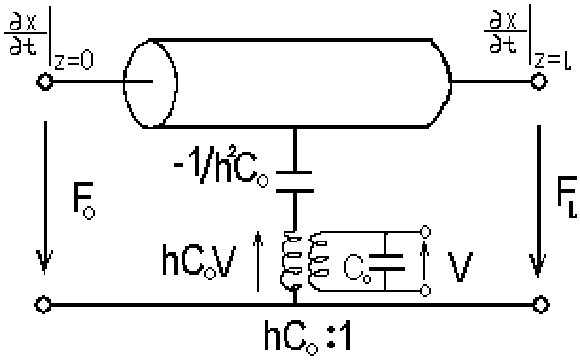

Figure 2.4: Transmission line equivalence circuit of a piezoelectric transducer. The transducer has one electrical and two mechanical ports. Details can be found in [16].

the case of longitudinal waves, contract and expand sinusoidally. This is equivalent to stating that elastic waves are traveling backward and forward inside the disc, and hence the transducer acts like a mechanical transmission line. We will return to transmission lines and this mechanical equivalent in section 2.2.1 and 2.2.2.

2.1.4 Relations between heat capacity and elastic moduli

We have not come across a general theory for the relationships between the heat capacity, the thermal expansion coefficients and the elastic moduli for a material. What is known for sure is that the three are connected, and also as we will show, that there exist relations between them under special conditions. We are mainly concerned with the temperature dependences of the three quantities and also how they change under a phase transition.

Depending on the approximation used and the physical situation, one can split the change of elastic constants that takes place at a phase transitioninto two parts: Mean field contributions and fluctuations. We will in section 2.3.3 argue that a mean field description is sufficient for describing low temperature superconductors (LTS) whereas fluctuations are important for describing HTS.

L. R. Testardi published in 1975 a general theory describing how thermal expansion heat capacity and elastic moduli were related at a continuous phase transition [18]. The key idea was to assume that the difference in Gibbs free energy per mole between the high temperature phase and the low temperature phase could be expressed as follows:

$$\Delta G \equiv G^H(T) - G^L(T) = \sum_i \phi_i(\sigma) f_i[T/T_c(\sigma)], \tag{2.21}$$

where the general function ϕ depended on the stress, and $f_i[T/T_c]$ were normalized so that $f_i(0) = 1$ and $f_i(1) = 0$. The value $G^H(T)$ is the extrapolated value expected if the material had not gone trough the phase transition[4].

---

[4] E.g. still in the normal phase in the case of superconductors

Using standard thermodynamic relations and assuming all ϕ_i to be equal the difference in thermal expansion were calculated to be[18]:

$$\Delta\tilde{\alpha} = -\left(\frac{d\ln T_c}{d\sigma}\right)\Delta C_p + \left(\frac{d\ln\phi}{d\sigma} - \frac{d\ln T_c}{d\sigma}\right)\Delta S \qquad (2.22)$$

Here C_p is the specific heat at constant stress and S is the entropy. The isothermal longitudinal and high-symmetry shear elastic compliances were:

$$\Delta s_L = \left(\frac{d\ln T_c}{d\sigma}\right)^2 T\Delta C_p - AT\Delta S - \left(\frac{1}{\phi}\frac{d^2\phi}{d\sigma^2}\right)\Delta G \qquad (2.23)$$

with

$$A = \left[\frac{2d\ln T_c}{d\sigma}\frac{d\ln\phi}{d\sigma} - 2\left(\frac{d\ln T_c}{d\sigma}\right)^2 + \frac{1}{T_c}\frac{d^2T_c}{d\sigma^2}\right] \qquad (2.24)$$

and

$$\Delta s_s = -\left(\frac{1}{T_c}\frac{d^2T_c}{d\sigma^2}\right)T\Delta S - \left(\frac{1}{\phi}\frac{d^2\phi}{d\sigma^2}\right)\Delta G \qquad (2.25)$$

We have measured elastic moduli and not elastic compliances. As explained by Testardi and also used by Nohara *et al.*[19] the longitudinal elastic moduli can similarly be expressed as follows:

$$\Delta C_{ii}(T) = \left(\frac{d\ln T_c}{d\varepsilon_i}\right)^2 \frac{T\Delta C_p(T)}{V_{mol}} - AT\Delta S(T) + \left(\frac{1}{\phi}\frac{d^2\phi}{d\varepsilon_i^2}\right)\Delta F(T) \qquad (2.26)$$

where $i = 1, 2, 3$ and

$$A = \left[\frac{2d\ln T_c}{d\varepsilon_i}\frac{d\ln\phi}{d\varepsilon_i} - \left(\frac{d\ln T_c}{d\varepsilon_i}\right)^2 + \frac{d^2\ln T_c}{d\varepsilon_i^2}\right] \qquad (2.27)$$

Here $\Delta F = -\phi(\varepsilon_i)f[T/T_c(\varepsilon_i]$ is the Helmholtz type free energy difference between the two phases. V_{mol} is the molar volume. For pure transverse elastic moduli, labeled Γ;

$$\Delta C_\Gamma(T) = \left(\frac{1}{T_c}\frac{d^2T_c}{d\varepsilon_\Gamma^2}\right)T\Delta S(T) + \left(\frac{1}{\phi}\frac{d^2\phi}{d\varepsilon_\Gamma^2}\right)\Delta F(T) \qquad (2.28)$$

These relations are reduced to the Ehrenfest relations [19, 20] at T_c.

Testardi's theory does not exclude fluctuations. One might in place of T_c use a temperature T_0 where the extrapolated high temperature value splits of from the measured low temperature value, and let ΔC_p, ΔS, and ΔG contain the necessary description of the fluctuations[18].

For HTSs Millis and Rabe [21] made a theory very similar to the one by Testardi, where a more detailed description of fluctuations were included. By approximating the free energy by its most singular part;

$$F_s(T,\varepsilon) = \frac{A^{\pm}}{\alpha}\left[\frac{|T-T_c(\varepsilon)|}{T_c(\varepsilon)}\right]^{2-\alpha} + ... \tag{2.29}$$

the following expression was calculated for the change of high symmetry longitudinal elastic moduli due to fluctuations:

$$\Delta C_{ii}^{fl}(T) = -A^{\pm}{\frac{d\ln T_c}{d\varepsilon_i}}^2 \frac{(2-\alpha)(1-\alpha)}{\alpha}\left[\frac{T}{T_c}-1\right]^{-\alpha}, i = 1,2,3 \tag{2.30}$$

In the two previous equations α is the critical exponent for the specific heat, and $A^{\pm}$ is some amplitude above (+) and below (-) T_c. Nohara *et al.* extended these calculations to high symmetry shear elastic moduli [22]:

$$\Delta C_{\Gamma}^{fl}(T) \propto -\Delta C_p \frac{d^2T_c}{d\varepsilon_{\Gamma}^2}\frac{2-\alpha}{\alpha}\left[\frac{T}{T_c}-1\right]^{1-\alpha} \tag{2.31}$$

We will use the expressions presented in this section, in the following chapters, when discussing measured data.

2.2 Continous wave resonant ultrasonics

2.2.1 Transmission line theory

A bit simplified Maxwell's equations can be classified into three regions when comparing the wave length of the electromagnetic waves with the system sizes. If the wavelength is much smaller than the system we are in the optical regime where geometrical optics apply. In the other extreme we have the lumped circuit theory of Kirchhoff with frequencies from kHz to zero (DC). In between wavelengths are comparable with the system sizes, which means there are significant phase variations over the system. The intermediate region can, as the two others, be further split into smaller regions. Relevant here is the radio frequency (RF) region and parts of the microwave region, with typical frequencies in the megahertz (MHz) range.

Lumped circuit theory can in general not be used when working with high frequencies. Field analysis can in principal always be done, but is often too difficult. Bridging this gap is a theory called transmission line theory. A transmission line is a distributed parameter network, where voltages and currents can vary in magnitude and phase over its length[23]. We will very briefly look at a few relevant concepts for the further discussions.

The typical model for a transmission line (for TEM waves[5]) is a two wire line of length Δz as shown in figure 2.5a. The lumped-element equivalent circuit, figure 2.5b, has a resistance R, induction L, conductance G and capacitance C per unit length.

From Kirchhoff's laws in the limit $\Delta z \rightarrow 0$ one can find the transmission line equations[23] for the voltage $v(z,t)$ and current $i(z,t)$:

$$\frac{\partial v(z,t)}{\partial z} = -Ri(z,t) - L\frac{\partial i(z,t)}{\partial t} \tag{2.32a}$$

$$\frac{\partial i(z,t)}{\partial z} = -Gv(z,t) - C\frac{\partial v(z,t)}{\partial t} \tag{2.32b}$$

For sinusoidal steady state conditions, with $v(z,t) = V(z)\sin(\omega t)$ etc., trav-

---

[5] TEM waves = Transverse Electro Magnetic waves, as opposed to TM and TE waves

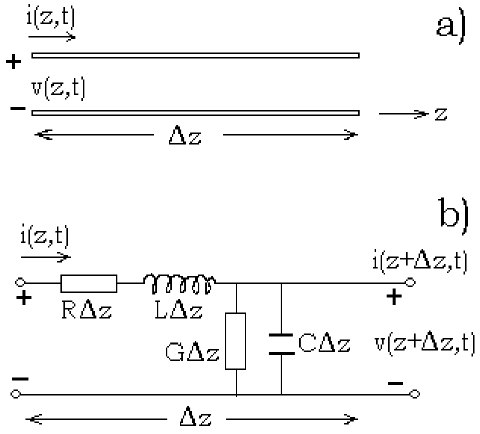

Figure 2.5: Two typical models for a transmission line. a) Two wire model, and b) lumped-element equivalence circuit.

eling wave solutions to equation 2.32a can be found as

$$V(z) = V_0^+ e^{-\gamma z} + V_0^- e^{\gamma z} \tag{2.33a}$$

$$I(z) = I_0^+ e^{-\gamma z} + I_0^- e^{\gamma z} \tag{2.33b}$$

where the sign (+ or -) represent the propagation direction along z. The propagation constant is

$$\gamma = \alpha + jk = \sqrt{(R + j\omega L)(G + j\omega C)} \tag{2.34}$$

Here α is the attenuation, k is the wave number, and $j = \sqrt{-1}$.

A central concept which we will use often in the coming chapters is the *characteristic impedance* often donated by Z_0 and defined as

$$Z_0 = \frac{V_0^+}{I_0^+} = \frac{V_0^-}{I_0^-} = \sqrt{\frac{R + j\omega L}{G + j\omega C}} \tag{2.35}$$

In the case of lossless transmission lines the characteristic impedance becomes real

$$Z_0 = \sqrt{\frac{L}{C}} \tag{2.36}$$

A typical example[6] is the coaxial cables we have used, with $Z_0 = 50\ \Omega$. We will assume lossless lines in the following, but losses can be considered by letting $k \rightarrow \gamma$.

If a transmission line with characteristic impedance Z_0 is connected to another line with characteristic impedance Z_L (or the line is terminated in an arbitrary load Z_L) the total voltage or current on the line will be a sum of incident and reflected waves. The amplitude of the reflected voltage normalized to the amplitude of the incident voltage is known as the voltage reflection coefficient Γ given by[23]:

$$\Gamma = \frac{V_0^-}{V_0^+} = \frac{Z_L - Z_0}{Z_L + Z_0} \tag{2.37}$$

One can also calculate the reflection coefficient at any distance l, where $l = -z$, from the junction (or load):

$$\Gamma(l) = \frac{V_0^- e^{-j\beta l}}{V_0^+ e^{j\beta l}} = \Gamma(0)e^{-2j\beta l} \tag{2.38}$$

where $\Gamma(0)$ is the Γ in equation 2.37. Since the reflection coefficient varies with distance from the junction this means that also the impedance will do so. A very important expression for the input impedance, which we will also use in the next section is the following:

$$\begin{aligned} Z_{in} &= \frac{V(-l)}{I(-l)} = Z_0 \frac{1 + \Gamma e^{-2j\beta l}}{1 - \Gamma e^{-2j\beta l}} \\ &= Z_0 \frac{(Z_L + Z_0)e^{j\beta l} + (Z_L - Z_0)e^{-j\beta l}}{(Z_L + Z_0)e^{j\beta l} - (Z_L - Z_0)e^{-j\beta l}} \\ &= Z_0 \frac{Z_L + jZ_0 \tan \beta l}{Z_0 + jZ_L \tan \beta l} \end{aligned} \tag{2.39}$$

---

[6] lossless in this case means just that losses are very small

To avoid reflections on the line Z_0, one needs to make Z_L look equal to Z_0. This is called impedance matching. A standard way of matching is to add a component, called a matching network, with input impedance equal to Z_0 between Z_0 and Z_L. Matching networks works mainly at one frequency (where $\Gamma = 0$), but there will be some bandwidth around this frequency where the reflection coefficient is small[23].

2.2.2 The original continous wave theory

During the 1960s Bolef *et al.*[24, 25, 26, 27, 28, 29] developed what they called 'High Frequency Continuous Wave Ultrasonics (CW)' based on ideas from the early days of ultrasonics. A review article was written by Bolef and Miller in Physical Acoustics in 1971 [8] and we will in what follows give the most important results and definitions from that article. As a start up we will give their view of precision of the system. They write '...CW spectrometer which are capable of measuring small changes in attenuation ($\Delta\alpha \simeq 10^{-6}\ cm^{-1}$ or less) and in phase velocity ($\Delta v/v \simeq 10^{-7}$).'. We will discuss this further in later chapters.

The basic CW transmission spectrometer contains three parts, as shown later in figure 3.12: 1) A signal generator 2) a composite resonator assembly and 3) a receiver section. The different CW techniques discussed in [8] relied all on the establishment of ultrasonic standing wave resonances in the composite resonator. The n'th resonance peak is defined by its resonance frequency f_n and its Q-value. The Q-value is defined by the linewidth at the half power points δf as:

$$Q = f_n/\delta f \tag{2.40}$$

The measured resonance frequency, f_n would, if the thickness of the transducer was negligible compared to the thickness of the sample, l_S, give the phase velocity in the sample, v:

$$v = 2l_S f_n/n \tag{2.41}$$

The attenuation α is related to the Q-value by

$$\alpha = (\pi f_n/v)Q^{-1} \tag{2.42}$$

This relation is found under the assumption that the resonance peak can be modeled by a series RLC-circuit.

Measurements of phase velocity as a function of some external parameter (temperature, magnetic field, ...) can be done by following the shift of the resonance frequency as the external parameter changes. We will call this ‘peak tracing’ in later chapters.

The theory describing the composite resonator is based on the transmission line equivalence for a transducer by Mason [30, 31] (see also section 2.1.3). The composite resonator is modeled as in figure 2.6. The two transducers (T_1 and T_2) and the sample (S) are all characterized by a phase velocity, v, a thickness, l, and a characteristic impedance, Z. Bonding effects are neglected. The characteristic impedance, per unit area, is given by:

$$Z = \rho v \tag{2.43}$$

where ρ is the density. Using equation 2.39 the impedances looking from

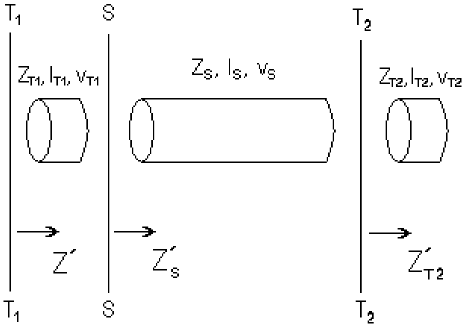

Figure 2.6: Transmission line equivalence of the acoustic composite resonator discussed in the text. The two transducers (T_1 and T_2) and the sample (S) are all characterized by a phase velocity, v, a thickness, l, and a characteristic impedance, $Z = \rho v$.

the planes T_1T_1, SS and T_2T_2 in the figure are given by:

$$Z' = Z_{T1}\left[\frac{Z'_S + Z_{T1}\tanh i(k_{T1} - i\alpha_{T1})l_{T1}}{Z_{T1} + Z'_S\tanh i(k_{T1} - i\alpha_{T1})l_{T1}}\right] \tag{2.44}$$

$$Z'_S = Z_S\left[\frac{Z'_{T2} + Z_S\tanh i(k_S - i\alpha_S)l_S}{Z_S + Z'_{T2}\tanh i(k_S - i\alpha_S)l_S}\right] \tag{2.45}$$

$$Z'_{T2} = Z_{T2}\tanh i(k_{T2} - i\alpha_{T2})l_{T2} \tag{2.46}$$

Under the assumption of lossless lines ($\alpha_l = 0$, $l = T_1, S, T_2$), the n'th resonance of the composite f_n^C occurs when the total impedance is zero. Assuming identical transducers ($T_1 = T_2 = T$) this then yields

$$2 + \frac{Z_S\tan k_S l_S}{Z_T\tan k_T l_T} - \frac{Z_T}{Z_S}\tan k_T l_T \tan k_S l_S = 0 \tag{2.47}$$

To solve this transcendental equation the tan-function is expanded in a power series around the resonances of the transducers and sample

$$\tan k_T l_T = \tan(\pi\frac{f_n^C - f^T}{f^T}) \simeq \pi\frac{f_n^C - f^T}{f^T} + ... \tag{2.48}$$

$$\tan k_S l_S = \tan(\pi n\frac{f_n^C - f_n^S}{f_n^S}) =\simeq \pi n\frac{f_n^C - f_n^S}{f_n^S} + ... \tag{2.49}$$

Here f_n^S denotes the n'th resonance frequency of the sample etc. Introducing the parameter η defined by

$$\eta \equiv \rho_T l_T/\rho_S l_S \tag{2.50}$$

equation 2.47 gives

$$(f_n^C - f_n^S) + 2\eta(f_n^C - f^T) - [n^2\eta^2/(f_n^S)^2]((f_n^C - f_n^S)(f_n^C - f^T) = 0 \tag{2.51}$$

Neglecting terms of order η^2 and higher the following relations are obtained

$$f_n^S = f_n^C + 2\eta(f_n^C - f^T) \tag{2.52}$$

and

$$(f_{n+1}^S - f_n^S) = (f_{n+1}^C - f_n^C)(1 + 2\eta) \tag{2.53}$$

If the small parameter η is negligible the measured composite frequency is the same as the sample's resonance frequency. It is straightforward to expand the analysis to also include higher harmonics of the transducers.

The two last equations can be combined with equation 2.41 to obtain

$$v_S \equiv 2l_S \Delta f^S = 2l_S \Delta f^C (1 + 2\eta) = 2l_S \frac{f_n^C + 2\eta(f_n^C - f^T)}{n} \tag{2.54}$$

Hhere $\Delta f^S \equiv f_{n+1}^S - f_n^S$ and $\Delta f^C \equiv f_{n+1}^C - f_n^C$.

The equivalence circuit presented in this section is a purely mechanical equivalence. The full equivalence should also contain the electrical port as described for transducers in section 2.1.3. The strength of the model presented is that it can easily be expanded or redused to more complicated or simple configurations. One can reduce the transducer-sample-transducer composite to a simpler transducer-sample system, with only one transducer. In this case equation 2.54 will be almost the same, but with $2\eta \to \eta$. We will discuss extentions of the model in section 4.1.2.

2.3 Vortex physics in HTS

2.3.1 The flux-line lattice and its elasticity

The HTSs are type-II superconductors. A common feature of type-II superconductors is that if a strong enough magnetic field is applied magnetic flux will penetrate the sample in form of flux lines[7] each carrying a quantum of magnetic flux $\phi_0 = h/2e$. The tiny vortices will tend to arrange them selves in a triangular flux-line lattice (FLL). The lattice vector of the ideal FLL is[3]:

$$a_\triangle = (2\phi_0/\sqrt{3}B)^{1/2} \tag{2.55}$$

which is about 49 nm for $B = 1$ T and 22 nm for $B = 5$ T, two typical examples for our measurements.

For isotropic superconductors in the London and continuum limit the elastic moduli are [3]:

$$c_{11} \approx c_{44} \approx \frac{B^2}{\mu_0} \frac{1}{1 + k^2\lambda^2} \tag{2.56}$$

and

$$c_{66} \approx \frac{B\phi_0}{16\pi\lambda^2\mu_0} \tag{2.57}$$

where λ is the magnetic penetration depth and k the wave vector. The physical reason for the strong dispersion of c_{11} and c_{44} is that since typically $\lambda \gg a_\triangle$ the FLL is much softer for short wavelengths compressional and tilt distortions than it is for uniform compression and tilt [3].

The high temperature superconductors are anisotropic materials with tetragonal or orthorhombic structure, which is considered quasi tetragonal in most theoretical investigations as the a- and b-axis are of almost equal length. Within the anisotropic extension of London theory the HTSs are charracterized by two magnetic penetration depths for the current in the ab-plane, λ_{ab}, and along the c-axis, λ_c. They are correspondingly characterized

---

[7] Flux lines are also called Abricosov vortices, vortex lines, flux tubes or fluxons

by two coherence lengths ξ_{ab} and ξ_c. The anisotropy factor is then given by

$$\Gamma = \frac{\lambda_c}{\lambda_{ab}} = \frac{\xi_{ab}}{\xi_c} \tag{2.58}$$

The GL parameter is defined as

$$\kappa \equiv \frac{\lambda_{ab}}{\xi_{ab}} \tag{2.59}$$

The HTSs have very high κ values (~ 100) due to the low electron density and high effective (electron) masses. The tetragonal structure with copper-oxide planes also make the FLL dependent on the angle between the crystal axes and the applied magnetic field. The notation we will choose for the FLL was introduced by Sudbø and Brandt[32]. The $\parallel$ or $\perp$ refer to the compression, tilting or shear of the FLL being parallel or perpendicular to the ab-planes. The applied magnetic field (and the FLL) will be considered here only when it is parallel with the c-axis or the ab-planes. When the FLL is parallel with the c-axis no $\parallel$ or $\perp$ will be written (see table 2.2).

The tilt and compressional elastic moduli for anisotropic superconductors have been calculated in[32, 33, 34]. The expressions will not be given here as the measurements considered will be in the long wavelength limit ($k \approx 0$). Hence all the observable c_{11} and c_{44} will, at $T = 0$ K, be given approximately by B^2/μ_0.

The shear modulus is strongly dependent on the anisotropy, as first pointed out by Kogan and Campbell[35] and also by Sudbø and Brandt[36]. With the names c_{66}^e (easy) and c_{66}^h (hard) for $c_{66,\parallel}$ and $c_{66,\perp}$ respectively, the three main shear moduli are given by:

$$c_{66} \approx \frac{B\phi_0}{16\pi\lambda_{ab}^2\mu_0} \tag{2.60}$$

$$c_{66}^h = c_{66}\Gamma \tag{2.61}$$

$$c_{66}^e = c_{66}/\Gamma^3 \tag{2.62}$$

An explaining sketch is shown in figure 2.7. With high anisotropy factor the hard shear modulus c_{66}^h can become quite big, while c_{66}^e will be extremely small. We will discuss this in more detail in section 4.4. Elastic moduli, both for the orthorhombic crystal itself and the FLL, which in principle could be measured with our ultrasonic system, are given in table 2.2. The magnetic field is assumed to be parallel to one of the crystal axes and the crystal is assumed to have planes cut perpendicular to the crystal axes.

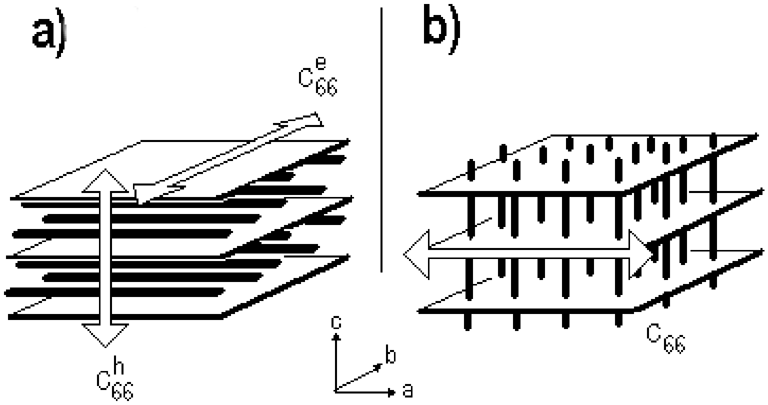

Figure 2.7: A sketch of fluxlines and ab-planes in a high temperature superconductor. The figure is *not* to scale. The share directions for the three shear moduli c_{66}^e, c_{66}^h, and c_{66} are indicated.

Table 2.2: Elastic moduli measured by different waves along the a, b or c-axis in a crystal with orthorombic symetry.

Crystal moduli	*Wave*	$\vec{u}, \vec{k}$	*Magnetic field*	*FLL moduli*
C_{11}	L_x	$\vec{u} \parallel \vec{k} \parallel a$	$B_a \parallel c$	c_{11}
			$B_a \parallel a$	$-$
			$B_a \parallel b$	$c_{11,\parallel}$
C_{22}	L_y	$\vec{u} \parallel \vec{k} \parallel b$	$B_a \parallel c$	c_{11}
			$B_a \parallel a$	$c_{11,\parallel}$
			$B_a \parallel b$	$-$
C_{33}	L_z	$\vec{u} \parallel \vec{k} \parallel c$	$B_a \parallel c$	$-$
			$B_a \parallel a$	$c_{11,\perp}$
			$B_a \parallel b$	$c_{11,\perp}$
C_{44}	T_{yz}	$\vec{u} \parallel b, \vec{k} \parallel c$	$B_a \parallel c$	c_{44}
			$B_a \parallel a$	c_{66}^{e}
			$B_a \parallel b$	$-$
C_{44}	T_{zy}	$\vec{u} \parallel c, \vec{k} \parallel b$	$B_a \parallel c$	$-$
			$B_a \parallel a$	c_{66}^{h}
			$B_a \parallel b$	$c_{44,\perp}$
C_{55}	T_{xz}	$\vec{u} \parallel a, \vec{k} \parallel c$	$B_a \parallel c$	c_{44}
			$B_a \parallel a$	$-$
			$B_a \parallel b$	c_{66}^{e}
C_{55}	T_{zx}	$\vec{u} \parallel c, \vec{k} \parallel a$	$B_a \parallel c$	$-$
			$B_a \parallel a$	$c_{44,\perp}$
			$B_a \parallel b$	c_{66}^{h}
C_{66}	T_{xy}	$\vec{u} \parallel a, \vec{k} \parallel b$	$B_a \parallel c$	c_{66}
			$B_a \parallel a$	$-$
			$B_a \parallel b$	$c_{44,\parallel}$
C_{66}	T_{yx}	$\vec{u} \parallel b, \vec{k} \parallel a$	$B_a \parallel c$	c_{66}
			$B_a \parallel a$	$c_{44,\parallel}$
			$B_a \parallel b$	$-$

2.3.2 Pinning and TAFF

Research on HTS materials have shown how vortices can be pinned by a number of different pinning sites. To mention but a few there are point pins like oxygen vacancies or embedded particles, line pins like dislocations or radiation tracks, and planar pinning sites like twin boundaries or intrinsic (CuO-plane) pinning. There are several theories describing pinning and how it works under different 'initial conditions'. We will just briefly *mention* theories which are relevant for our measurements and without going into detail.

Point pins are important in the collective pinning theory by Larkin and Ovchinnikov[37]. Relevant for us is the fact that a rigid (not elastic) vortex lattice would *not* be pinned by randomly distributed pinning cites. This is because every configuration would have the same energy, and hence no pinning force can arise.

If the flux lines are subject to some driving force (by for instance a magnetic field, a sound field or an electric current) then, depending on the strength of the pinning sites compared to the driving force, in a given temperature range (for excample near T_c or near $T = 0\ K$), different kinds of flux flow or creep may occur.

A phenomenon called Thermally Assisted Flux Flow (TAFF)[38, 39] explained the irreversibility line measured in magnetization or susceptibility measurements and were also used by Pankert *et al.*[40, 41] to explain their measurements of the elasticity of the FLL. TAFF occurs in superconductors with an intrinsically low pinning barrier and at temperatures high enough to overcome this barrier. Pankert showed that for a given sound mode probing c_{11}, c_{44} or c_{66} of the vortex lattice (see table 2.2) gave a contribution Δc^f superimposed on the elastic moduli of the crystal:

$$\Delta c^f = c_{ii} \frac{\omega^2}{\omega^2 + (c_{ii}\gamma k^2)^2} \tag{2.63}$$

Here γ is a phenomenological relaxation coefficient related to the depinning energy[42], k is the wave number, ω is the angular frequency, and $i = 1, 4, 6$. Further discussion of the theory is postponed to section 4.4.

2.3.3 Flux lines, vortex loops and phase transitions

If we compare the cuprate (high temperature) superconductors with BCS (low temperature) superconductors there are some striking differences which make the magnetic field versus temperature (B-T) phase diagram very different in the two cases. The core of BCS theory is electron pairing, i.e. electrons interacting via the lattice form Cooper pairs. In LTS typical Cooper pair sizes are on the order of 1000 Å. The electron density is very high so the cooper pairs highly overlap. A mean field description is therefore expected to be valid, and BCS theory is shown to work perfectly. In HTS the situation is quite different. The Cooper pairs are small ($\sim 3-10$ Å) and the electron density is low. With the high critical temperatures and the 'non overlapping' Cooper pairs strong fluctuation effects are to be expected and clearly observed.

One of the manifestations of fluctuation effects expected was the existence of a flux line liquid. Already 2-3 years after the discovery of HTS the first ideas [43, 44, 45] of a molten phase in the vortex state were put forward. At first depinning was a competing explanation [40], but presently melting of the FLL in a first order phase transition is no longer in question. During the last few years experimental evidence has accumulated from measurements of resistivity [46, 47], magnetization [48], heat capacity [49, 50], scanning hall probe microscopy [51] etc. The methods mentioned above provide at best only indirect measurements with respect to the elastic behavior of the FLL. The direct proof of a molten phase would come from measuring a complete softening of the shear modulus c_{66}. So far this has been impossible to measure, due to the extreme smallness of c_{66}.

There are not many theories explaining FLL melting and other fluctuation mediated effects in the HTS. We will mainly look at the 3D-XY model. There has been no evidence contradicting that the Ginsburg-Landau theory for type-II superconductors also works for HTS. One can do small modifications to incorporate the stratification of these materials (Lawrence-Doniach model[52]) and usually the theory has to be simplified. One of these simplifications is to assume that there are no fluctuations in the amplitude of the wave function, leaving the phase as the only degree of freedom[53]. Making a lattice model with local phases having some direction in the xy-plane in the three dimensional crystal yields the 3D-XY model. Extensive monte Carlo simulations on the 3D-XY and similar models [53] reveal a fundamentally new picture from what was known before. In short what could be called the vortex-loop-blowout theory [54, 55, 56] predicts that as the temperature increases the FLL melts first to an incoherent vortex liquid with a finite line tension and then, in a new phase transition [54], looses its line tension before the crossover to the normal phase at B_{c2}. The zero field continuous phase transition at T_c is governed by a blowout of thermally induced vortex loops. The B_{c2}-crossover represents the remanence of this blowout and is in this picture not the superconducting to normal phase transition as in LTS.

There have been many controversies about the 3D-XY model the last few years. Alternatives to the 3D-XY model have been the decoupling model [57] and the lowest-Landau-level (LLL) model [58]. Both these two last models are expected to work better for very anisotropic materials like BSCCO than for example YBCO. The LLL model is expected to describe the situation in high magnetic fields whereas the 3D-XY model should only work for lower fields. We will postpone the further discussion to Chapter 4 with emphasis on our measurements, comparing them to measurements of heat capacity and thermal expansion.

Many other phase transitions and crossover lines than mentioned here have been proposed for the magnetic phase diagram of the HTS. For a resent review see [4].

Chapter 3

Experimental

3.1 Single crystals

The crystals are the most important part of the experimental system. We have mainly been working with two optimally doped LSCO crystals, but have also done some few measurements on other materials. The four crystals presented in Chapter 4 will be discussed here. Some characteristics are listed in table 3.1. The transition temperatures as listed are on-set T_c's defined from the susceptibility data in figure 3.1-3.4. The transition width ΔT_c is also estimated from the Susceptibility data for each crystal.

The data in figure 3.1 and 3.2 have been measured by Dr. N. Kikugawa

Table 3.1: Characteristics of HTS crystals used in the measurements

Sample	*Chemical formula*	$T_c(K)$	$\Delta T_c(K)$	*Crystal grown by*
F40	$La_{1.85}Sr_{0.15}CuO_4$	37.8	0.8	Dr. N. Kikugawa
F60	$La_{1.85}Sr_{0.15}CuO_4$	37.1	10	Dr. N. Kikugawa
NO970822	$Bi_{2.2}Sr_{1.8}CaCu_2O_x$	83.3	3.5	Dr. K. Oka
WAX144-1	$Nd_{1.03}Ba_{1.97}Cu_3O_x$	92.5	2.3	Dr. T. Wolf

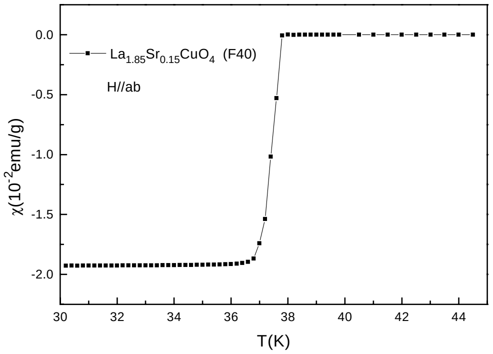

Figure 3.1: Susceptibility data of the crystal F40 in a zero field cooled measurement with a field of 2 mT parallel to the ab-planes.

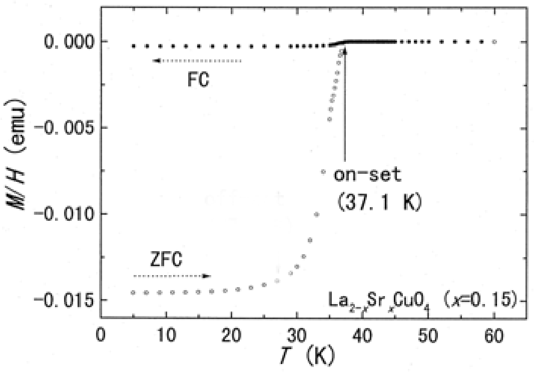

Figure 3.2: Susceptibility data of the crystal F60. The applied field of 2 mT is parallel to the ab-planes. The figure is made by Dr. N. Kikugawa.

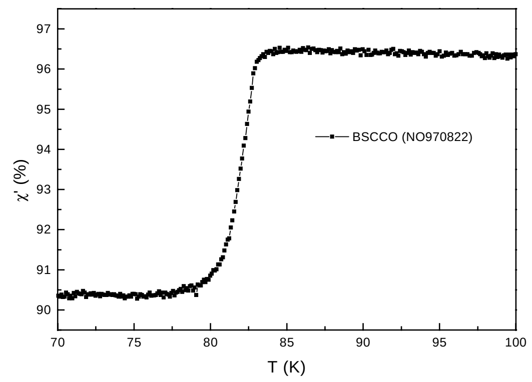

Figure 3.3: AC-Susceptibility data of the crystal NO970822

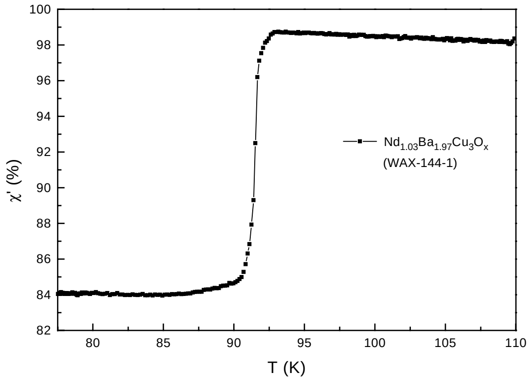

Figure 3.4: AC-Susceptibility data of the crystal WAX144-1

at the University of Hiroshima with a SQUID magnetometer[1]. The other two measurements have been measured in our lab with an in-house built AC-susceptibility system presented in section 3.2.

We will discuss details important for the measurements, for each of the crystals.

$La_{1.85}Sr_{0.15}CuO_4$, F40:

The sample was grown by a traveling-solvent-floating-zone (TSFZ) method [59]. The Sr concentration was measured to be 0.146 ± 0.02 by EPMA. The crystal was annealed in oxygen for 50 hours at 450 $°C$, in order to achieve good oxygen filling and thereby reduce the pinning by oxygen deficiencies. The crystal orientation was determined by X-ray back-reflection Laue technique. It was originally cut and polished to a final rectangular shape with planes parallel to the crystal axis. The dimensions were $L_{[100]} \times L_{[010]} \times L_{[001]} = 1.4 \times 3.4 \times 2.0$ mm^3. The reflection measurements discussed in Chapter 4 were all done on the crystal when it had these dimensions. See also section 3.2.

LSCO undergoes a structural phase transition from a tetragonal (THT) to an orthorhombic (OMT) phase[2] at a temperature T_d, which is doping dependent. For F40 T_d si about 180 K, and twin boundaries will be present below this temperature. In the reflection measurements slow cooling of the sample was performed before each measurement in order to introduce as few defects as possible.

In an attempt to reduce the number of twin boundaries to an absolute minimum the crystal was in later transmission experiments detwinned during cooling. The crystal was cut and polished with two parallel planes perpendicular to the [110]-axis. A uniaxial stress of approximately 4 MPa was applied to the sample along the tetragonal [110] axis during the measurements. See figure 3.5. The crystal [100]- and [010]-axes are shifted 45° in going from the THT to the OMT phase. An applied stress along

---

[1] Quantum Design, model MPMS

[2] The abbreviations are: THT = Tetragonal at High Temperatures, OMT = Orthorhombic at Middle Temperatures

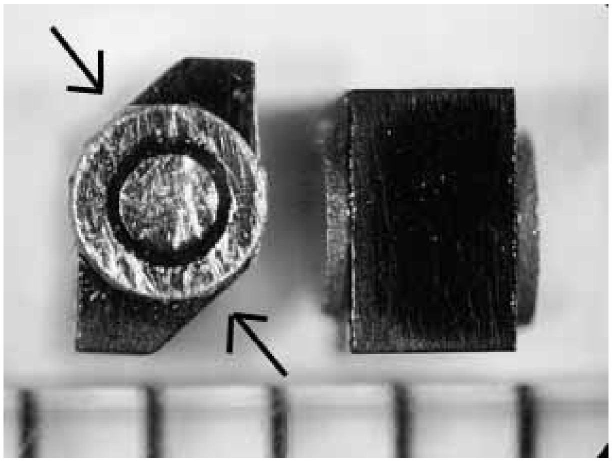

Figure 3.5: A photo of the samples F40 (left) and F60 (right) with transducers, 1.5 mm in diameter, mounted. The two arrows show the direction of the applied pressure in the detwinning of F40. The black lines at the bottom of the picture are 1 mm apart.

the tetragonal [110]-axis will make this the [100]-axis[3] in the orthorhombic phase below T_d [60, 61, 62]. Nakayama *et al.*[61] reported that a uniaxial stress of 1.5 MPa was enough to get 85-90% of the volume with the [100]-axis parallel to the direction of the stress, for a near optimally doped LSCO crystal (x=0.14). Even though the detwinning might not be 100% in our measurements we have assumed this in the measurements discussed in Chapter 4.

The crystal was characterized also by magneto optical (MO) measurements. Measurements were done with our in-house built system discussed in section 3.2. A series of six pictures for F40 measured at 30 K is shown in figure 3.10. Other MO measurements for F40 and F60 will be discussed in section 4.4.

An estimate of the anisotropy factor, Γ was found from resistivity data[4] as [63]:

$$\Gamma^2 = \rho_c(50K)/\rho_{ab}(50K) \tag{3.1}$$

We found $\Gamma^2 = 617$, consistent with the data shown in table 1 in [63].

$La_{1.85}Sr_{0.15}CuO_4$, F60:

The crystal was grown by the TSFZ method as for F40 discussed above. The growth velocity was very similar in the two cases, but the growth temperature was slightly higher for F60. The Sr concentration of F60 was measured to be 0.145 ± 0.02 by EPMA. The crystal was cut and polished to a rectangular shape with axes along the tetragonal [110], [1$\bar{1}$0], and [001] directions. The dimensions were $L_{[110]} \times L_{[1\bar{1}0]} \times L_{[100]} = 1.4 \times 3.4 \times 2.0$ mm^3. A picture of the crystal is shown in figure 3.5. The depinning procedure was the same for F60 as for F40. Susceptibility data are shown in figure 3.2. T_c and ΔT_c can be found in table 3.1. We will dicuss the wide transition related to the ultrasonic measurements in Chapter 4. The information we have from the crystal grower does not explain the difference in transition

---

[3] The [100]-axis and not the [010]-axis since the [100]-axis is shorter.

[4] The resistivity measurements were by Dr. N. Kikugawa. The measurements were done on a different part of the crystal F40 than the one we have used for ultrasonic measurements

widths between F40 and F60.

$\mathbf{Nd_{1.03}Ba1.97Cu_3O_x}$, WAX144-1:

We had three parts of the original crystal each with mm dimensions in each direction. Details of the crystal growth method can be found in [64, 65]. Big crystals of $Nd_{1+y}Ba2-yCu_3O_x$ (NBCO) often have long cracks along the ab-planes. Also WAX144-1 had this features, which could be observed both by a light-microscope and acoustically. The crystals were heavily twinned, which could be observed directly by a polarization microscope. We found T_c= 92.5 K and ΔT_c = 2.3 K from the susceptibility measurements, figure 3.4.

$\mathbf{Bi_{2.2}Sr1.8CaCu_2O_{8+x}}$, NO970822:

The sample was originally about 1 mm thick along the [001]-axis and about 7 mm and 4 mm in the directions along the [100]- and [010]-axis respectively. The original shape was like a slightly coned half cylinder. The orientation of the crystal was checked by Laue back-scattering measurements. We found a Bi-deficient superstructure along the [100]-axis as described in [66]. The crystal was grown by the TSFZ method, further details can be found in [67]. We cut off one small part intended for measurements of c_{66}^h, and used the bigger part for other measurements. The sample was extremely brittle so small pieces of each part broke off. Later inspections showed that the 'crystal' was really at least three crystals grown into each other. The extreme flakyness also prevented us from polishing the sample. It therefore had a somewhat irregular shape[5] when we did the ultrasonic measurements shown in section 4.3. We found T_c= 83.3 K and ΔT_c = 3.5 K from the susceptibility measurements, figure 3.3.

Other crystals:

We have also had in hand some other crystals, which we will briefly discuss:

---

[5] One of the two parallel surfaces used in the measurements was a cleavage plane, the other was cut with a diamond saw.

Two YBCO crystals, AE258G and AE493, grown by Dr. A. Erb with T_c's of 91.1 K and 85.5 K respectively, had very sharp transitions (0.2 and 0.5 K) but showed to be much too thin for our ultrasonic measurements. The thickness along the [001]-axis were 0.15 mm for AE258G and 0.27 mm for AE493.

A LSCO sample, F73, with Sr concentration $x = 0.10$ were grown by Dr. N. Kigugawa. This crystal showed a transition width of about 10 K. No measurement have been done on the crystal, in some extent due to the wide transition, but also due to the small size.

One YBCO crystal, TWOX321-1, and one NBCO crystal, WAX191-1 (with T_c=95.5 K and $\Delta T_c = 0.9$K), were grown by Dr. T. Wolf. We had two parts of TWOX 321-1 with thickness 0.5 and 0.6 mm, also these turned out to be too thin to measure by ultrasonics. The two parts of WAX191-1 had big cracks which made ultrasonic measurements impossible. See figure 3.11.

3.2 Cryostats

The purpose of the measurements has been to investigate elastic properties of the HTS samples in relatively high magnetic fields. We chose to use an old 5 T NMR magnet in our laboratory for the measurements[6]. The system was made by Oxford instruments[7] in 1984 and contained, in addition to the stainless steal dewar with the $NbTi$ solenoid, an analog current source, a LHe-meter, a sample holder, and some equipment intended for NMR measurements. The advantage of choosing an NMR-magnet is the high homogeneity needed in those systems. The current source used for magnetizing the solenoids were connected to an analog amperemeter. The magnetic H-field was calculated from the applied current. We have used the symbol B_a for the applied magnetic field, measured in Tesla, where $B_a = \mu_0 H$. The applied current,I_a, measured with an accuracy of ± 0.25 A, was related to the magnetic field as:

$$B_a = 0.0727 I_a \tag{3.2}$$

The top-loaded sample holder, or cryostat, was rebuilt for the ultrasound measurements. All coils and plugs were changed and a new sample cell was made. A sketch of the magnet, with the original inner vacuum chambers and the sample holder, is shown in figure 3.6. The figure is explained in the figure caption. A serious disadvantage with the original cryostat was that it was very thin, and therefor gave very little place for mounting of the sample. Space was needed because the transducers were held in place by spring loaded gold contacts about 10 mm long[8]. With an available space of 2.2 cm in diameter we chose to do reflection measurements, reducing the number of transducers from two to one. This made the mounting of the sample and the transducer much simpler. Especially for shear transducers which needed to be mounted with the polarization

---

[6] The two other magnets in the laboratory were also considered, but the 6 T magnet had a leak and the 10 T magnet had shown to be too LHe-consuming and difficult to handle for one person.

[7] Oxford Instruments: Solenoid S/5/50/.002, Project number B26723

[8] They were originally 22 mm long, but we cut them as much as we could.

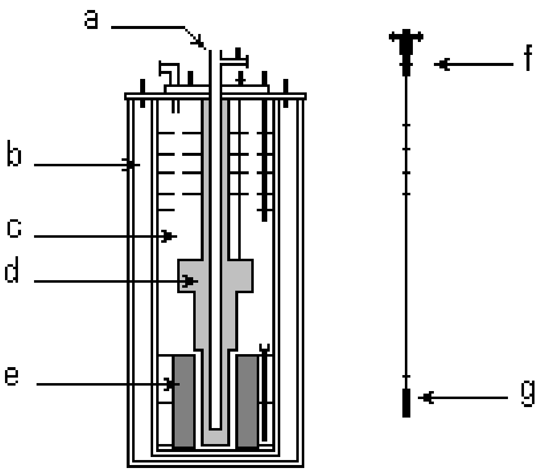

Figure 3.6: A sketch of the original NMR magnet system. The parts indicated on the figure are in alphabetic order: The inner sample chamber (a) into which the cryostat were inserted, the LN_2 chamber (b), the LHe chamber (c), The inner vacuum chamber (d), and the $NbTi$ solenoid (e). The top-loaded cryostat (f) is shown on the right with the sample cell (g) indicated.

along the crystal axis. We will discuss details of the cell design below, but for a different cryostat.

Cooling of the sample was in the original system done by introducing cold helium gas from the bottom of the sample chamber. A needle valve connecting the outer liquid helium bath to the inner parts of the system was used. This had to be done manually. In NMR measurements relaxation times are in the order of fractions of a second, the need for stable temperatures over long time were therefor much less than in our measurements. The introduction of cold gas as the coolant became extremely difficult to control with the accuracy we wanted, often resulting in too high pressure in the sample chamber and measurements under very varying conditions. The preliminary solution we found to the problem was to reduce the vacuum between the helium bath and the sample chamber (the unit 'd' in figure 3.6). With this procedure temperature control could be done satisfactory, but the helium boil-off was extremely high (from 3.5 to 7 liter per hour!)[9].

We finally came to the conclusion that a new system had to be built allowing much better experimental conditions. We will name the original cryostat system 'The reflection cryostat' in the following. Though almost impossible to use with LHe as a coolant, it was quite easy to use with LN_2. Many tests of the measurement method and parts of the system were successfully done with this cryostat.

The 'new cryostat' we build was a traditional two-chamber cryostat, which fit into the $NbTi$ solenoid. The outer dimensions of the cryostat were largely the same as those of the original inner vacuum chamber, shown in figure 3.6. A difference with the new cryostat was that there was left more space for liquid helium in the dewar. A drawing of the cryostat is shown in figure 3.7. Two different mounting configurations were needed in the measurements; one with the propagation direction of the ultrasound parallel to B_a, the other perpendicular to it. Closeups of the sample cell for each of these two setups are shown in figure 3.8 and figure 3.9.

On the top A in figure 3.7 vacuum tight electrical feedthroughs were

---

[9] The system had to be almost constantly watched resulting in work shifts of about 20 hours or so with less than 4 hour sleep in between.

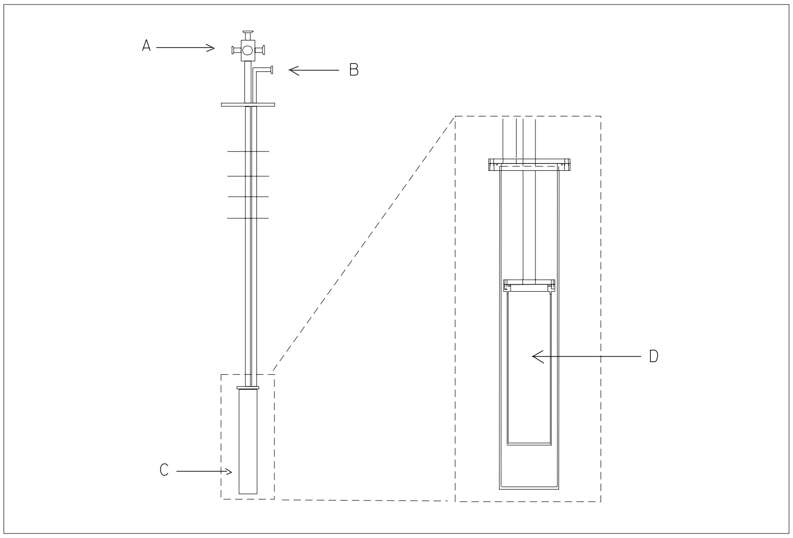

Figure 3.7: The ‘new cryostat’ used in most of our measurements. Vacuum tight electrical feedthroughs is mounted at the top A. Pumping of the inner chamber D is also done there. The outer vacuum chamber C has a separate pumping line B.

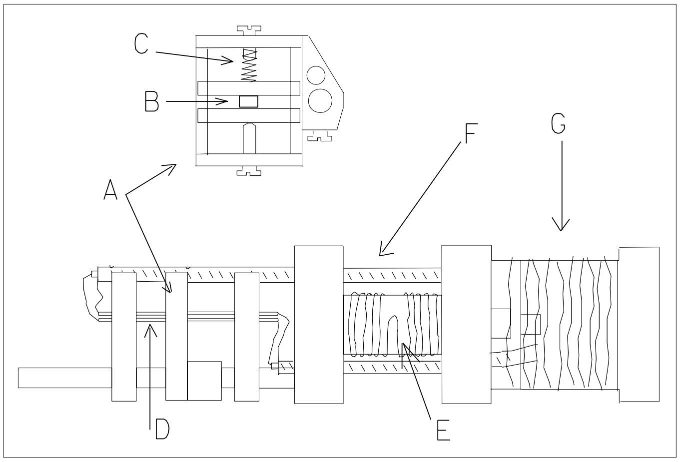

Figure 3.8: The sample cell used when the propagation direction of the acoustic waves was parallel to the magnetic field. Shown in the figure are: The sample holder A, a sample B, the spring used for detwinning C, Spring loaded gold contacts D, The heating vire E, coaxial cables F, and the area used for thermal anchoring of coils G.

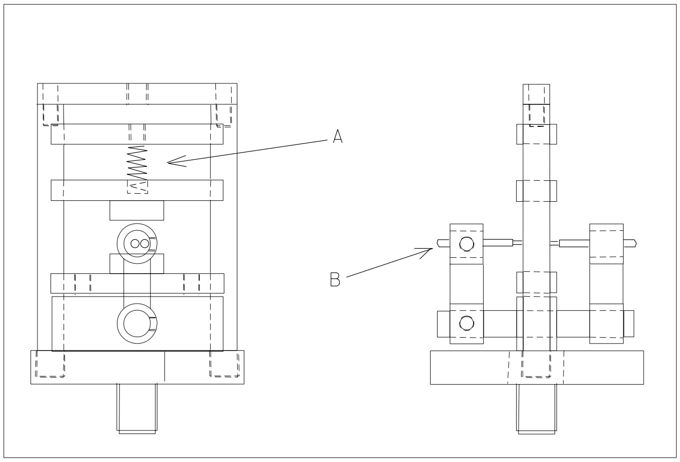

Figure 3.9: Details of the sample cell used when the propagation direction of the acoustic waves was perpendicular to the magnetic field. The spring used in the detwinning of the crystal (A) and the gold contacts (B), discussed in the text, are indicated.

connecting the outer circuit to the coils inside the cryostat. Pumping of the inner chamber D was also done there. The outer chamber C had a separate vacuum line B. There were two coaxial coils[10] connected to the outer BNC plugs by a SMC-BNC connection. For each of the thermometers there were four 0.08 mm thick Cu-coils and for the heating wire two 0.25 mm thick Cu-coils. The Cu-coils were twisted in pairs. The inner chamber D was filled with about 1 atm He-gas at room temperature, resulting in a lower pressure at low temperatures[11]. The exchange gas was needed for the temperature control as discussed below. The outer chamber C was evacuated to a pressure of $\sim 10^{-6}$ mbar, and continously pumped during the measurements.

The sample cell drawn in figure 3.8 was used in the measurements where the applied field was parallel to the propagation direction of the acoustic waves. The sample holder A is shown with a sample B and a spring C used for detwinning the sample. Spring loaded gold contacts[12] D were connecting the coaxial cables F to the transducers. The contacts were spring loaded in order to keep the transducers in place on the sample. The transducers had a coaxial electrode configuration as shown in figure 3.5. Ideally, the spring loaded contacts should also have been coaxial, but we could not get hold of short enough coaxial contacts and were therefore forced to use others. We have tested coaxial contacts in other measurement setups discussed below. No measurable difference was seen, probably due to the short length of the contacts. A crucial and practically difficult step was to line up the small sample, the polarization direction of each of the two transducers, and the magnetic field. We used a microscope when mounting the sample. We estimate typical alignment errors to be less than ±2°. We used mainly a Carbon-Glass (CGR) thermometer[13] for the LHe-measurements, and a platinum (Pt) resistance thermometer for measurements at higher

---

[10] Suhner RG-178

[11] A reasonable estimate of the pressure for a given temperature can be found by the ideal gas law.

[12] Produced by Ingun UK Ltd. [68].

[13] Lake Shore Carbon-Glass Resistor Model: CGR-1-2000, Calibrated by Lake Shore from 4.0 to 325 K.

temperatures. The thermometers were placed close to the sample. They are not shown in the figure. The heating wire E was used to control the temperature in the cell, by a temperature controller as discussed in section 3.3. The heating wire were wound half way clockwise the other half counter clockwise in order to avoid inducing a (small) magnetic field during the temperature control. The helium exchange gas mentioned above was needed to create a uniform temperature in the whole cell. This was necessary because the thermometers were much bigger than the sample. During control of the temperature the measured temperature was kept constant during minutes for each point measured. We will discuss this in further detail in section 3.3. All cables/coils were thermally anchored at the 'top' of the sample cell as indicated schematically in the figure (area G).

The sample cell in figure 3.9 shows only that part of the cell which is different from figure 3.8. The spring used for detwinning A, and the gold contacts B, are also indicated in the figure. This cell was used when the magnetic field was perpendicular to the direction of the acoustic waves. All the different parts in figure 3.8 and 3.9 were made of copper.

We have, in addition to the two cryostats discussed above, also used three other ultrasonic measurement systems. Two of the systems have not been cryostats at all, but table-models for work in air at room temperature. With these we could do many systematic checks of the method. The third system was a cryostat made for measurements in zero magnetic field with LN_2 as a coolant. The measurements done on the sample WAX144-1 presented in section 4.3 were measured with this cryostat. The design was to a large extent the same as for the cryostat discussed above. Due to a bigger space for the mounting of samples we were able to use spring loaded 50 Ω coaxial gold contacts[14] for connection to the transducers.

An in-house built AC-susceptibility system was used for sample characterization as mentioned in section 3.1. In short, the principle behind the measurements is as follows: An AC-current, at 300 Hz, is inducing a magnetic field in a solenoid. Inside the solenoid is another solenoid around the sample under investigation. The sample, being the core of the inner coil will,

---

[14] Produced by Ingun UK Ltd.[68].

due to its diamagnetic behavior, lead to a phase shift of the field induced in the inner coil when the sample becomes superconducting. The voltage over the inner solenoid is compared with the original signal by means of a lock-in amplifier. The in-phase component of the resulting signal being proportional to the real part, χ', and the out-of-phase part proportional to the imaginary part, χ",of the complex susceptibility. Our measurements were done by slowly cooling or heating the sample. We made a program for taking data at every 0.1 K. The temperature was read by a Pt-thermometer located close to the sample.

We have also built a magneto optical system for sample characterization. The cryostat is a flow cryostat where cold helium gas is used for cooling. The sample is glued to a 'cold finger' which is in contact with the cooling gas. On top of the sample we put a film of bismuth doped Yttrium Iron Garnet (Bi:YIG) which utilize the Faraday effect. A polarization microscope and digital camera is then used in recording the amount of flux inside the sample. The temperature of the sample was read with a CGR-thermometer, and the temperature was controlled via the gas flow. A series of six pictures measured for the sample F40 at 30 K shown in figure 3.10 is shown here as an example of typical MO measurements with our apparatus. Reading from left to right in the figure the applied fields are 10, 20, 30, 35, 40, and 50 mT. The maximum field we could use with our system was 50 mT. The inner black region in the pictures shows no flux penetration. This part of the sample is therefore still in the Meissner phase. In the gray outer region flux penetrates as described by the critical state model [69, 70]. The MO technique is mainly used to investigate the flux penetration, pinning or similar for the sample [69, 70]. We have found it to be a good tool also for investigating cracks in the sample, not necessarily observable from the outside. Two examples are shown in figure 3.11 for the samples WAX144-1 and WAX191-1. The cracks are apparent as the flux penetrates the sample from the edges, along the cracks. This kind of investigations is well established [69]. We will discuss other MO data in section 4.4.

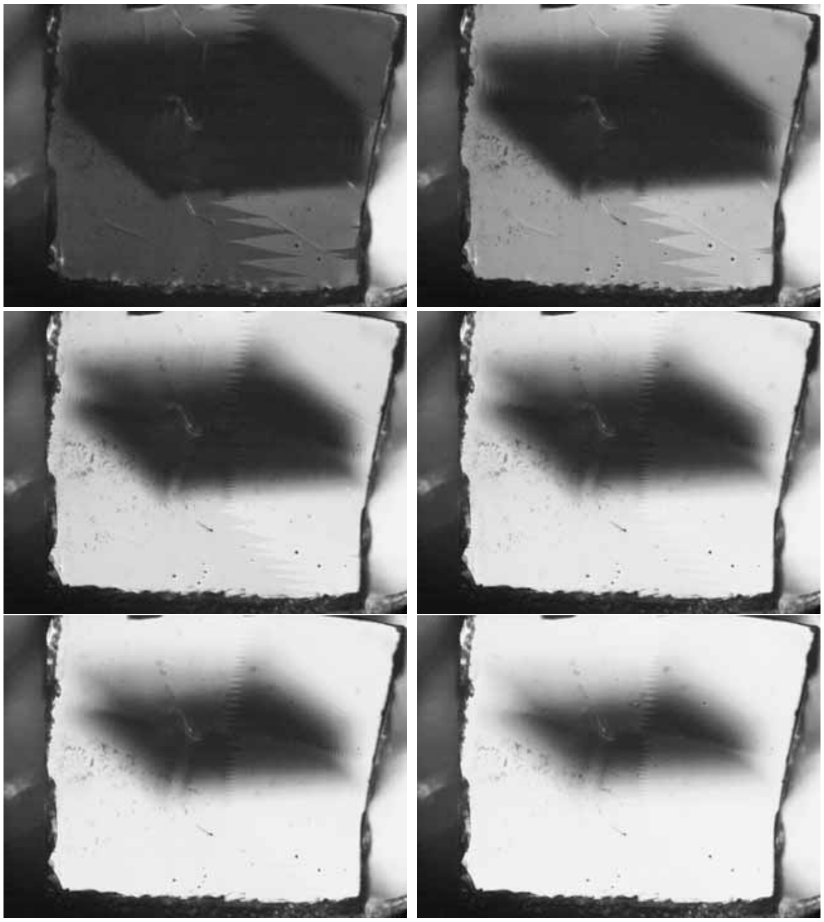

Figure 3.10: MO measurements of the sample F40 at 30K. The applied fields parallel to the c-axis of the crystal are, reading from left to right, 10, 20, 30, 35, 40, and 50 mT. The real shape of the sample is clearly seen in the upper left picture where full screening still exists.

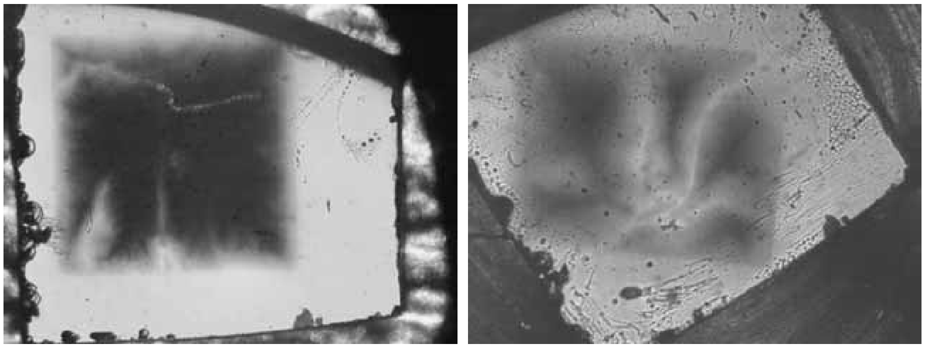

Figure 3.11: Two examples of MO measurements revealing cracks in a sample. The left figure shows the sample WAX144-1. The right picture shows the sample WAX191-1. Both recordings were done at about 80 K.

3.3 Circuits and computer programs

The first circuit, hereafter named 'Circuit 1', to be discussed is shown in figure 3.12. It consists of a signal generator, an ultrasonic composite resonator (Transducer-Sample-Transducer), an amplifier, a diode detector, and a digital multimeter (DMM). The different elements in the circuit are connected via standard 50 Ω coaxial cables. The equipment we have used is shown in table 3.2, also for the circuits discussed below. Circuit 1 is used for screening the resonance frequencies of the ultrasonic composite.

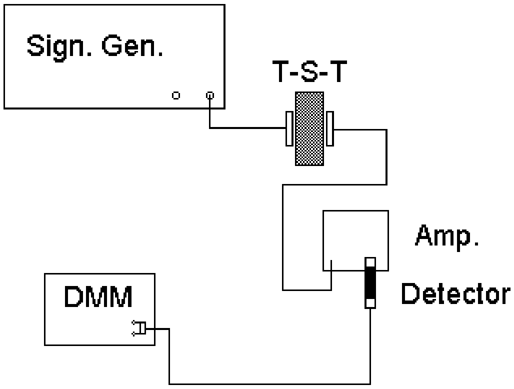

Figure 3.12: Circuit 1 used for frequency sweeps. The circuit contain a signal generator, an ultrasonic composite resonator (Transducer-Sample-Transducer), a RF amplifier, a diode detector, and a digital multimeter (DMM). The apparatus are connected via 50 Ω coaxial cables (black lines).

All measurements were done automatically using a PC with a general purpose instrumentation bus (GPIB)[15]. Programs were written in Quick Basic 4.5. The screening, or frequency sweep, was done with a computer

---

[15] We used a PC2A-card from National Instruments Corporation.

Table 3.2: Equipment used in the measurements

Unit	*Full name*
Sign. Gen.	HP 8643A Synthesized Signal Generator
Amp.	HP 8447D Amplifier
Detector	HP 8471D Detector
DMM	Keithley 196 system DMM
Lock-in Amp.	EG&G 5302 Lock-in Amplifier
OSC.	Tektronix 2230 Digital Storage Oscilloscope
Temp. Cont.	Linear Research LR-130 Temperature Controller
DC	Anzac H-9 Hybrid Junction

program called 'FSWEEP' in the following. A flow diagram is shown in figure 3.13. The user sets the start frequency, f_{Start}, the end frequency, f_{end}, the size of the frequency steps, f_{step}, between each point measured, and the input amplitude of the RF-signal. The RF signal is generated by the signal generator and sent to the first transducer, one frequency at a time. Out of the second transducer comes a signal with the same frequency, but with a much lower amplitude. This is then amplified and rectified by the amplifier and detector before it is measured as a DC voltage by the DMM. The frequency and the output amplitude are recorded by the program. Data are plotted on the screen and saved in a data file. An example of a frequency sweep is shown in figure 3.14. This measurement is done at room temperature on a 1 mm glass sample with longitudinal transducers, having fundamental frequencies of about 30 MHz. These and other data will be further discussed in Chapter 4.

The second circuit, Circuit 2, is shown in figure 3.15. In this circuit the output signal is measured by a lock-in amplifier instead of the multimeter. The RF signal from the signal generator is frequency modulated (FM) and the audio signal used for modulation is used by the lock-in amplifier as a reference. The principle behind the frequency modulation method is illustrated in figure 3.16. The FM signal is slowly swept trough the

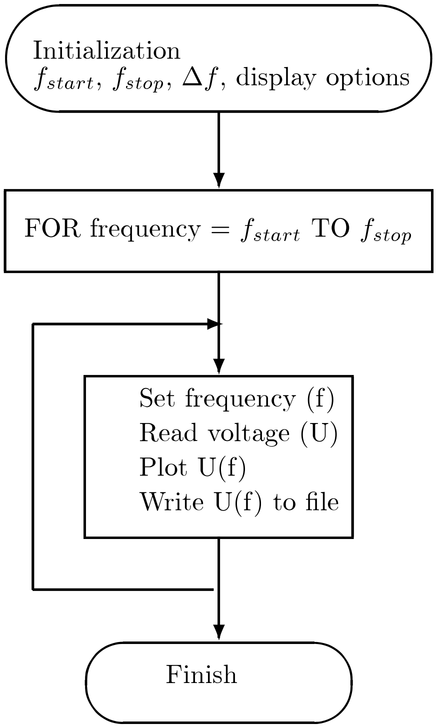

Figure 3.13: Flow diagram for the program FSWEEP discussed in the text.

mechanical resonance, resulting in an amplitude modulated (AM) output signal proportional to the first derivative of the resonance. At resonance there will be no amplitude modulation of the carrier frequency, although some modulation at 2nd and higher harmonics is present. This can be observed also on an oscilloscope. The phase sensitive detector (PSD) in the lock-in amplifier rejects all signals different from the reference frequency, thus indicating a null reading ($X = 0$) when the carrier frequency is at

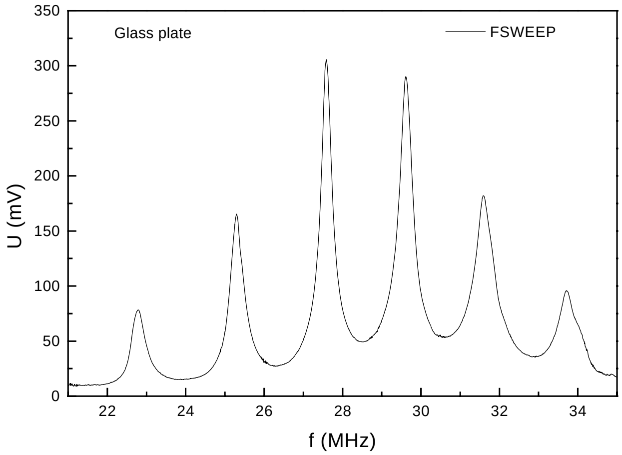

Figure 3.14: Frequency sweep showing standing wave resonances in a 1 mm thick glass plate

resonance[27]. A simple program called XSWEEP record the derivative of the resonances using this principle. The program is essentially the same as FSWEEP presented above. An example comparing the use of FSWEEP and XSWEEP is shown in figure 3.17. The measurement principle and the settings of the apparatus will be further discussed below.

Since measurements have been done at low temperatures (from 4.2 to 160 K), temperature control was an important part of the measurements. The temperature was read by a CGR- or Pt-thermometer as discussed in section 3.2. The difference between the measured and the desired temperature was transformed to a voltage in the computer program and sent via a digital-to-analog converter (DAC) to an analog temperature controller. The temperature controller uses standard PID-control with control parameters manually set by the user. The temperature controller regulated the temperature by controlling the voltage over the heating wire in the sample cell. Typical temperature control accuracy was 10^{-5} K close to 4 K and about 10^{-4} K near 77 K. The temperature control in relation to accuracy

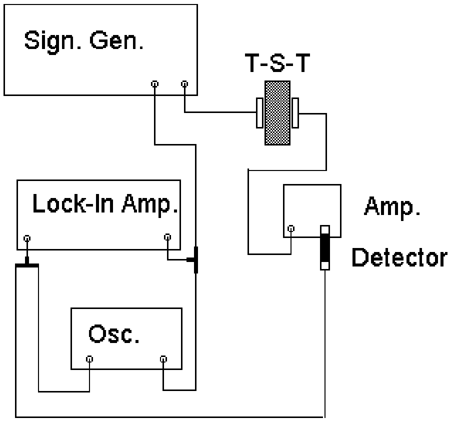

Figure 3.15: Circuit 2 used for frequency sweeps and peak tracing. The circuit contain a signal generator, an ultrasonic composite resonator (Transducer-Sample-Transducer), a RF amplifier, a diode detector, a oscilloscope and a lock-in amplifier. The apparatus are connected via 50 Ω coaxial cables (black lines).

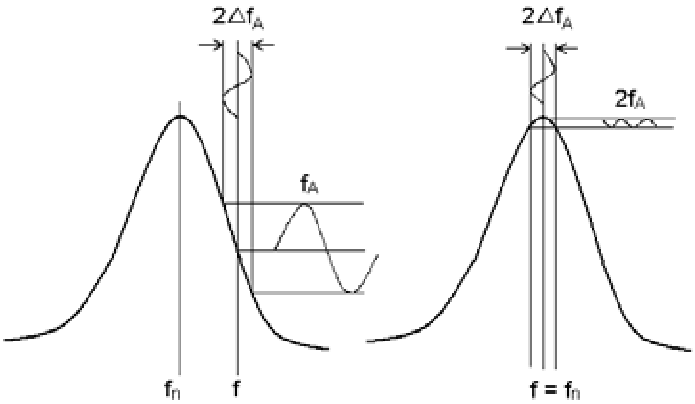

Figure 3.16: The principle behind the measurement method using frequency modulation and lock-in detection. For details see the text.

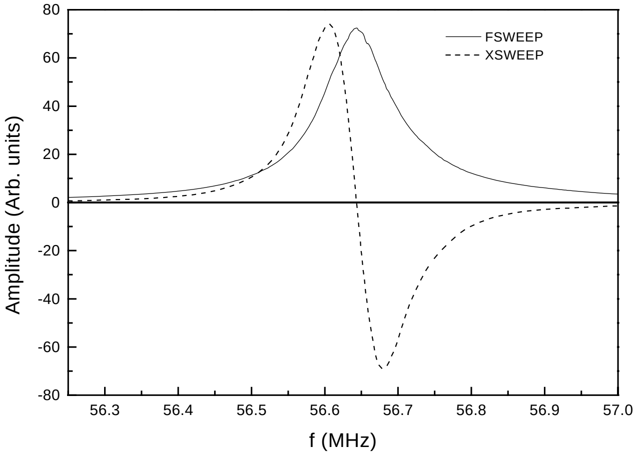

Figure 3.17: Example of frequency sweeps done with the programs FSWEEP (full line) and XSWEEP (dashed line)

of the measurements is further discussed below and also in Chapter 4. The programs FSWEEP and XSWEEP were extended to also include temperature control, allowing sweeps to be measured at arbitrary temperatures set by the user.

Measurements of the relative changes of phase velocity have been done as shown in the flow diagram in figure 3.18. The program used will be named USV here (Ultrasonic (phase) velocity). The main part of the program is a double regulation routine with temperature control on one hand and frequency tuning on the other. Finding the resonance frequency (at a given temperature) with high accuracy also demands a high accuracy of the temperature control. Since the GPIB can only handle communication with one unit at a time parallel processing could not be done. Frequency tuning and temperature control were therefore done in an alternating sequence. In addition to the criterium $X = 0$ at resonance the signal from the PSD should have a negative gradient as shown in figure 3.17. If the gradient is positive a null reading is just indicating a frequency between two resonances. The main loop of the program is going from one temperature to another in steps set by the user. One example of a measurement is shown in figure 3.19. Two different temperature steps are shown here as an example.

There are many parameters in the USV program and settings for the different apparatus which have to be optimized in order for the measurements to be the best possible. We cannot here go into detailed discussion of them all. However, a few important parameters will though be mentioned: The audio signal, used to modulate the RF carrier has both an amplitude and a frequency which are important in the experiments. The amplitude essentially determins the frequency interval over which the FM signal is varying, called the FM level. This is shown as Δf_A in figure 3.16. The audio frequency (f_A) on the other hand is related to the discretization of the frequency spectrum. If the audio frequency is much lower than the FM level the frequency spectrum of the modulated carrier will be approximately flat and continuous[8]. We used typically an audio frequency of 120 Hz and FM level in the range from 20 to 200 kHz. Our experience is that an FM level about half of the half-power band width, δf, is ideal in the peak tracing

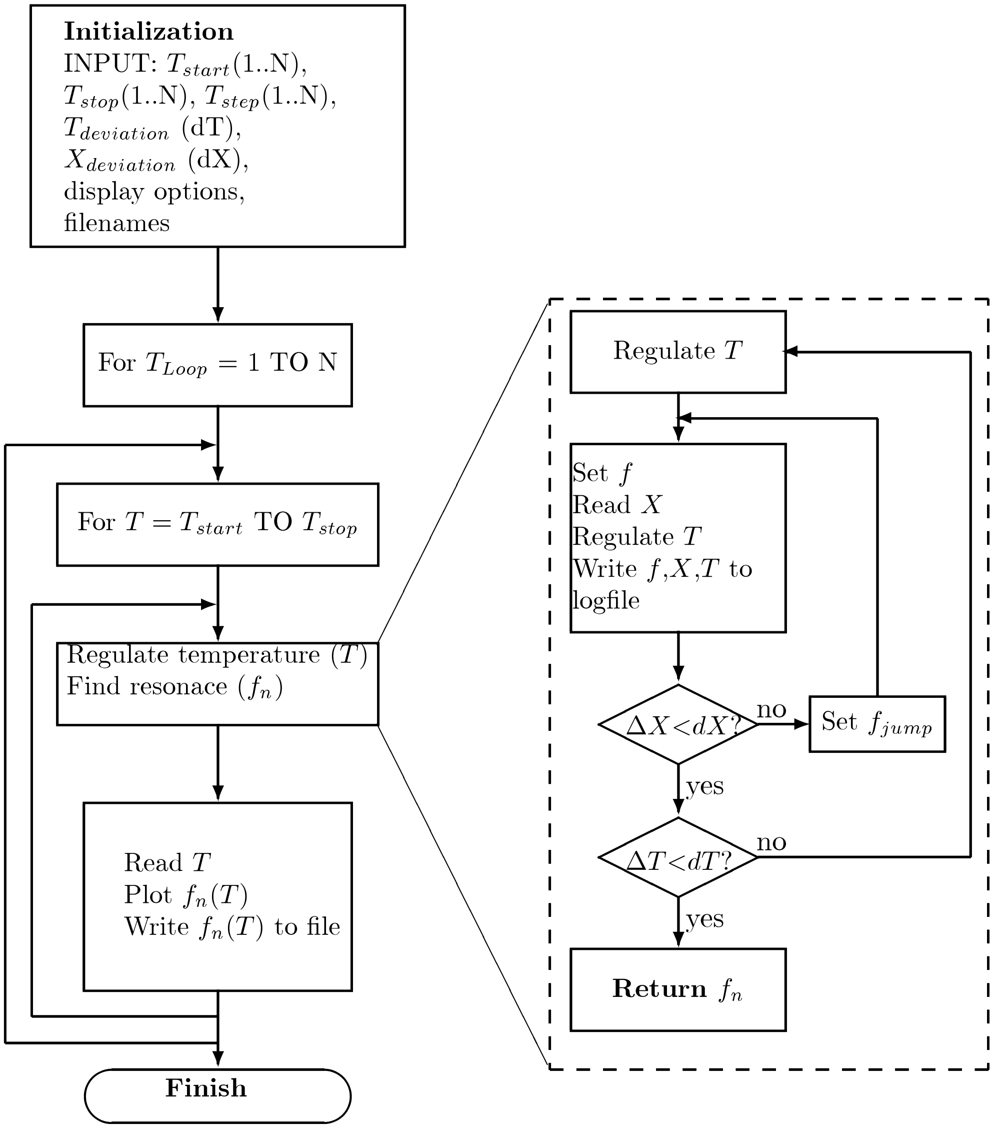

Figure 3.18: Flow diagram for the program USV.

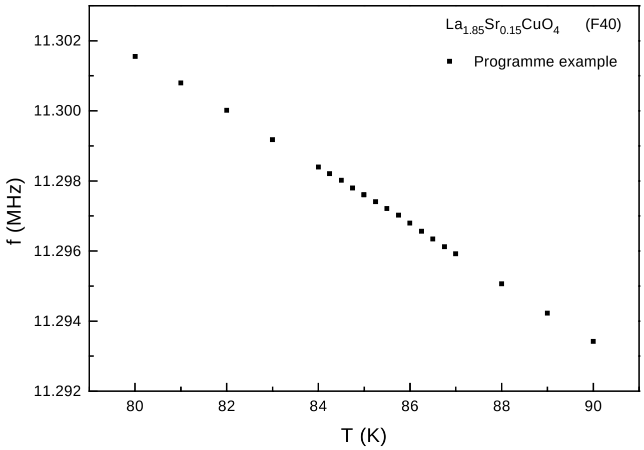

Figure 3.19: Example of peak tracing. The USV program find the resonance frequency for temperatures pre-decided by the user.

measurements. In this case most of the wobbling or other kinds of noise in the resonances were smeared out and at the same time smaller changes in frequency could be found. If the FM level was too big the whole resonance could be smeared out. If the FM level was too low, on the other hand, noise in the resonances could easily ruin the measurements by making 'jumps' in the curves. If the quality of the resonances were too poor these jumps were almost inevitable (see also section 4.3). To better be able to quality-check the measurements afterwords, 'log files' were recorded. The two examples in figure 3.20 and 3.21 are taken from the same measurement shown in figure 3.19.

The log files contain only data measured for temperatures within a small deviation from the desired temperature. For temperatures outside this interval no frequency tuning is done. Only the last part of the temperature control sequence is therefore recorded in the log file. As seen in figure 3.20 there are different sizes of the frequency 'jumps' (called f_{jump} in figure 3.18) as the resonance is approached. The user sets the size of these before

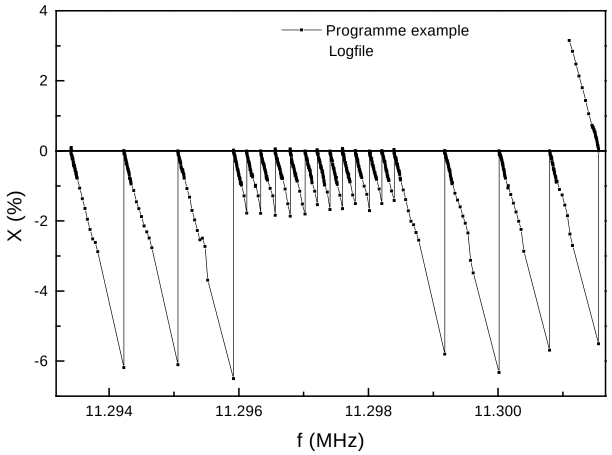

Figure 3.20: Log file plot showing how the program approach the resonance frequency decided by X=0.

each measurement, depending on the Q-value of the resonance, the FM level and the desired frequency resolution. The frequency resolution was also dependent on the time constant and the sensitivity of the PSD in the lock-in amplifier. The output, X, of the PSD could be measured down to 0.01% of the sensitivity (measured in mV). We usually accepted an error of ±0.02% in the measurements, giving frequency resolution as high as ±1 Hz, as shown later in figure 4.6. The temperature was kept constant, within an accepted variation, during a few minutes at each measured point in the measurements using the USV program. Due to the discrete and manual setting of the PID parameters some temperature intervals were measured under better conditions than others. The log files as presented here do not demonstrate this aspect. Often measurements were done during the night without observer attendence. In most of these measurements the PID parameters were chosen such that the temperature interval between about 15 and 40 K had the best temperature control. Outside this interval the temperature would fluctuate more if the PID parameters were not changed.

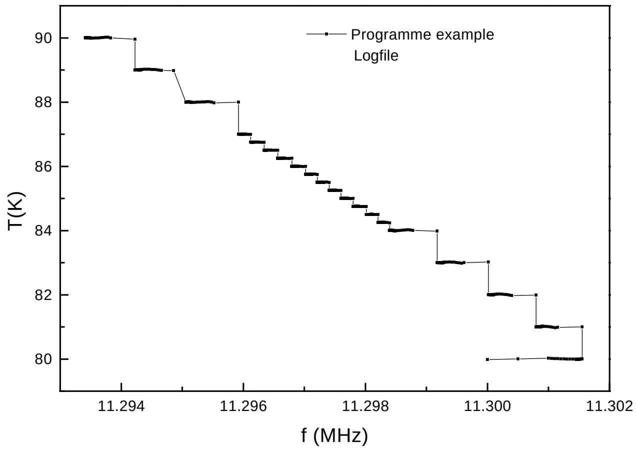

Figure 3.21: Log file plot showing how the temperature is stabilized as the program approach the resonance frequency.

This can be seen in some of the measurements shown in Chapter 4.

As explained in section 3.2 we have also done reflection measurements in addition to transmission experiments discussed so far in this section. The only differences between the two kinds of measurements are the use of a directional coupler and a simpler ultrasonic composite containing the sample and only one transducer. Figure 3.22 shows Circuit 3, which is a variant of Circuit 1. A similar change was done with Circuit 2. All computer programs have been the same in these measurements. A crucial point in the reflection measurements was the impedance matching (IM) of the fourth or 'Isolated' port of the directional coupler. The directional coupler we have used is a socalled 180^o hybrid junction[16]. The other three ports are called Input, Through and Coupled [23]. If the Isolated port is terminated in a 50 Ω termination, then 'all'[17] the power from the Input

---

[16] This kind of directional coupler is often called 'a magic T' due to the symmetry of the ports.

[17] All minus the 3 dB reduction of power between neighbouring ports of the coupler.

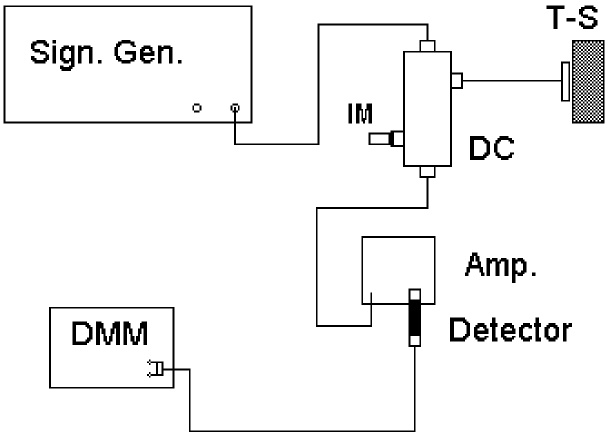

Figure 3.22: Circuit 3 used for frequency sweeps. The circuit contain a signal generator, an ultrasonic composite resonator (Transducer-Sample), a directional coupler (DC), a RF amplifier, a diode detector, and a digital multimeter (DMM). The apparatus are connected via 50 Ω coaxial cables.

reflected at the transducer will exit the Through port. In this case the resonance pattern measured will in principle be inverted with minima for each mechanical resonance. Two complications make the need for a different termination of the Isolated port. First of all standing wave resonances in the coaxial cables will also be measured in this setup as a frequency dependent background. When the sample is cooled, so is also the cable going down to the transducer, and its impedance will change. This makes the background impossible to control in the measurement. The second reason is that the power reflected is often many times higher than what is transmitted at resonance, the signal to noise ratio will therefore often be rather bad. The solution we found, from mainly empirical investigations, was to use another cable with the same length as the one going down to the transducers as an impedance match. This matching cable had to be cooled the same way as the signal cable in order to work at any temperature. The idea is to subtract the contributions from the coaxial cables and thereby measuring only the acoustic composite. As shown in section 4.1.1 in two examples and also in section 4.4 this way of matching worked when done properly. It is not as trivial as it might seem though, and we were not able to repeat the success when we build the new cryostat. Another problem with this setup is to find a theoretical explanation of how this matching really works. It is complicated because there will be multiple reflections when two of the ports are not matched to 50 Ω [23]. We have not been able to really come to a fully satisfactory solution of these problems.

Ultrasonic transducers for pulse-echo experiments are matched to the electric circuit and have often a heavy ‘backing’. The impedance matching will prevent the TEM waves from being reflected, so all the reflected signal comes from the acoustic part of the circuit. The backing prevents the transducer from ‘ringing’ after an ultrasonic pulse has been sent out. In our circuit there is no impedance matching of the transducers, and therefore a big portion of the output power from the signal generator will be shorted to ground over the capacitance C_0 shown in figure 2.3 and 2.4. This was no problem in our case because we used much lower power than the signal generator could give. Complete impedance matching is in reality almost impossible to achieve in this kind of measurement since we vary the frequency over a wide range. The matching would have to be done for each resonance peak to be traced. Another difficulty with matching is that the impedance is changing very much near a resonance peak. In the transmission experiments impedance matching has not been necessary, and in the reflection measurements we did some different attempts as discussed. The transducers should in principal be negligible compared to the sample. When this is the case air-backed transducers, as we have used, will be the optimal case. We see advantages with backing also for the CW-method, but will not discuss these here. Commercially sold transducers with backing[18] are too big for our crystals and they are not made for low temperature measurements.

---

[18] For example from Panametrics Inc.: http://www.panametrics.com/

Chapter 4

Results and discussion

4.1 The apparatus and the method

4.1.1 Experimental experiences

The maybe most critical factor from an experimental point of view in doing research on HTS materials is to get hold of good crystals. Different methods have different requirements and different physical phenomena sets different limits. We will discuss our measurements on HTS materials in the following sections. Here we will take a practical view of the CW-method, but focus the discussion on the requirements given by working with HTSs.

The practical demands were dictated by the following facts: 1) Extremely small, often brittle and 'flaky', samples. 2) Small physical effects, which required very high resolution measurements, with coresponding dimands on the apparatus. 3) Good reproducibility. 4) A wide temperature range in high applied magnetic fields. 5) Samples and transducer polarization to be linearized to a high degree. 6) Bonding effects should ideally be negligible.

The size of a sample became a critical issue in the ultrasonic experiments. The main practical reason for this was the limitation given by the physical size of the transducers. The smallest $LiNbO_3$-transducers commercially available are 0.5 mm in diameter [17]. With coaxial electrodes the practical minimum size will be closer to 1.5 mm. As mentioned in section 2.1.3 the fundamental frequencies of the transducer crystals are inversely proportional to the thickness of the crystals. Fundamental frequencies higher than about 40 MHz would not be useful as the transducer crystals would be too brittle[1]. Ideally the size of the sample should be big enough for the contribution from the transducers to be neglected. We will later discuss the implications of this requirement.

We have used transducer crystals of 3.2, 2.5, and 1.5 mm diameter with fundamental frequencies from about 10 to 30 MHz. We have measured the first odd harmonic resonances for a few unloaded transducers. This was both done as a check of the measurement system and of the theoretical modeling of transducers. One example is shown in figure 4.1 where we have plotted the first and third harmonic resonance of the same longitudinal 1.5 mm diameter transducer. The first harmonic resonance is double peaked, and this was seen for all the seven 1.5 mm longitudinal transducers we inspected. We have also measured the unloaded resonance of two 3.2 mm diameter longitudinal transducers without seeing the double peak. These measurements were done with our apparatus in a reflection measurement, but the very same characteristics were also found using a network analyzer[2].

The Q-factors for the unloaded transducers are much higher than the envelope Q-factors seen in frequency sweeps like figure 3.14. This is also seen in the theoretical analysis (section 4.1.2). The more loaded the transducer is the wider the envelope. As with the transducers the samples will have normal modes more and more widely separated along the frequency axis as the thickness decrease ($\Delta f \propto 1/2l$). If the crystals are too thin, there may be no resonances within the frequency range where the transducer is active. If the crystal is thick enough frequency sweeps can be done for several higher harmonic resonances of the transducer. In figure 4.2 is shown resonance patterns at about 78 K for the LSCO single crystal F40 discussed in section 4.2 and 4.4.

For the moment we will just comment that the double peak seen for

---

[1] The price also increase dramatically above these frequencies

[2] Hewlet-Packard HP8753A Network Analyzer

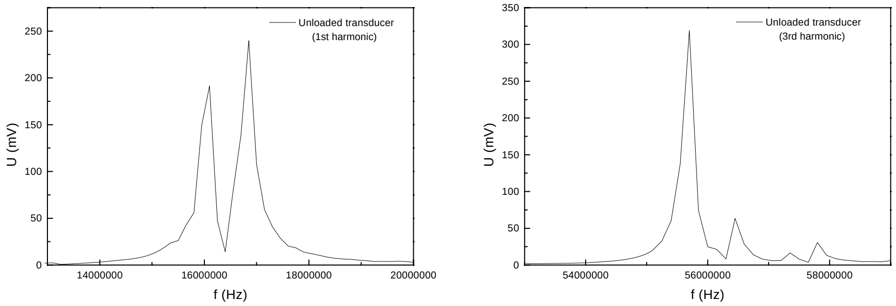

Figure 4.1: Frequency sweep around the 1st(left figure) and 3rd(right figure) harmonic of an unloaded 1.5 mm diameter longitudinal transducer. The shapes of the resonances are somewhat influenced by the frequency step size.

the unloaded transducers (figure 4.1.1) seems to be present also in the first plot, having a double peaked envelope. The transducers used for the sweep in figure 3.14, which has no such feature, showed no double peak when measured unloaded.

The transducer crystals are *acoustically bonded* to the sample, by a material which allows acoustic wave propagation between the transducer and the sample, and hence also prevents the acoustic waves from being totally reflected at the surface of the transducer crystal. Even though longitudinal waves can travel through air the acoustic impedance difference between air and a solid would be too big for significant sinal transmission. Transverse waves are even more demanding to transmit since liquids lack a shear modulus. Still, with a 'thick' liquid in a thin bond shear waves can be supported. There are numerous bonding agents which work at room temperature. Some are better than others but in reality there is no certain rule for what is useful. We have used oil, grease, honey, varnish, paper glue, glycerol and other liquid like substanses with success at room temperature. Cryogenic temperatures are a completely different story. As the temperature is lowered towards LHe-temperatures all substanses, except of course

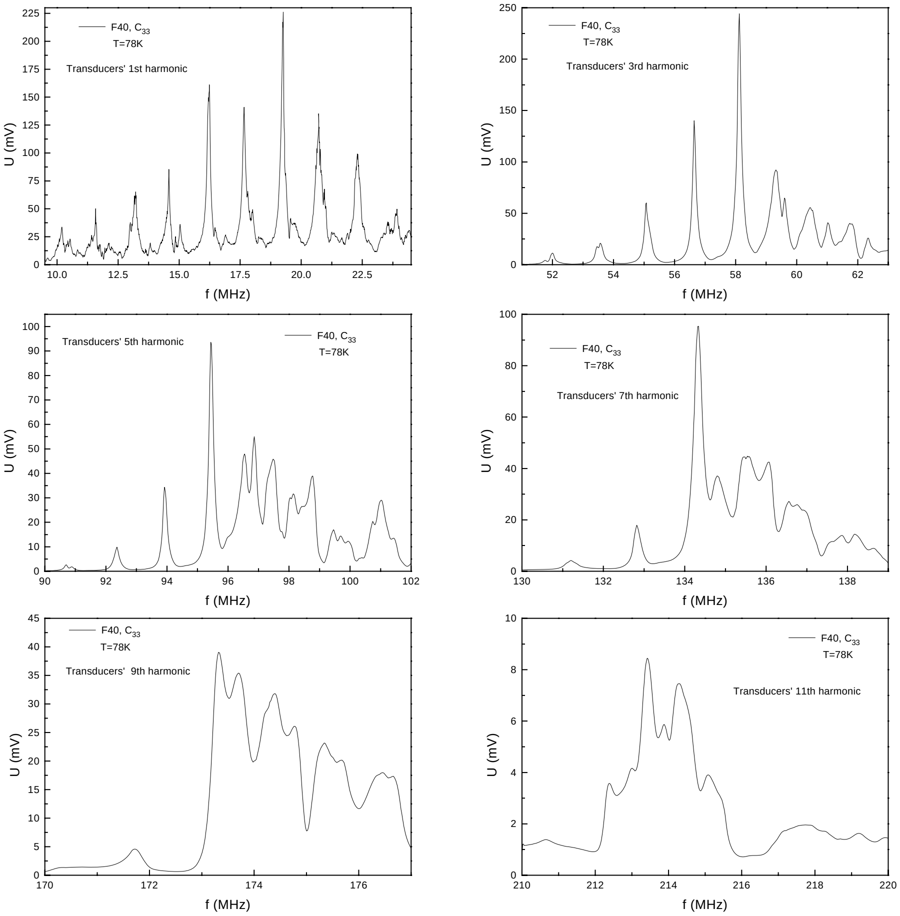

Figure 4.2: Frequency sweep around the 1st to 11th harmonic of the transducers. The longitudinal transducers are mounted on a LSCO single crystal for measurement of C_{33}, as discussed in section 4.2

helium, will finally solidify. From a wave propagation point of view this is advantageous since there will be less difference in acoustic impedance after the bond is frozen and since a frozen bond supports shear waves. However, *bond break* is a serious and frequently occuring problem which very often ruins the measurement. In our experiences bond breaks fall in two categories. Either the bond cracks, or the bonding substance looses contact with the sample and/or the transducer. In either case measurements are interrupted. The bonds are cooled under a changing pressure, since the transducer and the sample have different thermal expansion (contraction)[3] and since the force from the spring loaded gold contacts, discussed in Chapter 3, change as the temperature is lowered. The bond may also change dramatically when it solidifies, and it can have structural changes during further cooling. Of the fifteen different bonding agents we have tested only one turned out to work at low temperatures. Even this one is also quite far from perfect as will be discussed below. Two examples of high and low temperature frequency sweeps are shown in figure 4.3 to illustrate the problem of bond breaks. The bond break seen in the lower right corner of the figure is of the kind were the frozen bond cracks.

When one of the transducers loose contact with the sample no power is transmitted trough the composite. The multimeter will therefor measure at most the threshold voltage for the diode in the detector. What we observe then is a flat signal in the order of 0.01-0.02 mV independent of input power. An electric open circuit would also give the same kind of output, but the reflection measurements can be used to tell the two cases apart. There is really no universal solution to the bond break problem. In the case of 'bond crack' our experience is that it is better to change to a different bonding agent than experimenting with different cooling rates etc. For the 'bond slip' we found that 'roughening' the sample surface a bit gave good results[4]. We will in the end of this section discuss how the reflection method can

---

[3] which may also change dramatically during the cooling process due to structural phase transitions or similar phenomena

[4] We typically scratched the sample very little with a 1200 SiC paper. Just enough for the surfaces to be a bit mate, but not so much that the extreme parallelism of the surfaces were broken.

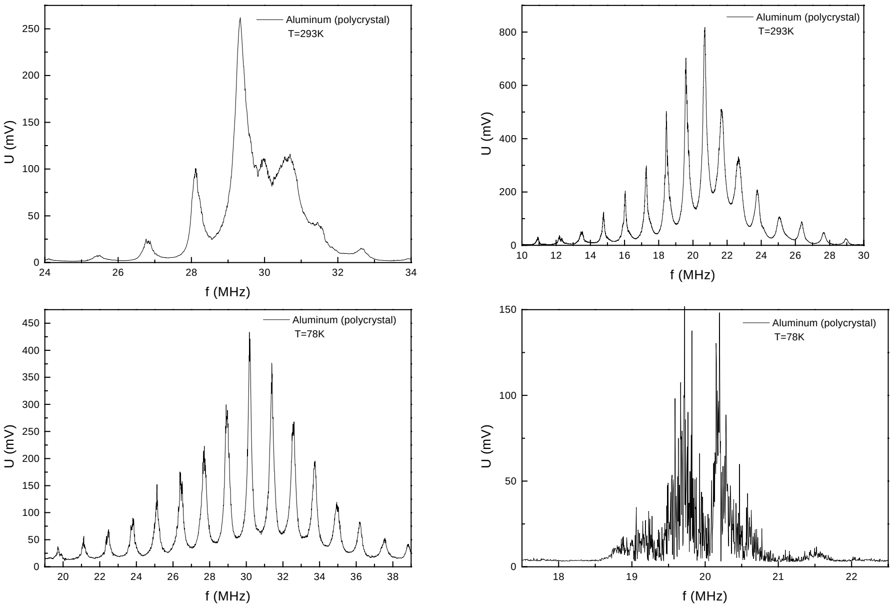

Figure 4.3: Two examples of room temperature frequency sweeps (top left and right) and success (lower left) or failure due to bond break (lower right) at LN_2-temperature. The measurements were done with the same transducers on the same aluminum sample.

give valuable information about the 'origin' of a bond break.

For a given sample the normal modes are the same from measurement to measurement. What is measured on with the CW-method is a composite resonator including also transducers and bonding. Therefore the resonance pattern will not be a 'fingerprint' unique for the given sample. Even taking the same transducers with the same bonding agent on the same sample will give different resonance patters from mounting to mounting. We have put some examples in Figure 4.4. Here the differences are quite big, and show clearly why the bond is a weak point in the measurements.

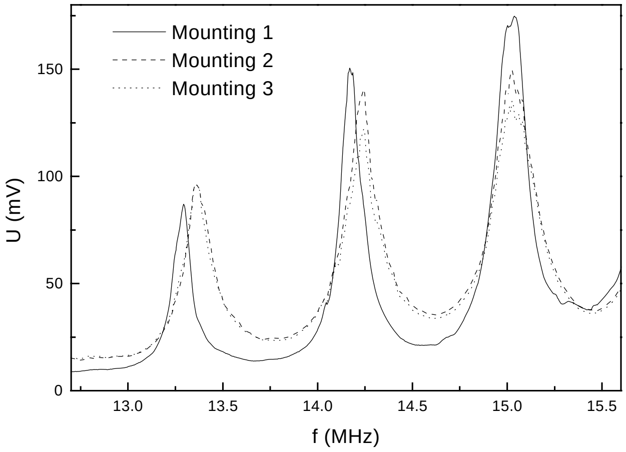

Figure 4.4: Three examples of frequency sweeps where the transducers have been re-mounted between sweeps. The measurements were conducted at room temperature.

The resonances in figure 4.2 also show some effects due to the transducers and the bonding. The left side of the resonance patterns are all very beautiful with clear resonances. The right side, on the contrary, is getting worse for higher frequencies. Our experience is that this effect is connected to the bonding and the mounting of the transducers, without being able to specify really what the problem is. The reason for the extra noise in the first harmonic also remains unexplained. This noise is also seen for the aluminum sample in figure 4.3(lower left).

Another interesting feature with the CW-method which we have seen experimentally and also found theoretically is a frequency pulling effect. This effect is only mentioned with one sentence in the original works [8], while we have studied it both theoretically and experimentally. We have found that the origin of the effect is in the coupling between resonances in the sample and the transducers. As will be discussed in the following section the amount of pulling changes with many factors, but more important is that it can be such a strong effect that the linear theory completely breaks down. One clear example of frequency pulling is shown in figure 4.5. The measurement is done on a 1 mm thick glass sample. The distance between succeeding resonance peeks is shown on the top of the figure.

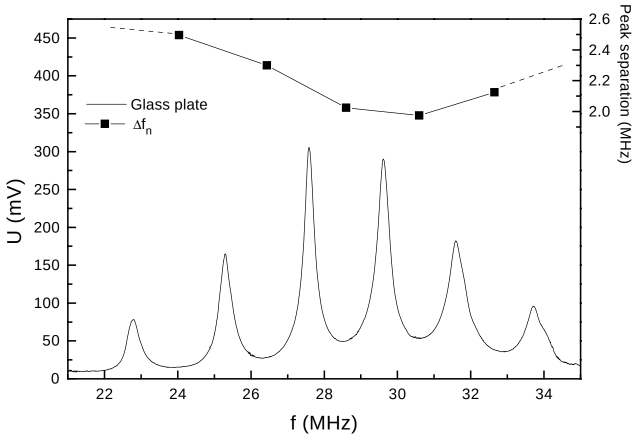

Figure 4.5: Frequency sweep on a 1 mm glass plate showing the frequency pulling effect discussed in the text. The separation between neighbouring peaks are shown on the top of the figure.

As explained in section 3.3, to measure the phase velocity (or elastic moduli) as a function of temperature we trace one resonance frequency.

Using the frequency modulation technique ables us to do this with a very high resolution. What is quite inevitable, based on experiences discussed above, is that the CW-method is not very accurate on the absolute scale. Using several resonances we are able to get an absolute accuracy of the phase velocity within ±1%. The 'recipe' is discussed in section 4.1.2. The extreme sensitivity in the peak tracing is due to the very powerful lock-in amplifier, but also due to the fact that the signal generator has a very high frequency resolution. *The limiting factors are the sample itself and also here the bonding to the transducers.*

Let us substantiate the discussion with a few graphs. In figure 4.6 is shown a frequency sweep, measured with the program XSWEEP, very close to a resonance. The lines at ±0.02% show typical bounds for the lock-in amplifier used in the USV programs discussed in section 3.3. For the example given a resolution in frequency of the order of 10^{-8} (!) could be expected, as shown in the figure.

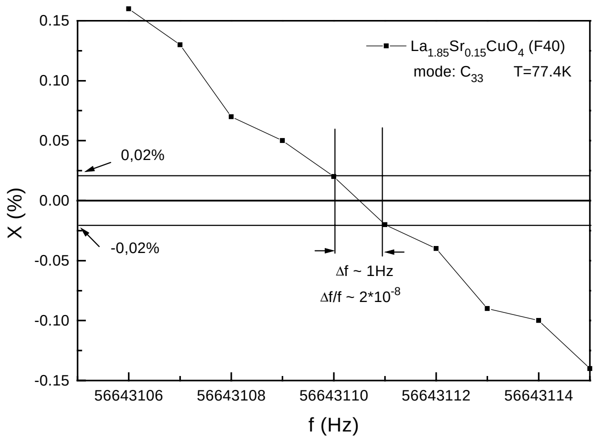

Figure 4.6: Frequency sweep close to a resonance, indicating the frequency resolution in the measurements.

Uncertainty in the temperature control adds new possible errors to the experiments, but as seen in figure 4.7 when the system works well the noise is very low even for temperature steps as small as 10 mK.

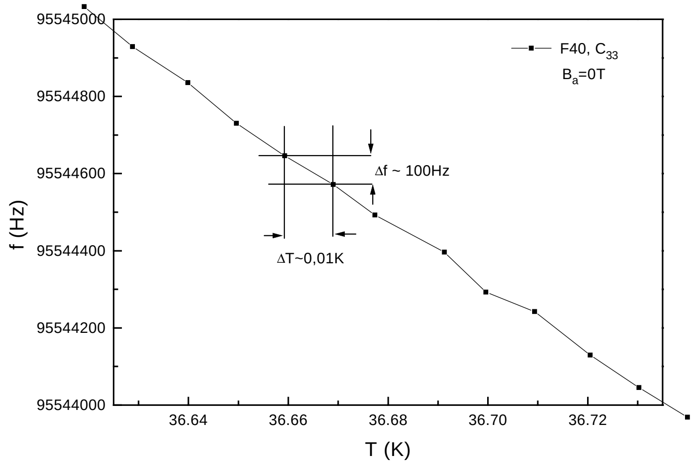

Figure 4.7: Example of peak tracing with temperature jumps down to 10 mK. The measurements are further discussed in section 4.2.

Another example is shown in figure 4.8. The two first curves, labeled (1), were measured in consecutive runs. The third measurement (2) was done later, after many temperature cycles[5]. Even though the temperature steps are very different in all three curves the noise within each curve is much smaller than the separation between them. We have also observed these effects in other measurements at different temperatures and for different samples. The effects are stronger for shear waves than longitudinal waves. Most likely the phenomena have to do with changes in the sample like structural creep, and maybe also the bonding. In the best cases the reproducibility has been on the 10^{-6} scale, but often 10-100 times worse. We will discuss this a bit further in section 4.4.

---

[5] These experiments are further discussed in section 4.2. All the data in different magnetic fields shown in figure 4.22 are measured after the second and before the third curve in figure 4.8.

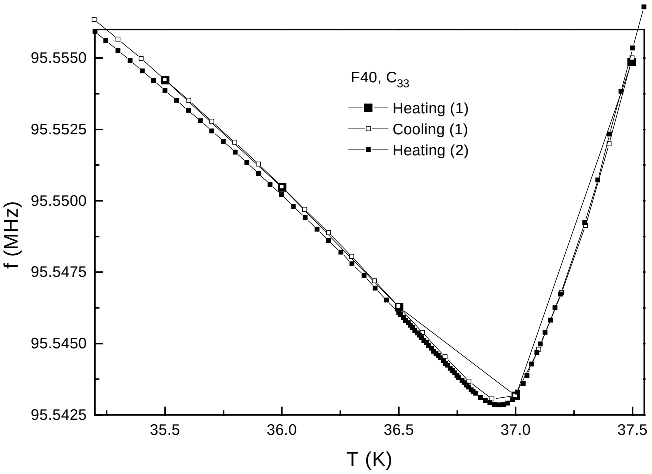

Figure 4.8: Examples of reproducibility of the measurements. Three curves shown with different temperature steps. The upper two curves are labeled (1). They were measured on heating directly followed by cooling. The third curve labeled (2) was measured much later (see the text for details).

A preliminary conclusion of the discussion so far is the following: The resolution of the apparatus in the electric part of the circuit are many orders of magnitude higher than the quality of the samples allow to be measured. The relative change of a resonance can be measured with much higher accuracy than the absolute accuracy of the phase velocity. The acoustic bonding adds extra noise which especially affects the reproducibility of the measurements.

Already from the presentation in section 2.2.2 it was clear that reducing the number of transducers from two to one would be preferable from the acoustic point of view. The bonding problem would be smaller and the mounting situation much easier. Especially in the mounting of transducers for shear waves the advantages of reflection measurements seems clear. Our first cryostat presented in section 3.2 also mainly utilized the reflection technique. The reasons for changing back to a transmission system was explained in Chapter 3.

Here we want to present some of the experience we gathered from working with the reflection technique. In figure 4.9 we show a peak tracing measurement similar to those presented in section 4.2. The data should be compared to those in figure 4.21 presented later.

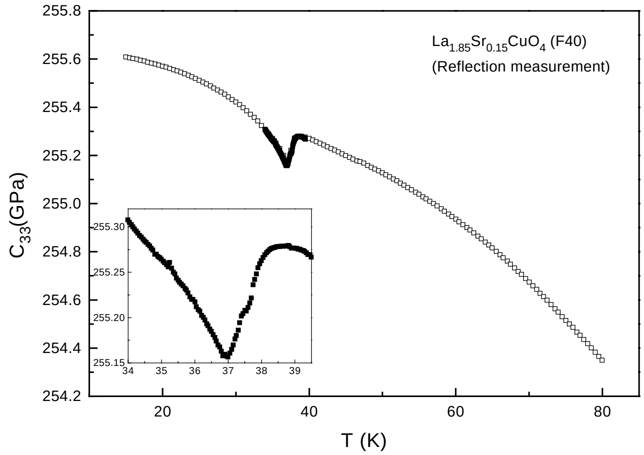

Figure 4.9: Reflection measurements of the elastic module C_{33} for the crystal F40

In figure 4.10 we show a frequency sweep on a 1 mm glass plate. Comparing this to figure 3.14 shows that the resonances have higher Q-values in the reflection measurements, but they are also more asymmetric.

The problems with our reflection cryostat which made us change to transmission measurements were discussed in Chapter 3, but we wanted to emphesize with these examples that the acoustic part of the reflection measurements worked satisfactory. We will show more examples of measurements with this system in section 4.2 and 4.4.

The reflection method can be used in the case of a bond break or other causes of failure to clarify the problem. If there is a bond break in only one of the two bonds in a transmission measurements both of the transducers

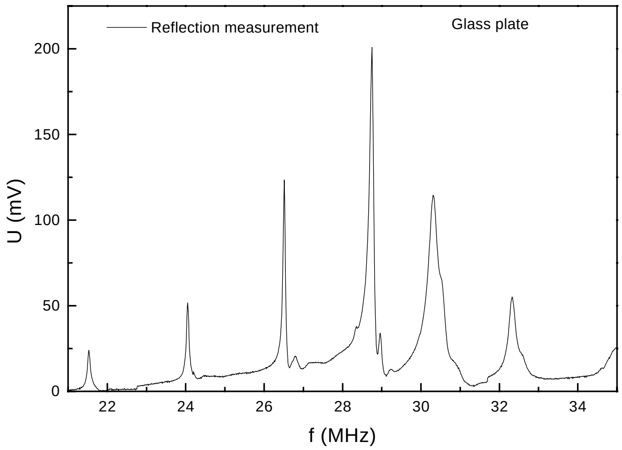

Figure 4.10: Example of frequency sweep using reflection in stead of transmission

would normally be re-mounted, since the user can not tell which one has a break. Using the reflection method one can 'observe' each of the bonds, typically doing a frequency sweep. If the bond is good one would typically observe nice resonances like in figure 4.10, if on the other hand there is a bond break of some kind the measurement would show this in distinct ways. If the bond has cracked the reflection measurements will give the same picture as the transmission measurements. If there is a bond slip the reflection measurement measures only the transducer giving data similar to figure 4.1. Also other obstacles like an electric open circuit can be seen by the reflection method. In this case the output will be flat the same way a bond slip would show up in a transmission measurement. A short circuit is easier found with a multimeter.

So far we have concentrated the discussion on measurements of phase velocity. From the original works of Bolef *et al.*, presented in section 2.2.2, also measurements of attenuation seems promising. The attenuation is related to the Q-value via equation 2.42. In [8] is mentioned a Q-meter which could be used to measure the Q-value as a function of some external parameter like the temperature. We have not made a Q-meter like Bolef *et al.*, but tried to measure $Q(T)$ in two different ways. The first attempt was based on an analogy with a series RLC-circuits where the Q-value is proportional to the height of the resonance peak. From any frequency sweep we can immediately see that this can not be correct on an absolute scale (the peak height follows the bell shaped curve around the transducer resonance), but possibly we should detect changes on a relative scale for a given peak. Our attempts on LSCO have not been successful. The measured data did not consistently indicate the expected changes of attenuation near T_c. The measured Q-value varied so much from measurement to measurement that we had to discard the data. The measurements were done using the simple circuit 1 in figure 3.12. The poor quality of the resonances may have been a major reason for the failure of these measurements[6]. The shape of the resonance changed, not much, but still more than the change of the height. We therefore mainly measured noise in the resonance peak. The second attempt was to use the standard definition of the Q-value $Q = f_n/\delta f$ as we mentioned in section 2.2.2. In these measurements we used the frequency modulation procedure analogous to the measurements of phase velocity. These attempts were not successful either, mainly related to the difficulty of determining the half power width δf. The resonance peak is at its steepest near the frequencies determining δf. The data were too noisy and had to be discarded. The Q-factor for a given resonance peak is clearly not determined solely by the attenuation and phase velocity of the sample, but will change with the attenuation of the transducers and the bonding. We will discuss this furter in the next section.

---

[6] We have not included any plot which really shows the quality of the resonances, but figure 4.4 can be used as an example. Zooming in the resonance peaks revile that all peaks are a bit wobbly. Accurate measurements with circuit 1 is very sensitive to these wobbles, and especially that they change in different fashion when the temperature is changed.

4.1.2 Theoretical considerations of the experimental method

We have based our work on the original theory for the CW-method, which was presented in section 2.2.2. We made no attempts to model the system in a considerably different way. The main difference between our analysis and the one by Bolef *et al.*[8] is our use of computers. We will show how the full model, not linearized as in section 2.2.2, can explain many of the surprising phenomena encountered in the experiments. We have also been able to incorporate bonding as a part of the model. We have done systematic measurements on materials like glass to check the theoretical predictions. Our data show good consistency. The following presentation will be given with focus on the teoretical calculations, in order to be perspicuous.

Figure 4.11 shows a typical frequency sweep calculated by the use of equations 2.44 - 2.46. For simplicity we will refer to this configuration as TST (Transducer-Sample-Transducer). We have plotted the absolute value of the admittance as a function of frequency, giving maxima where the impedance goes to zero. We will discuss the validity of this criterion in the end of this section. Two curves are shown in figure 4.11, one for the phase velocity of the sample $v_S = 6000$ m/s and one with $v_S = 3000$ m/s. All other variables in the model are kept constant. It is apparent from the figure that increasing the phase velocity increases the distance Δf between successive resonances, as expected ($v_S \propto 2l_S\Delta f$). Other features include the difference in amplitude of the two curves, the change in Δf due to the change of velocity not being linear, and changes of both Δf and the shape of the resonances with frequency. In the model plots the calculated curves have been normalized by the maximum value for the admittance of the two curves. A similar plot is seen in figure 4.12 where the thickness of the sample l_S has been varied. The TST model has a whole zoo of variables which need to be inspected. Each element (T or S) has its phase velocity, attenuation, thickness, and density. From them we calculate the characteristic impedances and Q-values which are used in the model instead of density and attenuation (using equation 2.43 and equation 2.42). For the transducers also the resonance frequency is needed as an input parameter. Except for the density all parameters will be different in the

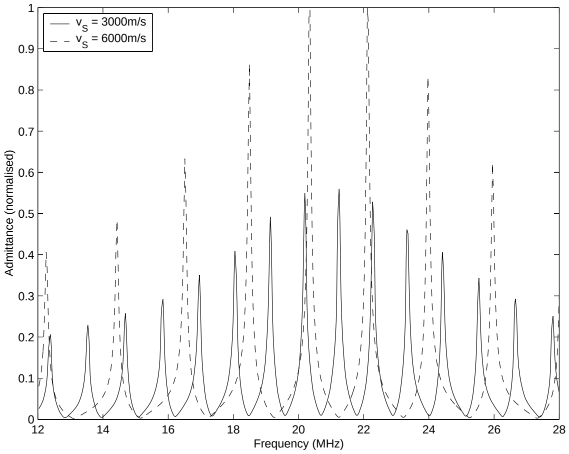

Figure 4.11: Calculated frequency sweeps with two different phase velocities v_S as input parameters

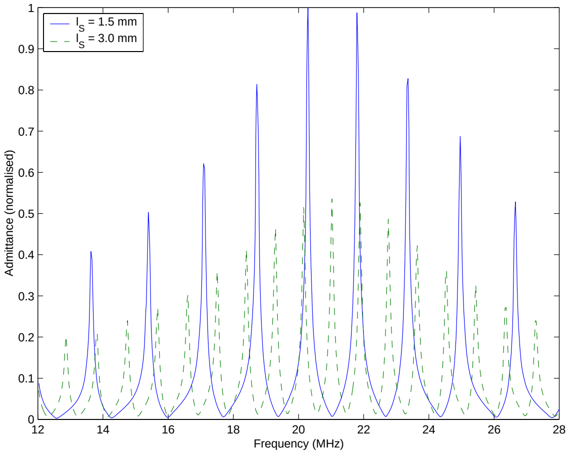

Figure 4.12: Calculated frequency sweeps for two different sample thicknesses

Table 4.1: Parameters for simulations on the Transducer-Sample-Transducer system

Element	*Thickness(l)* [mm]	velocity(v) [m/s]	*Impedance(Z)* [$MRayl$]	*Q-factor* [-]
Transducer(L)	$0.10 - 0.70$	7340	34.1	$10^2 - 10^4$
Transducer(T)	$0.07 - 0.45$	4795	22.2	$10^2 - 10^4$
Sample	$0.2 - 20$	$1500 - 6000$	$1 - 40$	$10^2 - 10^4$

case of longitudinal and transverse waves. In table 4.1 we have listed most of the relevant parameters in the simulations. For some of the parameters (e.g. v_T) only one value is shown. In these cases only this value was used since we have intended to model the experimental situation in the case of $LiNbO_3$ transducers. For other parameters (e.g. Q_S) an interval is indicated to illustrate that the parameter was varied in the simulations to fit measured data or that the values were different for different crystals.

The frequency pulling effect mentioned in the previous section can be explained by the model as exemplified in figure 4.13. We see how a change of the characteristic impedance $Z = \rho v$ alter the resonance pattern. The essential point is that when the difference between acoustic impedance in the sample and the transducer is increased then the frequency pulling gets stronger. However, the frequency pulling will also change with other parameters than the characteristic impedance. The parameter η which was introduced in section 2.2.2 is a good indicator for the situation. It also includes the lengths and phase velocity of the sample and the transducer:

$$\eta \equiv \frac{\rho_T l_t}{\rho_S l_S} = \frac{Z_T l_T v_S}{Z_S l_S v_T} \tag{4.1}$$

If η is small, for a given impedance ratio, then the frequency pulling will be weaker. Conversely when η is 'big' the pulling effect will be stronger. This is typically the case when the thickness of the sample is approaching the thickness of the transducers. In the cases modeled in figure 4.13 and for materials like glass the impedance of the sample is smaller than the impedance of the transducer. In the case of LSCO the situation is opposite.

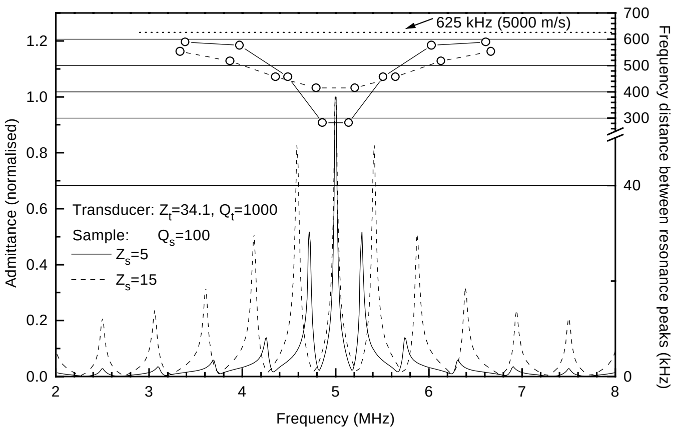

Figure 4.13: Calculated frequency sweeps showing the frequency pulling effect discussed in the text.

The TST model does not seem to give physically correct results if the sample has a higher value for ρv than the transducer. We show this in figure 4.14 where we also have shown a plot for the extended model TBSBT which includes the bond, B. All other parameters are the same in the calculation.

We have included the bonding in the model as a transmission line with the same variables as for transducer and sample. The challenge in doing this is not mathematical, but related to the knowledge of the physical parameters. Phase velocity, Q-factor, and density can be reasonably estimated or even measured. The thickness l_B on the other hand is much more uncertain. It is surely in the micrometer range, but may vary considerably from time to time in the experiments. In figure 4.15 we have calculated two frequency sweeps with bonding thickness 10 μm and 20 μm. What is interesting is that not only is the amplitude affected, but the resonances are shifted and the distance between them is also clearly changed. In most of our calculations the two bonds in the composite resonator were assumed

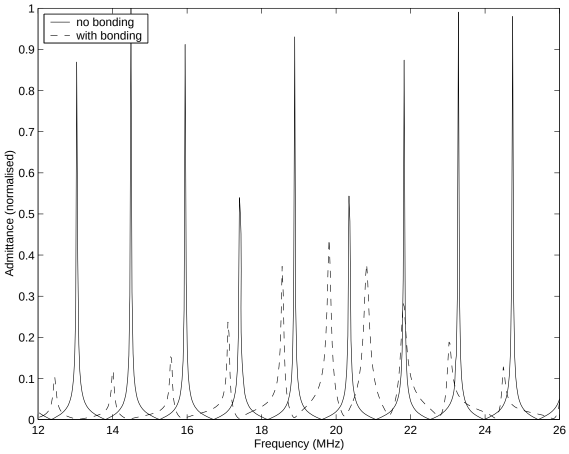

Figure 4.14: Calculated frequency sweeps showing where the characteristic impedance of the sample is bigger than of the transducer. The bonding is included in the calculation to get a physically realistic resonance pattern.

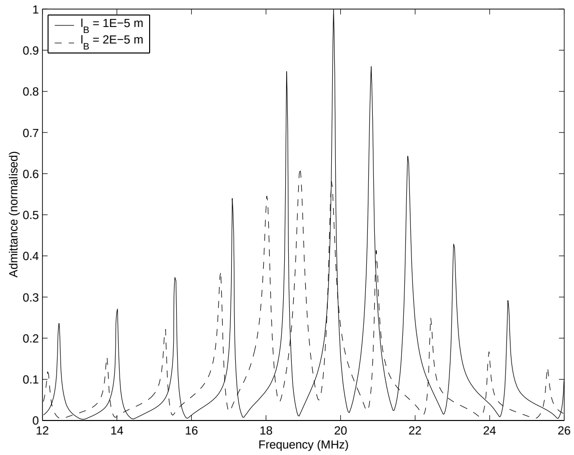

Figure 4.15: Calculated frequency sweeps where the bonding thickness have been varied

to be equal. We have also done a few calculations, not shown here, with different bond thickness. These results give reason for serious concern since they show that the calculated sweeps are extremely sensitive to variations in the bonds. As a final example of calculations with the TBSBT model we show some additional effects which appear when the Q-value of the sample is changed. This is shown in figure 4.16: The Q-values of the resonances are, as an overall feature, changed according to the input value. The center of the envelope is changed a bit, but the resonances are not shifted in this example. A more important point is that the resulting Q-values vary considerably with frequency, with the highest values seen near the center of the sweep.

We mentioned in the previous section that our attempts to measure Q-values as a function of temperature had failed. From the analysis of the model we see new problems in using the Q-value as a measure for the attenuation. This does not really give an input to alter the theoretical modeling since the Q-values there can be looked upon as just a different way

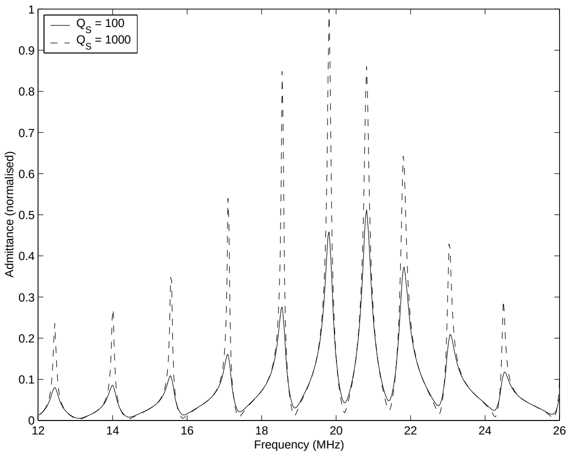

Figure 4.16: Calculated frequency sweeps for two different Q-values of the sample as input parameters

of writing the attenuation. The Q-values determined from the model plots are difficult to relate to the input Q-values both because they change within each frequency sweep as previously described, but also because the resulting Q-values change with most of the other parameters in the model. Here we actually point to the weakest aspect of the whole concept of CW ultrasonics: The strong coupling of all the parameters for all the different parts of the composite resonator makes the determination of physical properties of the sample very inaccurate in absolute magnitude. This does not mean that the CW-method is useless, but that we need to show sobriety in reading our data.

As a final point we will further review the linearized theory discussed in section 2.2.2, and discuss how we in practice have calculated elastic moduli from measured data. The approximations made to obtain equation 2.54 soon fail as $(f^C - f^T)$ is getting large. Only the centrally located two or three peaks can be expected to follow the linearized equations when the samples are small. To avoid linearization one would have to solve equation 2.47, but this can not be done analytically. A graphical solution can be found rewriting it as

$$\tan s = \frac{2\tan t}{z\tan^2 t - z^{-1}} \tag{4.2}$$

where $z = Z_T/Z_S$, $s = k_S l_S$, and $t = k_T l_T$. However, this still gives us less information than the TST calculations we have presented above. Including bond and attenuation into the model the situation is getting even more complicated. Therefor the full TBSBT calculations as discussed previously is the only realistic alternative. In our calculations we generalized the zero impedance criterion in the lossless case to require impedance minima at resonance. Thus we plotted the admittance $|Y| = 1/|Z'|$ as a function of frequency in figures 4.11-4.16. As mentioned in section 2.2.2 we are working with a mechanical equivalence of the whole system. Neglecting the coupling to the electrical circuit we can not expect precise results, but our experiences show that most of the features seen in the experiments can be explained by the model. Probably the most striking difference between the model and the exact system is that in the mechanical analogy also even harmonics of the transducer will contribute. The model is one dimensional, ignoring three dimensional effects which will be more and more important as the size of the sample approaches the size of the transducers. Three dimensional effects are to some extend discussed in [8].

The TBSBT-model as presented can be used to calculate frequency sweeps. In a measurement we are really pursuing the inverse problem; calculating phase velocity etc. from measured data. It is in principal possible to fit measured data to the theory, but this will soon be very time consuming and inaccurate due to the big number of input parameters. For peak tracing measurements the model calculations will therefore not be very useful.

Since LSCO and $LiNbO_3$ have quite similar characteristic impedances we have assumed that the frequency pulling effects can be neglected and we have used the linear theory presented in section 2.2.2 for the measurements on LSCO. To calculate the phase velocity from the measured data $f_n^C(T)$

we have used equation 2.54, rewritten here for simplicity:

$$v_S = 2l_S \frac{f_n^C + 2\eta(f_n^C - f_m^T)}{n} \tag{4.3}$$

Here we have also included the possibility of measuring near any m'th harmonics of the transducer(f_m^T). The parameter η is calculated for the given sample and transducers using equation 2.50. The transducer frequency can be found from the unloaded measurements mentioned in the beginning of section 4.1.1 or, as we often did, be estimated from higher harmonic frequency sweeps. The peak number n is the most crucial parameter in the calculations. There will be a large uncertainty in the absolute value of v_S even for small changes in n. The number n has to be an integer, and will in practice be rounded to the nearest integer found from measured data. Some peaks have more noise than others, we therefore developed a procedure for finding the number n based on peaks from several higher harmonic frequency sweeps. Using the central two-three peaks in up to six sweeps, like those in figure 4.2, we could find the peak distance Δf and from this the integers n to a satisfactory accuracy. Using this procedure we could find the longitudinal phase velocity to an accuracy of ±1% and the shear velocity to ±3%. The elastic moduli were calculated from the phase velocity using $v_{ii} = (C_{ii}/\rho)^{1/2}$ as explained in section 2.1.2.

4.2 Elastic moduli in LSCO

One of our goals has been to investigate parts of the magnetic phase diagram for HTS by means of elastic measurements. Zero-field measurements have been done both as a check of the method and as background for the measurements in an applied field. As discussed in the previous sections the CW-method has some weak points. Both method related difficulties and practical problems appear when the crystals are small. Measurements done earlier on LSCO by other groups, on much bigger crystals and with other ultrasonic methods, will therefor be a natural comparison.

Before presenting and discussing our data we want to emphasize a small difference in notation by different groups. In the early 90's much work was done to investigate the structural phase transitions in different HTS. Among these were ultrasonic investigations[7, 71, 72]. The natural way of naming the measured elastic moduli was to use the room temperature structure symbols even below the structural phase transition temperature. As explained in section 3.1 we have mainly used the low temperature orthorhombic symmetry in naming elastic constants. Our crystals were also mounted under a pressure applied for detwinning. When necessary we will emphasize the differences in notation to avoid confusions. Cutting the crystals has put seviere restrictions on which elastic moduli that could be measured. With the limited amount of crystals avaiable we have concentrated on just a few moduli as discussed below.

4.2.1 Critical fluctuations

The data given in figure 4.17 show the crystal modulus C_{66} measured for the crystal F60. Here the wave vector is parallel to the b-axis and the wave polarization is along the a-axis (See table 2.2). This mode would be named $C_{11} - C_{12}$ in the THT-phase. Our data can be compared with the zero field data in [22] and they have obvious similarities. The elastic constant is increasing as the temperature is lowered. The value increase about 1% in the temperature interval from 80 to 0 K. A minimum is seen near T_c. We will discuss the origin of this minimum below.

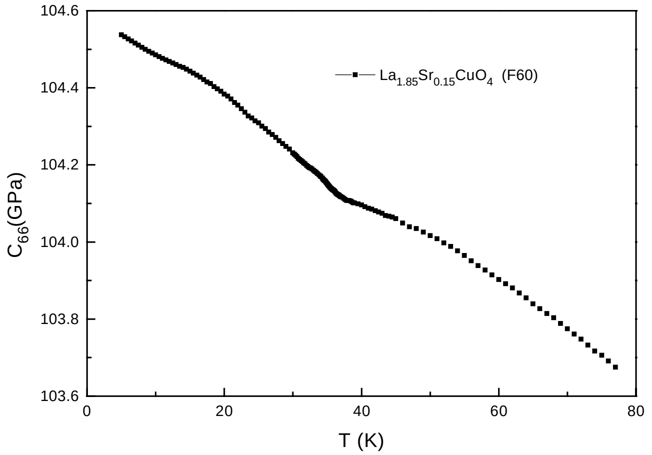

Figure 4.17: Measurement of the elastic modulus C_{66} for the LSCO crystal F60

The data in figure 4.18 show the crystal modulus C_{55} measured for the same crystal F60. Here the wave vector is parallel to the c-axis and the polarization is along the b-axis. In the next figure (Figure 4.19) almost the same measurement have been done for F40, but here with the polarization along the a-axis, resulting in a measurement of C_{44}. Since the a- and b-axes are almost equal, $C_{44}(T)$ and $C_{55}(T)$ should look almost the same. The main differences between the two curves are therefore expected to be due to differences between the two crystals. All three curves shown so far are a bit 'wabbly' in shape. We can not explain this in detail, but belive that changes inside the sample and variations in the temperature control are the main reasons. These details of the curves should therefore be disregarded. We will focus the discussion on the distinct minimum near T_c for the last two curves. This has not been observed earlier in similar published measurements. In [19] and [42] measurements of C_{44}, referred to the tetragonal phase, can be seen. No detwinning had been done in those measurements and the modulus measured had polarization along an axis at

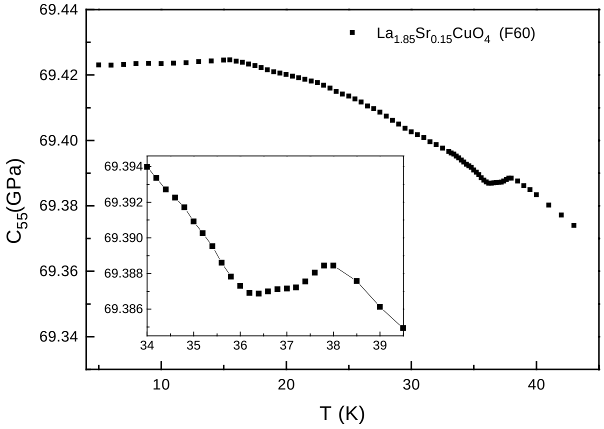

Figure 4.18: Measurement of the elastic modulus C_{55} for the LSCO crystal F60. A closeup near T_c is shown in the lower left corner.

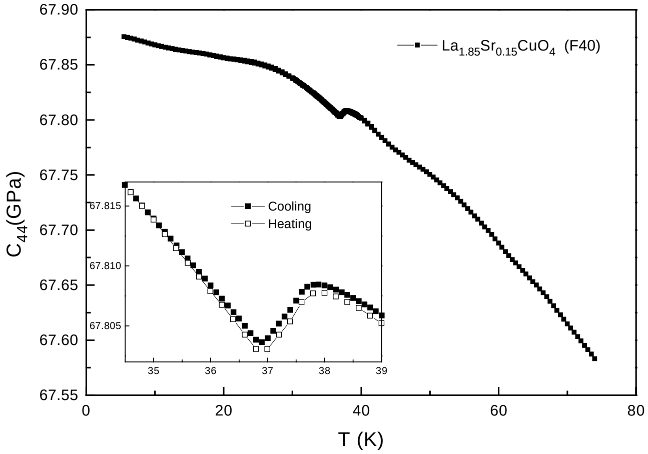

Figure 4.19: Measurement of the elastic modulus C_{44} for the LSCO crystal F40. A closeup near T_c is shown in the lower left corner.

45° to the one we have measured. In an early attempt we measured C_{44}^{THT} using the reflection cryostat. The result shown in figure 4.20 is more similar to the data in [19] and [42], but one can still discern a softening near T_c. We would like to emphesize that the measurements shown in figure 4.20 were not made with the optimised settings of the apparatus as in the rest of the figures in this section. In any case it appears reasonabble to expect that the sharp minimum near T_c will be weaker when the crystals have a higher degree of twinning.

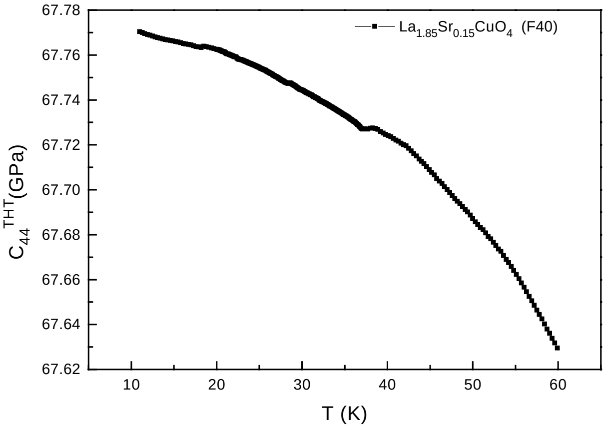

Figure 4.20: Reflection measurement of C_{44}^{THT} for the crystal F40

A mean field analysis of the data can be done using Testardi's theory which we outlined in section 2.1.4. This kind of analysis shows good corespondance with the data except for the temperature interval near T_c[19]. Only the data shown in figure 4.17 could fit into a pure mean field analysis as discussed in [19] and [22]. For the C_{44}- and C_{55}-data the minimum near T_c is too sharp and deep.

Using equation 2.31 Nohara *et al.* [22] also considered fluctuations as an explanation for the minimum near T_c seen in their data. Using a small but positive critical exponent α equation 2.31 predicts a hardening instead of the observed softening and naturally the conclusion did not favour the fluctuation model. In the 3D-XY model the heat capacity exponent is small but *negative*[73, 74], and this gives the expected softening. The shape of the fluctuation peak deduced from the equation is expected to be almost linear in T, which is essentially what we see in our measurement on F40 (figure 4.19). The minimum measured in the crystal F60 is somewhat different from that measured in F40. The difference can to some extent be understood from the susceptibility data shown in figures 3.1 and 3.2. The superconducting transition in F40 is about 0.8 K wide, while in F60 it is almost 10 K. The ultrasonic measurements near T_c should show this difference. What is somewhat surprising and unexpected is that we see a minimum at all for F60 with such a wide transition. The data will be discussed furter in section 4.4 where we study the crystals in an applied magnetic field. As discussed in the two previous sections we need to look carefully at our measurements in order to be sure that we investigate the physics we are really after. Our data discussed so far look almost the same as what was seen by other groups, therefore the overall picture looks reasonable. We do not wish to speculate on why earlier measurements did not show a minimum near T_c as seen here. There are methodical differences, differences in size and quality of crystals etc. which would have to be considered if we wanted to make a detailed comparison. We will instead inspect our measurement system for causes of error. Longitudinal modes, like C_{33} discussed below, are expected to have a minimum also in the mean-field case[19]. One could ask if the measurement somehow included a longitudinal contribution. We belive that possibly the opposite could be the case (that a longitudinal measurement could get contributions from shear modes) since the longitudinal transducers used are quasi-longitudinal (see table 2.1). The shear transducers on the other hand generate no longitudinal modes. The frequency sweeps should also show clear indications of longitudinal modes if they were present. Since the phase velocities for longitudinal and shear waves are quite different this should have shown up in the peak separation in the sweeps.

The last possibility we can see, other than critical fluctuations, seems to be an effect which we presented in section 2.1.4: The thermal expansion also has a sharp change near T_c. Under normal circumstances the sample length shrinks as the temperature decreases. This means that the length of the sample, as used for example in equation 2.54, is slightly changed during the measurement. Usually this effect is about two to three orders of magnitude smaller than the changes in elastic modili[75] and is therefore normally neglected[71]. The minimum near T_c in our data is rather small, and the thermal expansion coefficient have a sharp change, proportional to the change in specific heat, in the same temperature interval[75, 76]. See also equation 2.22. A peak in thermal expansion data does not,however, imply that the sample both shrinks and expands. The linear thermal expansion is proportional to the temperature derivative of the length L_i along the i-axis ($i = a, b, c$) [76]:

$$\tilde{\alpha_i} = \frac{1}{L_i}\frac{dL_i}{dT}, \tag{4.4}$$

meening that the sample rather shrinks at a slower and faster rate in the temperature intervall near T_c.

We will therefore claim that critical fluctuations are the most likely origin of the minimum near T_c in the measurements considered so far.

4.2.2 Critical scaling

The longitudinal mode C_{33} has been measured earlier by Nohara *et al.* [19, 77, 78]. Our data for the crystal F40, shown in figure 4.21, have the same features as seen earlier, but the minimum is a bit sharper and deeper in our data. Similar data were also shown in figure 4.9.

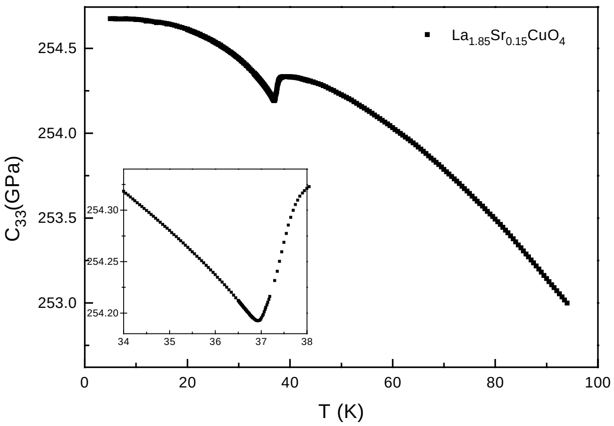

Figure 4.21: C_{33} data for the crystal F40. A closeup near T_c is shown in the lower left corner

We could not measure the modulus C_{11} because the applied pressure along the a-axis (in the orthorhombic phase) prevented attachment of the transducers. The modulus C_{22} could have been measured for the crystal F60, but we have not done this due to other priorities. For measurements of C_{11}^{THT} we would like to refer to [19]. We showed in section 2.1.4 that the deep minimum in the C_{33}-data is mainly proportional to the heat capacity peak, with small contributions from entropy and free energy. It seems therefore likely that we can analyze our data for contributions from critical fluctuations as if we had measured the specific heat. Pasler *et al.* chose a similar strategy when they concluded from thermal expansion measurements that their YBCO crystals had a normal to superconducting transition in the 3D-XY universality class [76].

To investigate the critical fluctuations at the superconducting transition the normal-state background has to be removed. One way of doing this , which is often done with heat capacity data[79], is to subtract data measured in a high magnetic field. Preferably the field should exceed the upper critical field, B_{c2}, in order to keep the sample in the normal state during the entire measurement. With our available magnet of only 5 T a modified strategy is needed. In figure 4.22 is shown measurements of C_{33} in different magnetic fields applied along the c-axis of the F40 crystal. The minimum near T_c is becoming smaller and is shifted to lower temperatures as the applied field is increased. At temperatures well below T_c the elastic

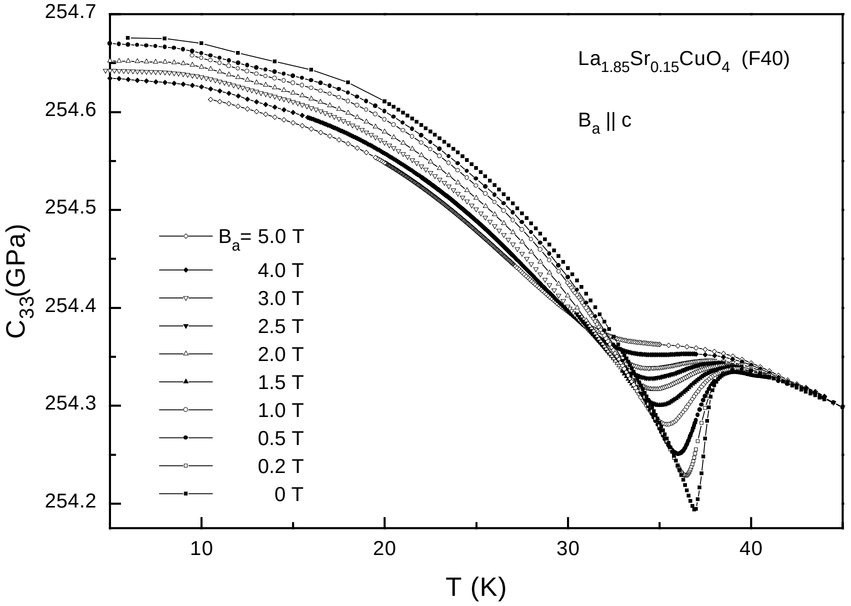

Figure 4.22: Measurements of C_{33} for F40 in applied magnetic fields from 0 to 5 T applied parallel to the c-axis of the crystal

modulus seems to soften almost linearly with the magnetic field. Following Nohara *et al.*[19] we will subtract a background of the form

$$C_N = C_0 + C_2T^2 + C_4T^4 \tag{4.5}$$

where C_0, C_2, and C_4 are constants. The T^4 dependence is ascribed to the phonon contribution and the T^2 dependence from (normal state) electrons. We have done an estimate of the background as shown in figure 4.23. There is clearly considerale uncertainty in this choice, but this should not be a very critical factor in the following analysis. Subtraction of the background has

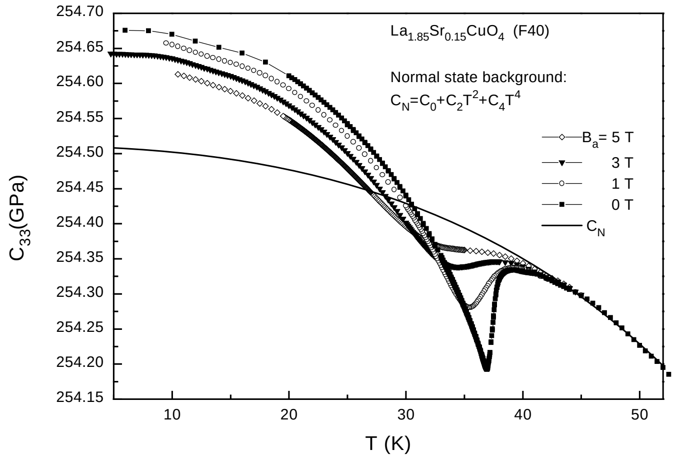

Figure 4.23: Estimated normal state background together with some of the $C_{33}(B_a)$-curves shown in figure 4.22

been done in figure 4.24 (right). Also shown in the figure (left) is a closeup of the data near T_c before the subtraction. The B_{c2}-crossover line can be determined from the data, plotting the peak temperature as a function of the applied field. Before the background subtraction a clear minimum in the curves can only be found up to about 3 T. The background subtraction changes this situation: Each curve now shows a distinct minimum. The

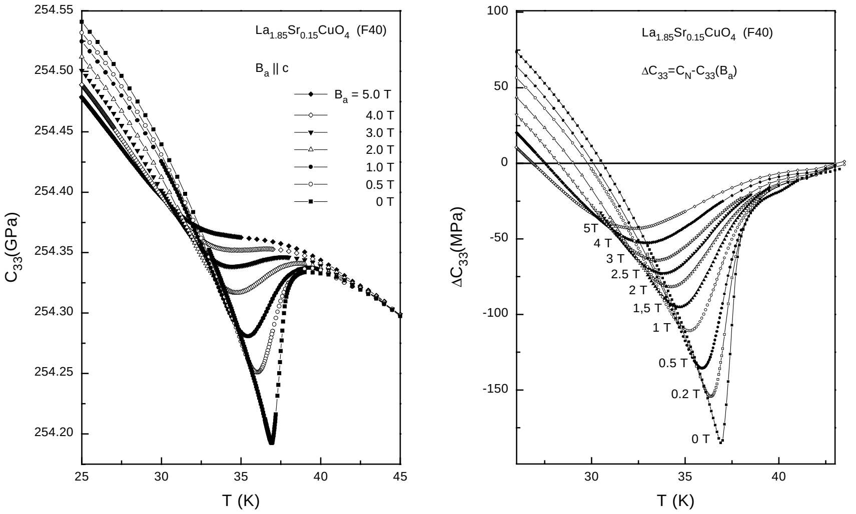

Figure 4.24: Closeup of the C_{33} data shown in figure 4.22, before (left) and after (right) subtraction of the estimated normal-state background

minima are shifted to lower temperatures in the subtraction procedure and this shift is increasing with the value of the applied field. From the 3D-XY model the B_{c2}-line is given by[53, 79]:

$$B_{c2}\ (T_c - T)^{2\nu}, \tag{4.6}$$

with the critical exponent ν given by the hyper scaling relation $2 - \alpha = \nu d$. Since α is almost zero, and the dimension $d = 3$, 2ν will be close to 4/3. In figure 4.25 we have plotted the B_{c2} data taken from figure 4.24(right) together with a least squares fit of the data to the form

$$B_{c2} = a(T_c - T)^b. \tag{4.7}$$

The numerical values of the constants a and b were found to be $a = 0.48 \pm 0.01$ and $b = 1.50 \pm 0.02$ respectively. Also included in the plot is a fit to the 3D-XY model (equation 4.6, with $\nu \approx 2/3$). It is clear from the previous

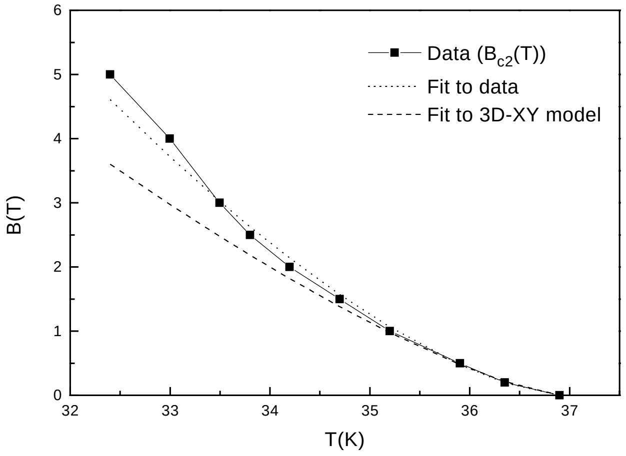

Figure 4.25: B_{c2}-line from the C_{33} data. Also shown is a best fit to the data using equation 4.7 (dotted) and a 3D-XY curve following equation 4.6 (dashed)

discussion that for lower fields the background subtraction is affecting the B_{c2} data much less than at higher fields. For example a fit for the data below 2.5 T gives the b-value 1.43 compared to 1.50 for the entire range. From figure 4.25 one can see that our 3D-XY fit shows the best correspondence with data at low applied fields. We will argue that our data are consistent with 3D-XY scaling in the lower field range, but we do not exclude at this point that the data also might be consistent with other models. Gaussian fluctuations would show a linear dependence ($b = 1$ in equation 4.7)[79], which is clearly further away from the observations. A different procedure for finding the exponent ν is to rescale the axes of the graphs in order to collapse the data onto one curve. This has been done for specific heat data, mainly on YBCO, by many groups[80, 81, 82, 83, 84], from the very beginning of the HTS era. The main discussions have been on 3D-XY versus 3D-LLL scaling. There seems to be no clear consensus even though data and the theoretical approach in treating them have been much of the same. Scaling procedures found in the literature is applicable for specific heat and magnetization measurements. It is not straightforward to extend this approach to our C_{33}-data even though the elastic modulus is roughly proportional to the specific heat near T_c. We will make an attempt, but disregard the magnetic field dependence and focus instead on the data measured in zero field.

The specific heat, for a sample in a continuous phase transition, has a singular part of the form[74, 76, 85][7]:

$$C_p(t) \sim A^{\pm}|t|^{-\alpha} \tag{4.8}$$

with t being the reduced temperature $t \equiv (T/T_c - 1)$ and $A^{\pm}$ the amplitude above (+) and below (-) T_c. In principle α and $A^{\pm}$ could be determined directly by plotting the data on a log-log scale. This would require a very high accuracy near T_c, but since the transition is broadened by inhomogeneities in the sample this approach fails[85]. To extract the critical behavior despite the broadening, we ignore the rounded part of the cusp near T_c and

---

[7] Alternative forms are $C_p/T \sim A^{\pm}|t|^{-\alpha}$, or $C_p(t) \sim \frac{A^{\pm}}{\alpha}|t|^{-\alpha}$ with similar singular behavior [85, 76]

use the tails of the peak to extract the critical exponent α. Mathematically this can be achieved by expanding equation 4.8 in a power series of $\ln|t|$:

$$C_p(t) \sim A^{\pm}|t|^{-\alpha} = A^{\pm}\exp(-\alpha \ln|t|) \simeq A^{\pm}(1 - \alpha \ln|t|), \tag{4.9}$$

a procedure which should be reliable as long as $(-\alpha \ln|t|) \ll 1$ and t is not too close to zero. From this it is apparent that plotting $C_p(t)$, or a quantity proportional to C_p, on a semilog scale, ignoring values with t close to zero, one should find two straight lines. The lines should have slopes $-aA^{\pm}\alpha$ and separation $\Delta = a(A^{+} - A^{-})$ where a is a constant. Taking the ratio of the slope and the separation defines the universal number

$$J = \alpha^{-1}\left(1 - \frac{A^{+}}{A^{-}}\right) \tag{4.10}$$

A practical problem in this kind of analysis, when the transition is broadened, is to find the correct T_c. Common practice [76, 85] is to adjust T_c until the branches are as straight as possible, keeping T_c higher than the peak temperature T_p. We would like to emphasize that this procedure will affect the value of J, and we have therefore plotted three curves, figure 4.26 - 4.28, with T_c from 36.95 K (T_p) to 37.75 K (T_c in the susceptibility measurements). We have indicated the two straight lines used in the scaling, together with a dashed line corresponding to the value $J = 4$ found for ^{4}He [74, 76, 79]. The vertical axes show $\Delta C_{33}/T$ in arbitrary units. We have subtracted the background as shown above and divided by T to have data proportional to C_p [8]. Before we analyze the critical exponents found from the semi-log plots, we would like to comment on some other details in the figures. The upper branch in the plot, which is most rounded, belongs to data below T_c. The branches meet, outside the plots, in T_p. The specific heat data shown in [74] for ^{4}He and in [85] for YBCO have the low temperature branch as the most linear one. The thermal expansion data

---

[8] The data have also been multiplied with constant values found in [19] for the molar volume and the strain derivative of T_c in order to get the data in correct units for C_p. Since this is no essential point and since it does not alter the values of J, $A^{\pm}$ or α we have not focused on this here.

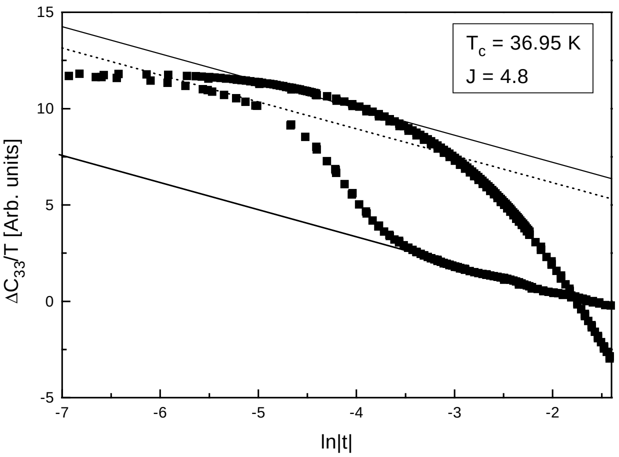

Figure 4.26: Semi-log plot for the background-subtracted C_{33}-data discussed in the text. T_c is chosen to be 36.95 K

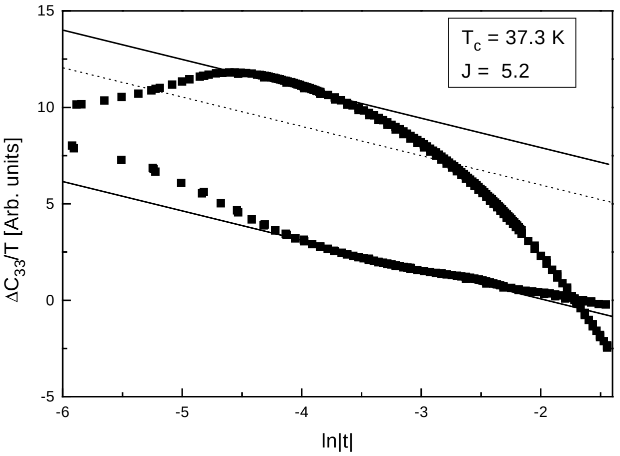

Figure 4.27: Semi-log plot with T_c=37.30 K

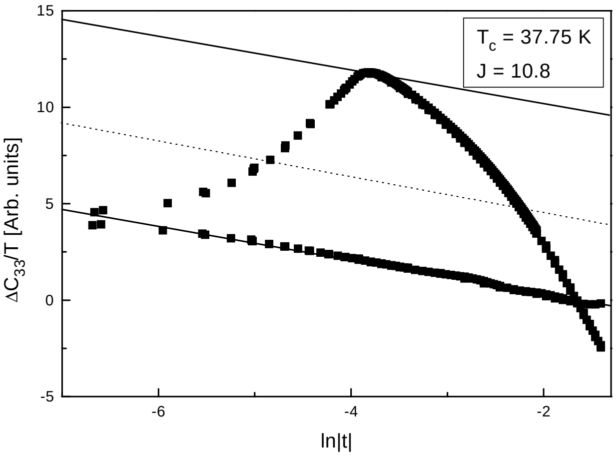

Figure 4.28: Semi-log plot with T_c=37.75 K

for YBCO in [76] are, on the other hand, more similar to our data. The downward rounding in the critical regime can be attributed to mean field contributions[76]. According to equation 2.26 these contributions can be expected to be caused by changes in entropy and free energy.

In the semi-log plots we expect the analysis to be valid roughly for $0.4K < |T - T_c| < 4K$, corresponding to $-4.5 < \ln t < -2.2$. The transition is rounded over 0.8 K giving ± 0.4 K as the lower limit. The critical fluctuations should be observable to $\sim \pm 10\%$ of T_c, which is about 4 K for the crystal F40.

A best fit to our data would give $J \sim 5$ - 6, which is 20-30% higher than the value obtained for ^{4}He. Pasler *et al.* found $J = 6$ from their thermal expansion data on YBCO[76]. Junod *et al.* [79] discuss specific heat measurements for 16 crystals of YBCO, $EuBa_2Cu_3O_7$ (EBCO), $DyBa_2Cu_3O_7$ (DBCO) and BSCCO, focusing on the values obtained for J. They conclude that only optimally doped YBCO has $J = 4$ and represent an exception belonging to the 3D-XY universality class. We will agree with Junod *et al.* that the values obtained for BSCCO, $J \sim 0.2$-0.8, gives critical exponents not consistent with 3D-XY scaling. However, we will argue that for example $J = 6$ gives consistent values, and that $J = 4$ should not be used as such a sharp criteria for 3D-XY behavier.

For the above analysis we do not have enough equations to determine all the unknowns J, $A^{\pm}$, and α. Common practice is therefore to assume 3D-XY values[9] for either A^+/A^- or α and from the measured J-value calculate the last unknown using equation 4.10. With J for example in the range 2 to 6 we get $-0.027 < \alpha < -0.009$ when A^+/A^-=1.054, and $1.0257 < (A^+/A^-) < 1.0771$ when $\alpha = -0.01285$. All these values are close enough to conclude that they are consistent with 3D-XY behavior[10]. There are only minor differences from the ideal case, and we cannot hope to do much better under the given experimental conditions. Other models discussed in [79] include 2D- and 3D-Gaussian fluctuations and 3D Bose-Einstein condensation for the charged boson gas. All these other models have values for α and A^+/A^- which are far away from the values discussed here, and therefore represent no real alternative to the 3D-XY model in this context. We stress again that BSCCO seems to be very different than YBCO or LSCO and agree with Junod *et al.* that the conclusion might be different for BSCCO[11]. We will mention one more model with critical exponents not too far away from the 3D-XY model. What we have in mind is the 3D-Heisenberg model with $\alpha = -0.115(9)$ and $\nu = 0.705(3)$ [73]. Why this model should be more appropriate than the 3D-XY model must be argued on theoretical grounds[12]. We cannot see that any model fits our data better than the 3D-XY model and must therefore conclude that it seems like the most reasonable model for explaining our data.

---

[9] We will use A^+/A^-=1.054 and $\alpha = -0.01285$ measured by Lipa *et al.* in ^{4}He [74].

[10] Even $J = 11$ is consistent with 3D-XY scaling. This value gives $\alpha = -0.005$ which could be compared to the RG calculations in [73] giving $\alpha = -0.007(6)$

[11] One difference with BSCCO compared to LSCO and YBCO is that for BSCCO is the coherence length, ξ_c, smaller than the layer distance, s. A more 2D like behavier will therefore be expected[3].

[12] A discussion on amplitude fluctuations in the order parameter which could be relevant to this is found in [86].

4.2.3 Critical dynamics

As discussed in section 2.2.2 the CW-method should in principle give the speed of sound independent of which resonance one is tracing. Working at different frequencies will on the other hand give some additional information if some other length scale is of relevance. An example would be a polycrystal with grains, say, on the micrometer scale. For low frequencies (long wave length) the crystal would look isotropic and homogenous to the measurement. With wave lengths on the order of the size of the grains this would definitively not be so. The resonance frequencies is not just inversely related to sample length, but also represent a time scale for probing of sample dynamics. Dynamics at some time scale, like a relaxation time, could therefore also be investigated by measuring at higher or lower frequencies, corresponding to shorter or longer time scales respectively. We have measured C_{33} for different frequencies following one resonance peak within each of the six odd harmonics (1st - 11th) for the transducers. The corresponding frequency sweeps are shown in figure 4.2. We have printed the six curves in figure 4.29. We have shifted the data by a constant amount in order to separate the curves. The resonances in the 1st and the 11th harmonics had a much higher noise-level than the others. Near T_c the following features are still clearly seen in figure 4.29: i) All the curves have the same minimum T_p. ii) The lower the frequency the sharper and deeper is the minimum. Discussions of our data have so far been focused on critical fluctuations, and it is tempting to do this again. The reduction of 'peak height' with increasing frequency is a very interesting feature, revieling the presence of critical dynamics near T_c. This is particularly interesting, since sound velocity is usually frequency independent at these frequencies. Critical fluctuations are characterized by both a diverging length and time scale on approaching the phase transition temperature. Thermodynamic equilibrium is needed to observe this. Qualitatively one can argue that the lower the frequency in our experimentes the more we should expect to see of critical fluctuations and the deeper and sharper the softening will be. Conversely, the higher the probing frequency the less of the long time and long wavelength fluctuations are beeing felt by the soundwave. A similar kind of critical

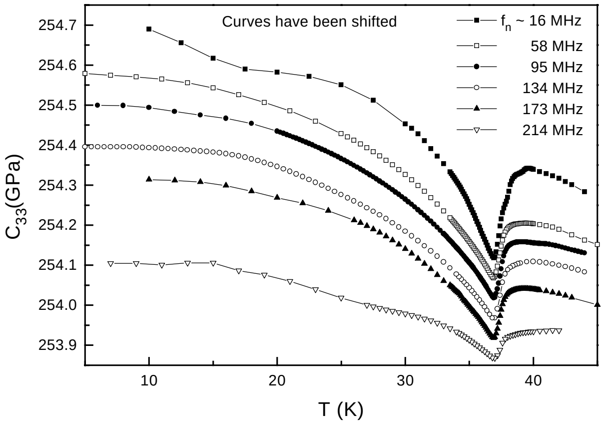

Figure 4.29: Measurements of C_{33} for frequencies in the range 16 to 214 MHz. The curves have been shifted by a constant to make the plot more clear. The scale on the C_{33}-axis follow the 95 MHz curve.

dynamics has previously been observed at structural phase transitions [87]. The physics here is similar in a broad sence, involving probing of fluctuations in the order paramater by acoustic waves. On a more detailed level we would need to consider a particular model. The 3D-XY model is one such choice with vortex loops as the relevant fluctuations[54, 55, 56]. This is a dynamic system with loops of different sizes blowing up at T_c in zero field, and at a phase boundary in the vortex liquid state in finite field. Without a theory of how ultrasonic waves would interact with these loops, we would in any case expect higher frequencies to be less effective than lower ones in probing the dynamics.

4.2.4 Low temperature behavior

We are left with one clear feature seen in figure 4.22 not discussed so far. For temperatures below the critical region, the elastic constant appears to have a linear dependence of the applied magnetic field. We show this in figure 4.30 where the zero-field data have been subtracted from the data in a magnetic field. The zero-line in the graph corresponds to the zero field data. The linear dependence of field is apparent over a wide temperature range, but for clarity we have plotted the average separation in the low temperature region as a function of applied field in figure 4.31. We would like to stress that from a theoretical point of view the measurements does not probe any elastic moduli of the FLL since the flux lines are compressed and stretched in the field direction. In a finite crystal with pinning one could maybe expect small contributions from c_{44}, but the measured change in C_{33} is *negative* and can therefor not be explained by a *stiffness* of the FLL. Since this behavior is characteristic for the low temperature region mean field analysis can be used. The thermodynamic relations presented

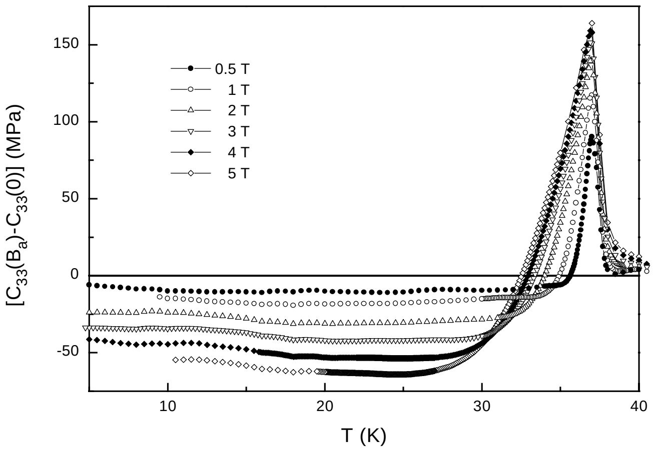

Figure 4.30: The $C_{33}(B_a)$-data subtracted from the zero field curve.

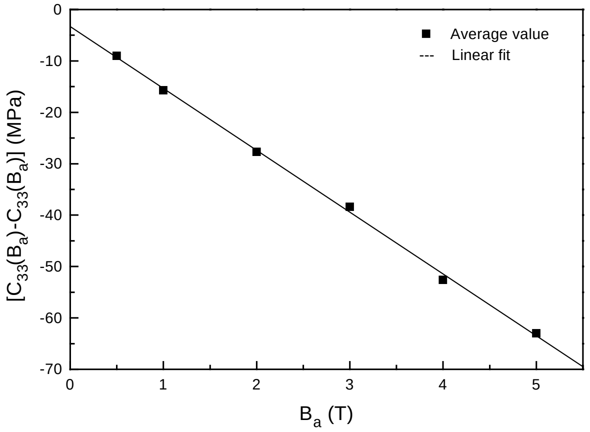

Figure 4.31: Average separation of the low temperature part of the curves shown in figure 4.30, a linear fit (full line) indicates the linear dependence of the applied field.

in section 2.1.4 will be our first approach. The behavior seen in figure 4.30 seems to act unchanged down to $T = 0$ K. Using equation 2.26 with $T \to 0$ we are left with only the last term proportional to the difference in free energy:

$$\Delta C_{33}(0) = \left(\frac{1}{\phi} \frac{d^2\phi}{d\varepsilon_3^2} \right) \Delta F(T) \tag{4.11}$$

We have no analytical expression for the free energy and do not know which field dependence the prefactor might have. We will therefore give a simple arguments based on the Gibbs free energy[13].

The difference in Gibbs free energy between the normal state and the superconducting state can be defined by the following relation:

$$\Delta G(T = 0, H) = G^N(0, H) - G^S(0, H) = -\int_0^{H_{c2}} M dH \tag{4.12}$$

The magnetic fields we are discussing here are much higher than H_{c1} and lower than H_{c2}. In this field range the magnetization is almost constant, since $H_{c2} \gg H_{c1}$. Therefore

$$\begin{aligned} \Delta G_S(0, H2) - \Delta G_S(0, H1) &= G_S(0, H2) - G_S(0, H1) \\ &= -\int_{H1}^{H2} M dH \\ &\simeq const \cdot (H2 - H1) \end{aligned} \tag{4.13}$$

Where $H1$ and $H2$ are magnetic fields in the range we have measured. The magnetization is very small in HTS, making the internal field B almost equal to the applied field B_a. The Helmholtz free energy should therefore approximately behave in a similar manner to the Gibbs energy.

From this and previous discussions it seems likely that at low temperatures (up to 20-30 K) contributions from the free energy is mainly

---

[13] The Gibbs energy because it is related to the H-field (B_a) and the stress (σ) controlled in the experiment.

determining the behavior of our data. Near T_c the specific heat is most important, while the contribution from entropy have a maximum in the intermediate region.

A more physical picture is necessary in order to get a deeper understand. We have roughly explained the linear behavior but not really why the crystal softens with increasing amount of flux lines. If we look at the stiffness in the FLL, the line tension in each flux line or the energy associated with contracting and elongating flux lines we will get positive contributions which should show up as a stiffness in the experiments. More flux lines on the other hand means that a bigger volume fraction of the crystal is in the normal phase. It therefore seems likely that the appearance of superconductivity favor the Cu-O planes to keep their distance more rigidly. In other words; changing the interlayer distance is unfavorable to superconductivity.

4.3 Elastic moduli in other HTS compounds

We have made some attempts to measure elastic moduli in other single crystals than the two LSCO crystals discussed in the last section. Susceptibility-data and other characteristics were shown in section 3.1. From a superconductivity point of view all crystals seem interesting for these measurements. They have different anisotropies, transition temperatures, amount of pinning, size etc. Except for LSCO the literature is also almost void of data when it comes to ultrasonic measurements on *single crystalline* high temperature superconductors[14]. Our attempts have been seaverely limited by lack of adequate crystal quality. This is a universal problem in HTS research when crystals of some size (a few mm^3) is needed. We have used the LSCO measurements as a comparison. Therefore, even though we could possibly have measured 'something', and clearly even better than what has been done before, we have not gone much further with crystals for which we could not have gained much insight on the problems we have been interested in.

For the small YBCO crystals of good quality availble to us on the world scene we have managed to measure only one resonance, and only at room temperature. At low temperatures the peaks disappeared or we clearly had a bond break. The main problem was that the crystals were of the same size or smaller than the transducers. The normal mode resonances in the samples were too separated, and we measured mainly the transducers.

We have done a few measurements on the BSCCO sample NO970822. The best frequency sweep and the best peak trace is shown in figure 4.32. Only raw-data is shown.

If we compare our data to the measurements by Wu *et al.*[88] we see that the noise level in our measurements are many times lower. The data seems also reasonable if we compare them to the LSCO data. There is no clear minimum near T_c, but this may be understandable, since the peak in specific heat for BSCCO is known to be much smaller than for LSCO or YBCO[79]. The peak is also much more rounded. The sample NO970822 has a T_c of

---

[14] We have found only three(!), though there might be a few more

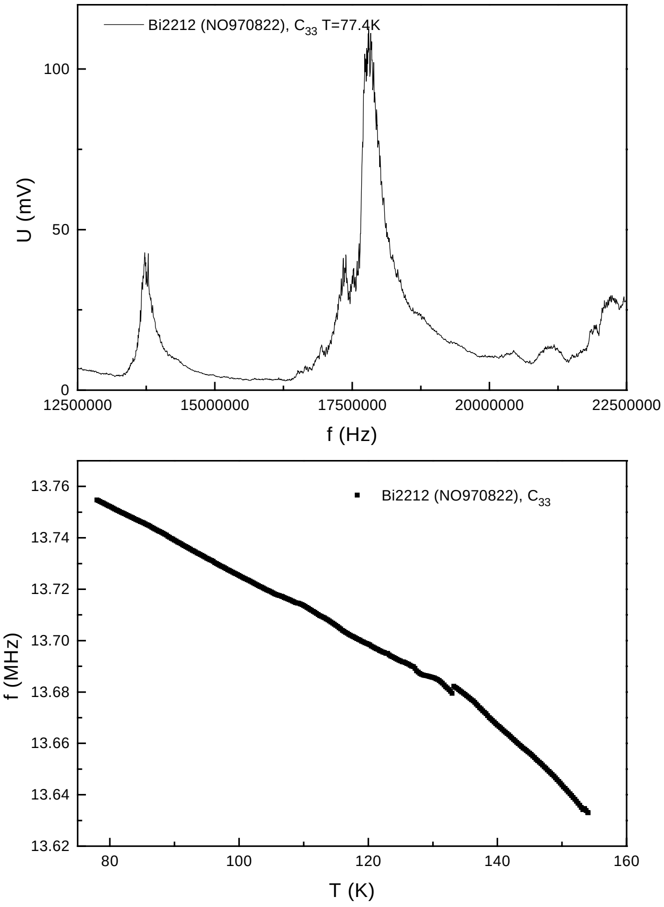

Figure 4.32: Frequency sweep (upper) and peak trace (lower) for the BSCCO sample NO970822.

about 83 K, which is near the left end of the graph. The measurements were made with liquid nitrogen as a coolant, but due to technical problems we could not lower the temperature by pumping. Later inspections showed that the 'crystal' really consisted of three pieces grown together; very unfavorable to ultrasonic measurements. It was also extremely brittle, and later attempts to measure on it were not successful.

The next and last data we will present in this section have been measured on one of the NBCO samples (WAX 144-1). Also here raw-data is shown, but for a sweep only. The data is shown in figur 4.33. The mode measured is a quasi (C_{11},C_{22})-mode. The crystal is heavily twined and have no clear a or b axis. What we measure is a Longitudinal sound mode parallel to the ab-planes. A peak trace was made but due to 'jumps' in the curve, which did not represent any real physics, data were disregarded. The jumps reflected only the poor resonance and how the measurement criteria (X=0) depended on this.

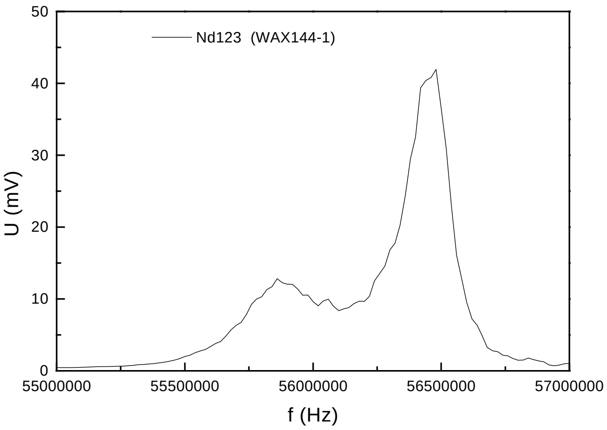

Figure 4.33: Frequency sweep for the NBCO sample WAX144-1.

4.4 Elasticity of the flux-line lattice

In section 2.3.3 we made a short review of the last few years exploration of the physics of the vortex liquid. As mentioned, the real proof of the existence of a melting transition would be to measure a total softening of the shear modulus. The original motivation for this project was to reveal this fundamentally important process. Based on equation 2.60 and 2.61 we can estimate numbers for the magnitude of the shear modulus. We rewrite the two equations here as a reminder:

$$c_{66} \approx \frac{B\phi_0}{16\pi\lambda_{ab}^2\mu_0} \tag{4.14}$$

$$c_{66}^h = c_{66}\Gamma \tag{4.15}$$

In choosing a sample, based on the underlying physics of these equations one is looking for a material with short penetration depth, λ_{ab}, and a high anisotropy, Γ. One problem is to obtain correct values for a given sample. Values for both λ_{ab} and Γ vary a lot in the literature, even for a given material with a given doping. As for all measurements on HTS the variations are due to differences in sample composition, quality and experimental methods.

The material with the highest anisotropy to which we have had access is BSCCO. An estimate based on the values $\lambda_{ab} \sim 2000$ Å [89] and a field of 5 T gives: $c_{66} \approx 4.1$ kPa. With $\Gamma \sim 150$ [90] we get $c_{66}^h \approx 0.6$ MPa.

As the previous discussions have shown, we have not been able to measure elastic moduli in other materials than LSCO. A first estimate with $\lambda_{ab} \sim 800$ Å [89] and a field of 5 T gives: $c_{66} \approx 25.6$ kPa. Which is even bigger than the value for BSCCO. Later we have found that 800 Å probably is an underestimate for λ_{ab}. For optimally doped LSCO the value is measured to be about 2400 Å (See [91]). The anisotropy Γ of LSCO is strongly doping dependant, but always lower than values for BSCCO. A reasonable estimate for optimally doped LSCO is $\Gamma \sim$ 20-30 [63]. We found $\Gamma^2 = 617$ for the crystal F40 as explained in section 3.1. Therefore we expect c_{66}^h to be of the order 0.1 MPa for the crystals F40 and F60. As pointed out by Pankert [40] there are at least two very good reasons for using ultrasonics for these kind of investigations. First, ultrasonic measurements are real bulk measurements which means that surface effects, and grain-boundary effects in the case of poly crystals, are of minor importance. The other reason is that the ultrasonic waves will move the flux lines away from their equilibrium positions by at most 10 nm (typical sound amplitudes). Choosing ultrasonic measurements as the tool for measuring c_{66}^h, the number 0.1 MPa, which we calculated, needs to be compared to the size of the elastic moduli of the crystal itself. From table 2.2 we see that this means comparing to C_{44} or C_{55}. In section 4.2 we found these to be of the order of $\sim 70\ GPa$. We therefore need to be able to measure a relative change $\Delta C_{ii}/C_{ii} \sim 1 \cdot 10^{-6}$ by the ultrasonic method. We made an attempt to measure c_{66}^h very early in the project, as shown in figure 4.34. The main figure shows a closeup near T_c, the whole curve is shown in the lower left corner. The typical separation of the two curves measured in zero field and in an applied field of 5 T is in the range of 0.1-0.5 MPa. Looking at the

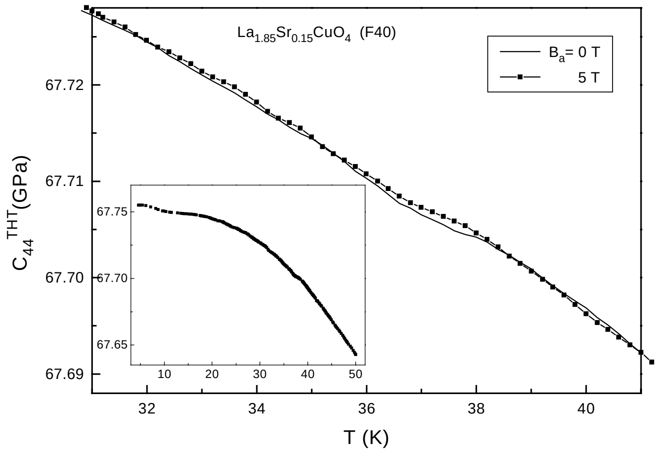

Figure 4.34: Attempt to measure the FLL modulus c_{66}^h superimposed on the modulus C_{44}^{THT} of the crystal. For details see the text.

graph it is apparent that the noise is of the same size.

The tilt and compression moduli, c_{44} and c_{11} respectively, are orders of magnitude bigger than the shear modulus (about 20 MPa for B=5 T) We therefore wanted to measure c_{44} as a check. Measurements had been done in the past[42] which were consistent with the theory discussed in section 2.3.2. One of our first measurement series can be seen in figure 4.35. In contradiction to the data by Fukase *et al.*[42], the curves here show two steps instead of one. By subtracting the zero field curve to obtain c_{44} we

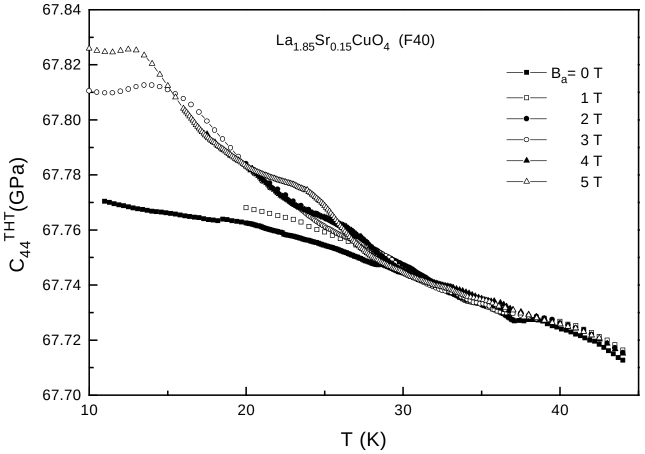

Figure 4.35: Reflection measurement of the modulus C_{44}^{THT} for the crystal F40 in different applied fields. The configuration is such that the FLL modulus c_{44} should be measured. The details are discussed in the text.

found what is shown in figure 4.36. Only data measured in 3 T and 5 T are shown. From the discussion in section 2.1.4 and 4.2 it appears that this kind of subtraction is not necessarily correct. Superconductivity itself will contribute in addition to the flux-line lattice on top of the normal state background. For measurements in the past[19, 40, 42] the contribution from superconductivity seemed to be absent or extremely small for C_{44}^{THT}. As we discussed in section 4.2 we observe both mean-field contributions

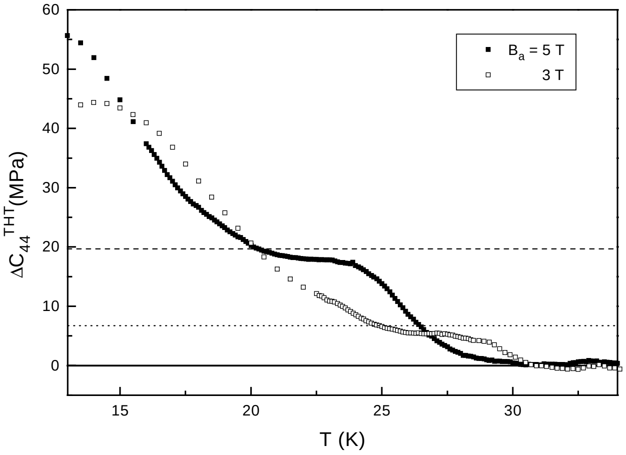

Figure 4.36: The 3 and 5 T curves shown in figure 4.35 with the zero field curve subtracted as a background. The dashed and dotted lines indicate the zero temperature value B^2/μ_0 for the tilt modulus c_{44}

and critical fluctuations in our data. For the present discussion we will regard figure 4.36 as mainly showing $c_{44}(T)$. The two straigt lines, hatched and dottet, in the figure represent the theoretical zero temperature value of B^2/μ_0 for the two curves. The lower plateu, just below the lines, seems to represent mainly the elasticity of the fluxline-lattice[15]. Using equation 2.63 we could have fitted the data in the interval from the lower plateu to T_c to obtain the depinning energy, as was done in[42]. The low temperature part of the curves on the other hand lack an explanation. The measurements presented so far in this section have all been taken with the 'reflection system' discussed in section 3.2. There were serious practical problems with this setup which is also reflected in the fact that so few of the measurements shown in figure 4.35 were completed. We made a much better system (section 3.2) and measured the tilt modulus again, this time also with the crystal detwinned. Our data is shown in figure 4.37. New quetions arise when looking at the zero-field and 1 T curves, while the other curves show the same behavier as earlier. To begin with, we show in figure 4.38 only the data with B_a from 2 to 5 T for temperatures between 5 and 30 K. The two-plateau nature of the data is apparent. For this crystal at least this kind of behavior seems to be manifest. The zero-field and 1 T curves on the other hand are troublesome. They seem inconsistent with the other curves, especially below 15 K. We suspect creep in the material to be at least partly responsible for this. The zero-field and 1 T curves were the two last measured in this measurement series. Inaccuracy in the temperature control, due to not optimal PID settings at low temperatures (discussed in section 3.3), could also be important. The zero field curve can definitely not be subtracted as a background the way we did to obtain figure 4.36. To gain more insight we did essentially the same measurements on the crystal F60. The results raised even more questions. The data are shown in figure 4.39. The data appear to be much more similar to the data in for example[42]. Does this indicate that the F40-data are non-physical? A closer look at figure 4.39 show that the difference between the 5 T curve and

---

[15] Also the data for the other applied fields (1, 2 and 4 T) are consistent for the lower plateu.

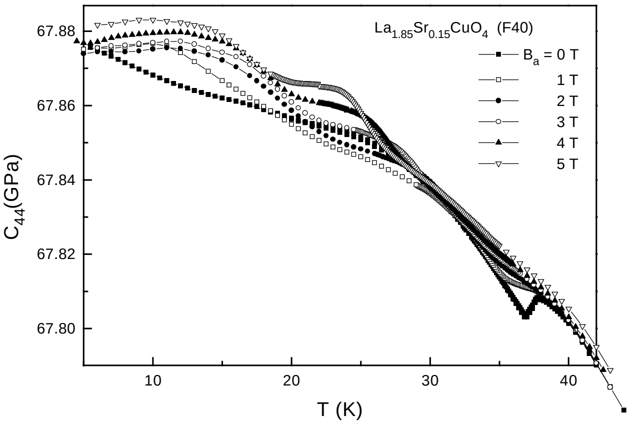

Figure 4.37: Transmission measurements of C_{44} in applied magnetic fields from 0 to 5 T applied along the c-axis of the crystal. Details are discussed in the text.

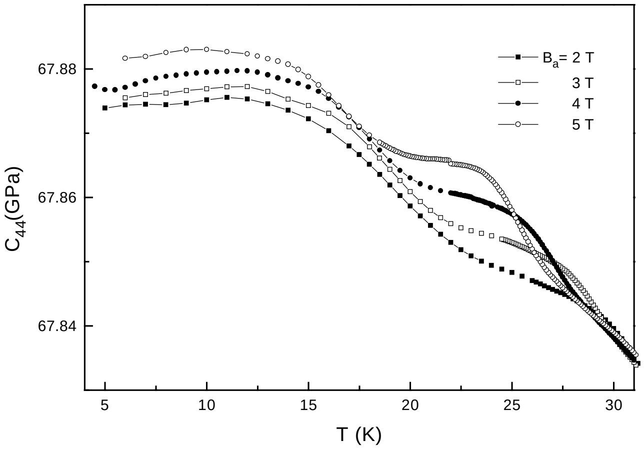

Figure 4.38: The lower temperature region for the data in figure 4.37 with B_a ranging from 2 to 5 T

the zero-field curve is of the order of 50 MPa as $T \rightarrow 0$. Under the clearly questionable assumtion that this represents c_{44}, what we just calculated is at least twice as much as the theoretical value. We belive the data for F60 are more similar to the F40-data than it seems at first. It appears that the essential difference between figure 4.39 and 4.37 is that the first plateus, seen for F40, have been smeard out in the F60 data. The susceptibility data shown in section 3.1 indicate that this is not unlikely to happen. The pinning situation in the two crystals is also quite different.

We showed a series of magneto optical images for the crystal F40 in section 3.2. These measurements were taken at 30 K. As a comparison, figure 4.40 shows the same crystal measured at the maximum field 50 mT at 18 K (left) and at 35 K (right). The field is parallel to the c-axis of the crystal. At 18 K almost no flux penetrate the sample at all. At 35 K, on the other hand, we observe full penetration at this field.

The crystal F60 shows a quite different behavier than F40. In figure 4.41 is shown images at 18 K in a field of 20 mT (left) and 30 mT (right) parallel

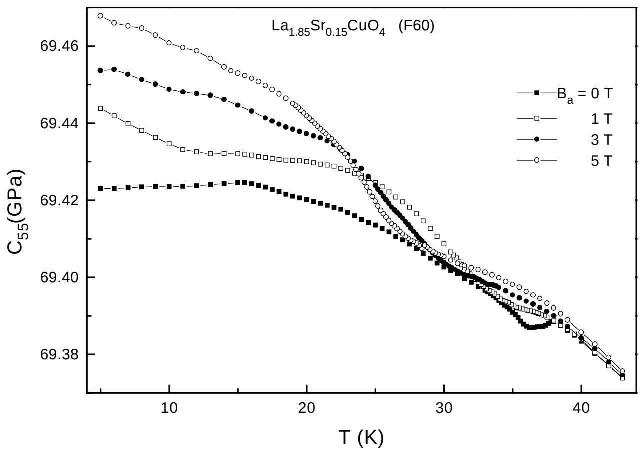

Figure 4.39: Measurements of C_{55} in magnetic fields from 0 to 5 T, parallel to the c-axis for the crystal F60. Apart from this the configuration is as in figure 4.37.

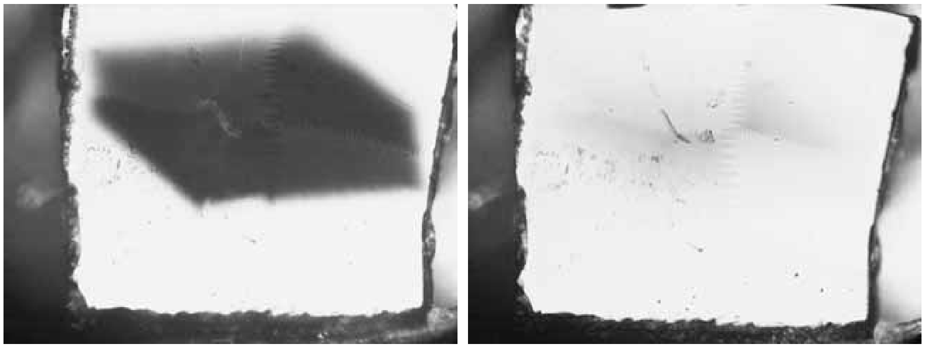

Figure 4.40: Magneto optical images of the crystal F40 with an applied field of 50 mT along the c-axis. The images have been taken at 18 K (left) and 35 K (right) respectively.

to the c-axis. Here the flux completely penetrates the sample already at 30 mT at this low temperature. As a comparison we measured the F60 crystal with the field parallel to the ab-planes. This is shown in figure 4.42 for the same fields and temperature as in figure 4.41. The c-axis goes vertically in the figure. The fields are not directly comparable in the last figures because of the anisotropy, but the sample characteristics are consistent. We are not able to really extract quantitative information about the differences between the two samples from this, but more emphazise that there are clearly differences. The MO-data have been taken at much lower fields, than the ultrasonic measurements, and with zero-field cooled samples. No detwinning were done in the susceptibility measurements nor in the MO-measurements.

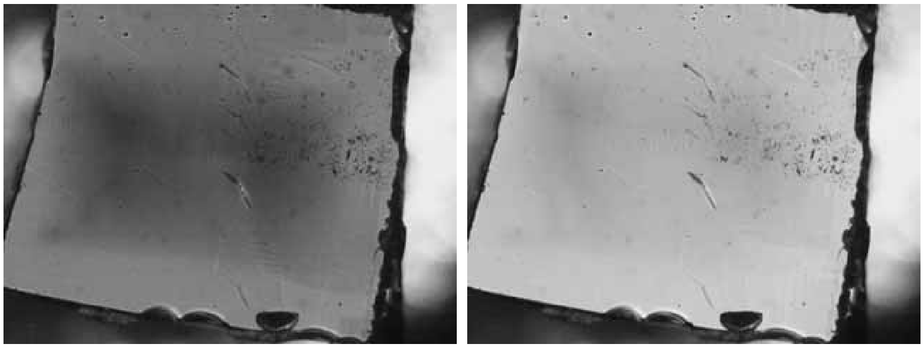

Figure 4.41: Magneto optical images of the crystal F60 measured at 18 K. The applied fields along the c-axis are 20 mT (left) and 30 mT (right).

From our experiences with the CW-method, our cryostat system and different crystals we feel that one should not take too much notice of all the features seen in the data. There were even cases when variations were bigger than the physical effects we are trying to measure. Reproducible behavier on the other hand should be considered ‘real’. In some way our resonant ultrasonic technique picks up some field dependent feature not seen in earliere measurements. What the effects could be due to may perhaps

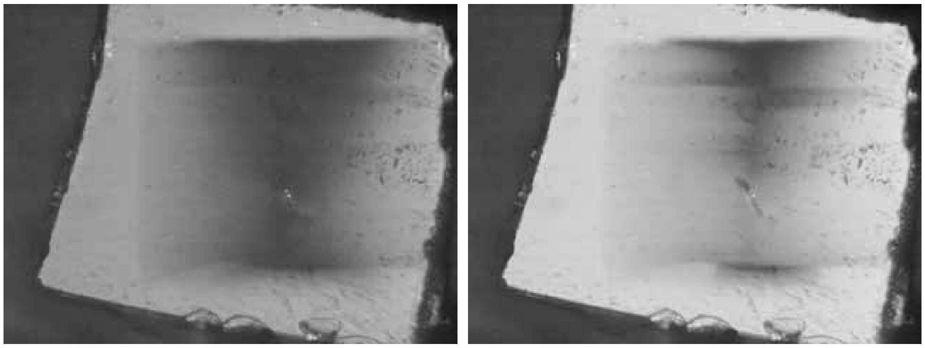

Figure 4.42: Magneto optical images of the crystal F60 measured at 18 K. The applied fields along the ab-planes are 20 mT (left) and 30 mT (right).

be seen in the theoretical work by Domínguez *et al.* [92, 93]. At low temperatures the Magnus force acting on vortices leads to a phenomenon called 'acoustic Faraday effect'. For standing wave resonances Domínguez *et al.* predict a splitting of resonaces of the order of 10 kHz for a field of 5 T, as T → 0. Other than this it appears to us that the predictions are very much the same as those by Pankert[40, 41]. We have observed a frequency shift typically of the order of 5 kHz, but we have no other indications which could link the data to these theories. There has been some controversy over the size of the acoustic Faraday effect[94], but no other evidence was presented. We will not speculate further on this point.

We had planned to finish this work by trying to measure c_{66}^h for the crystal F60. Due to the cutting, the crystal F40 could not be used. Technical problems made the attempt impossible, but we are not really convinced we could have been successful anyway. We have used long time to optimize the measurement system in order to get the needed resolution, but the real challange in measuring the shear modulus is acoustic of nature. With small crystals of too poor acoustic quality the measurements are impossible to do. We can not use the high resolution in frequency we have gained, because the reproducibility is not good enough. Measurements of c_{66}^h are also difficult because we need to subtract a background which is most probably different from the corresponding zero-field curve. Another dilemma is related to pinning. In order to have a strong coupling of the sound waves to the FLL the vortices need to be pinned. In order to measure a sharp change at the melting transition on the other hand, pinning should be more or less absent. The strong dapendence of pinning can be seen in the data by Fukase *et al.* [42], and from figure 4.43 (compared to figure 4.39) . When the pinning is small as in figure 4.43 the thermally assisted flux flow will smear ot the data in a large temperature range. When the pinning is strong the situation is opposite (see [42] figure 1).

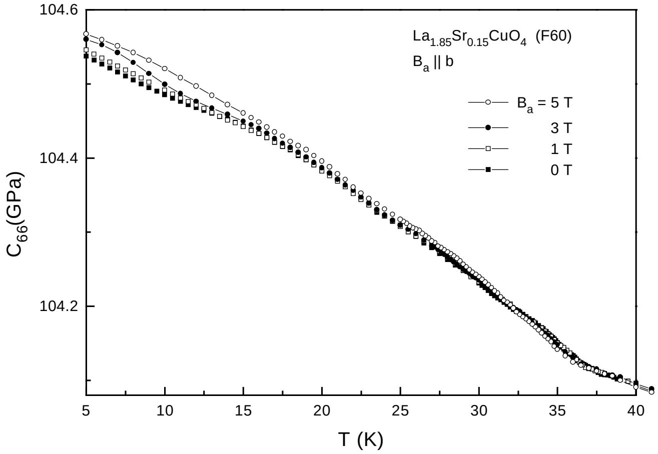

Figure 4.43: Measurement with configuration $C_{66} + c_{44,\|}$ for the crystal F60. The magnetic field is parallel to the b-axis of the crystal, $\vec{k} \parallel b$, and $\vec{u} \parallel a$.

Chapter 5

Conclusions

We will first look at the conclusions we can draw from the work on the method and our measurement system. After this we will sum up the measurements on LSCO.

We have built an ultrasonic measurement system for measurements at low temperatures in magnetic fields up to 5 T. We have used the continuous wave method developed by Bolef *et al.* [8], extending it to measurements on very small samples. We have calculated the resonant behavior of the ultrasonic composite also including attenuation (Q-value) and bonding in the model. Our TBSBT (Transducer-Bond-Sample-Bond-Transducer) calculations explain features not encountered by the linearized theory, with frequency pulling as the most apparent effect. The TBSBT theory can not easily be used for converting data from peak traces to elastic moduli due to the many parameters in the model and the coupling between them.

The apparatus we have build works very well, and has a frequency resolution of at least $\Delta f/f \sim 10^{-8}$. The resolution of the experiment is lower than this due to the crystal quality and the bonding. For our measurements on $La_{1.85}Sr_{0.15}CuO_4$ the resolution in the relative change of elastic moduli with temperature were $\Delta C_{ii}/C_{ii} \sim 10^{-4} - 10^{-6}$. The absolute accuracy is in the $1 - 3$ % range.

We have not been successful in doing measurements of attenuation, but have forseen many of the dangers with the method in doing so.

We have shown how the reflection method can be used in the case of a bond break or other causes of failure to clarify the problem.

Most of the samples we have had have either been too small or of too low acoustic quality for the measurements. The literature is also almost void of ultrasonic measurements on single crystalline high temperature superconductors. We have been able to investigate two optimally doped crystals of LSCO. The measurements of C_{33}, C_{44}, C_{55}, and C_{66} are consistent with similar published data measured on other LSCO crystals. Our crystals have been detwinned by a uniaxial stress of approximately 4 MPa applied along the tetragonal [110]-axis during the measurements. A distinct minimum near T_c is observed for the first time in our measurements of C_{44} and C_{55}. A minimum is also measured for C_{66} as observed earlier by Nohara *et al.*[22]. We ascribe the observed minimum to critical fluctuations.

We have done critical scaling of the C_{33} data and found consistency with 3D-XY critical exponents. The measured J-values are higher than what is measured for ^{4}He, and change with T_c. The variation is still within the range encountered by the 3D-XY model.

We have measured the modulus C_{33} in the frequency range from 16 - 214 MHz and found a signature of dynamic behavior near T_c. This behaviour has not been observed before and we belive more investigations could give valuable information about the physics of the phase transition.

For the low temperature behavior of C_{33} in field from 0 to 5 T we have observed an elastic softening, linear in the B-field. The phenomenon is not related to the elasticity of the FLL but might relate to the appearance of superconductivity. No distinct explanation of the effect have been found.

Attempts to measure the complete softening of the shear modulus c_{66}^h at the melting transition were unsuccessful. It is argued that this is impossible to measure in the crystals available up to now. Our measurements of the tilt modulus c_{44} are at temperatures near T_c consistent with published data and theories found in the literature. At low temperature the measurements consistently show an extra stiffness, but this is unexplainable by the linear elastic theory of the FLL. We have not been able to explain this feature.

Bibliography

[1] J. G. Bednorz and K. A. Müller, Z. Phys. B **64**, 189 (1986)

[2] G. Blatter *et al.*, Rep. Prog. Phys. **66**, 1125 (1994)

[3] E. H. Brandt, Rep. Prog. Phys. **58**, 1465 (1995)

[4] *Physics and Materials Science of Vortex States, Flux Pinning and Dynamics*, NATO Science Series Vol. **356**, 1999

[5] V. L. Ginzburg and L. D. Landau, Zh. Eksp. Teor. Fiz. **20**, 1064 (1950)

[6] J. Bardeen and J. R. Schrieffer in *Progress in Low Temperature Physics, vol III*, 170 (1961)

[7] Wu Ting and K. Fossheim, Int. J. Mod. Phys. B **8**, 275 (1993)

[8] D. I. Bolef and J. G. Miller, Physical Acoustics vol **VIII**, 95 (1971)

[9] H. Goldstein, *Classical Mechanics*, 2nd ed., Addison-Wesley Publishing Company Inc., 1980

[10] A. Migliori *et al.*, Physica B **183**, 1 (1993)

[11] A. Migliori and J. L. Sarrao, *Resonant Ultrasound Spectroscopy, Applications to Physics, Materials Measurements, and Nondestructive Evaluation*, John Wiley & Sons, Inc., 1997

[12] T. J. Moran and B. L*ü*thi, Phys. Rev. **187**, 710 (1969)

[13] T. Gotho *et al.*, The bulletin of the Research Institute for Scientific Measurements (Tohoku Univ., Sendai, Japan), Vol. 38, 65 (1989)

[14] C. Kittel, *Introduction to Solid State Physics*, 7th ed., John Wiley & Sons Inc., 1996

[15] J. Blitz, *Fundamentals of Ultrasonics*, 2nd ed., Butterworth & Co. Ltd., 1967

[16] G. L. Gooberman, *Ultrasonics, Theory and Applications*, English Universities Press Ltd., 1968

[17] Valpey Fisher: http://www.valpeyfisher.com/

[18] L. R. Testardi, Phys. Rev. B **12**, 3849 (1975)

[19] M. Nohara *et al.*, Phys. Rev. B **52**, 570 (1995)

[20] L. D. Landau and E. M. Lifshitz *Statistical Physics, Part 1*, 3rd ed., Pergamon Press Ltd, 1993

[21] A. J. Millis and K. M. Rabe, Phys. Rev. B **38**, 8908 (1988)

[22] M. Nohara *et al.*, Phys. Rev. Lett. **70**, 3447 (1993)

[23] D. M. Pozar, *Microwave Engineering*, John Wiley & Sons Inc., 1998

[24] D. I. Bolef, and M. Menes, J. Appl. Phys. **31**, 1010 (1960)

[25] D. I. Bolef, J. de Klerke, and R. B. Gosser, Rev. Sci. Inst. **33**, 631 (1962)

[26] R. G. Leisure, and D. I. Bolef, Rev. Sci. Inst. **39**, 199 (1967)

[27] R. L. Melcher, D. I. Bolef, and J. B. Merry, Rev. Sci. Inst. **39**, 1618 (1968)

[28] J. G. Miller, and D. I. Bolef, J. Appl. Phys. **39**, 4589 (1968)

[29] J. G. Miller, and D. I. Bolef, J. Appl. Phys. **41**, 2282 (1970)

[30] W. P. Mason *Electromecanical Transducers and Wave Filters*, van Nostrand, Princeton, 1934

[31] W. P. Mason *Piezoelectric Crystals and Their Applications to Ultrasonics*, van Nostrand, Princeton, 1950

[32] A. Sudbø and E. H. Brandt Phys. Rev. Lett. **66**, 1781 (1991)

[33] A. Sudbø and E. H. Brandt Phys. Rev. B **43**, 10482 (1991)

[34] E. Sardella Phys. Rev. B **45**, 3141 (1992)

[35] V. G. Kogan and L. J. Campbell, Phys. Rev. Lett. **62**, 1552 (1989)

[36] A. Sudbø and E. H. Brandt Phys. Rev. Lett. **68**, 1758 (1992)

[37] A. I. Larkin and Y. N. Ovchinnikov, J. Low Temp. Phys. **34**, 409 (1979)

[38] P. H. Kes *et al.* Supercond. Sci. Technol. **1**, 242 (1989)

[39] E. H. Brandt, Z. Phys. B **80**, 167 (1990)

[40] J. Pankert *et al.*, Phys. Rev. Lett. **65**, 3052 (1990)

[41] J. Pankert, Physica C **168**, 335 (1990)

[42] T. Fukase *et al.*, Physica B **216**, 274 (1996)

[43] D. R. Nelson, Phys. Rev. Lett. **60**, 1973 (1988)

[44] P. L. Gammel, L. F. Schneemeyer, J. V. Waszczak, and D. J. Bishop, Phys. Rev. Lett. **61**, 1666 (1988)

[45] A. Houghton, R. A. Pelcovits, and A. Sudbø, Phys. Rev. B **40**, 6763 (1989)

[46] W. K. Kwok *et al.*, Phys. Rev. Lett. **69**, 3370 (1992)

[47] Hui Wu, N. P. Ong, R. Gagnon, and L. Taillefer, Phys. Rev. Lett. **78**, 334 (1997)

[48] E. Zeldov *et al.*, Nature **375**, 373 (1995)

[49] A. Schilling *et al.*, Nature **382**, 791 (1996)

[50] M. Roulin, A. Junod, and E. Walker, Science **273**, 1210 (1996)

[51] A. Oral *et al.*, Phys. Rev. Lett. **80**, 3610 (1998)

[52] W. E. Lawrence and S. Doniach, in *Proc. 12th Int. Conf. Low Temp. Phys. Kyoto, 1970* E. Kanada ed., Keigaku, Tokyo 1971

[53] A. K. Nguyen *Phase Transitions in extreme type-II superconductors: Topological defects, and dual description of the vortex system* Thesis no. 56:1999, NTNU 1999

[54] A. K. Nguyen and A. Sudbø, EuroPhys. Lett. **46**, 780 (1999)

[55] A. K. Nguyen, A. Sudbø, and R. E. Hetzel, Phys. Rev. Lett. **77**, 1592 (1996)

[56] Z. Tešanović, Phys. Rev. B **51**, 16204 (1995)

[57] L. I. Glazman and A. E. Koshelev, Phys. Rev. B **43**, 2835 (1991)

[58] Z. Tešanović *et al.*, Phys. Rev. Lett. **69**, 3563 (1992)

[59] I. Tanaka and H. Kojima, Nature **337**, 21 (1989)

[60] Y. Maeno *et al.*, in Advances in Superconductivity **VI**, 103 (1994)

[61] S. Nakayama *et al.* Physica C **235-240**, 1283 (1994)

[62] F. Nakamura *et al.* Physica C **235-240**, 1285 (1994)

[63] T. Sasagawa *et al.*, Phys. Rev. Lett. **80**, 4297 (1998)

[64] T. Wolf *et al.*, J. Crystal Growth **96**, 1010 (1989)

[65] T. Wolf, J. Crystal Growth **166**, 810 (1996)

[66] Lei *et al.*, Jpn. J. Appl. Phys **30**, L1802 (1991)

[67] D. H. Ha *et al.*, Jpn. J. Appl. Phys **32**, L778 (1993)

[68] Ingun UK Ltd.: http://www.ingun.co.uk/

[69] V. K. Vlasko-Vlasov *et al.*, in *Physics and Materials Science of Vortex States, Flux Pinning and Dynamics*, NATO Science Series Vol. **356**, 205 (1999)

[70] E. H. Brandt, in *Physics and Materials Science of Vortex States, Flux Pinning and Dynamics*, NATO Science Series Vol. **356**, 81 (1999)

[71] T. Suzuki *et al.*, in *Mechanisms of Superconductivity*, JJAP Series **7**, 219 (1992)

[72] J. L. Sarrao *et al.*, Phys. Rev. B **50**, 13125 (1994)

[73] J. C. Le Guillou and J. Zinn-Justin, Phys. Rev. B **21**, 3976 (1980)

[74] J. A. Lipa *et al.*, Phys. Rev. Lett. **76**, 944 (1996)

[75] M. Lang *et al.*, Phys. Rev. Lett. **69**, 482 (1992)

[76] V. Pasler *et al.*, Phys. Rev. Lett. **81**, 1094 (1998)

[77] M. Nohara *et al.*, Physica C **235-240**, 1249 (1994)

[78] M. Nohara *et al.*, Physica B **194-196**, 2167 (1994)

[79] A. Junod, A. Erb, and C. Renner, Physica C **317-318**, 333 (1999)

[80] M. B. Salamon *et al.*, Phys. Rev. B **38**, 885 (1988)

[81] U. Welp *et al.*, Phys. Rev. Lett. **67**, 3180 (1991)

[82] B. Zhou *et al.*, Phys. Rev. B **47**, 11631 (1993)

[83] N. Overend, M. A. Howson, and I. D. Lawrie, Phys. Rev. Lett. **72**, 3238 (1994)

[84] I O. Jeandupeux *et al.*, Phys. Rev. B **53**, 12475 (1996)

[85] T. Schneider and J. M. Singer, Cond-mat/9911352 (1999)

[86] A. K. Nguyen and A. Sudbø, Phys. Rev. B **60**, 15307 (1999)

[87] K. Fossheim and R. M. Holt, Phys. Rev. Lett. **45**, 730 (1980)

[88] J. Wu *et al.*, Phys. Rev. B **47**, 2806 (1993)

[89] M. Cyrot and D. Pavuna, *Introduction to Superconductivity and High-Tc Materials*, World Scientific Publishing Co. Pte. Ltd., 1992

[90] J. C. Martinez *et al.*, Phys. Rev. Lett. **69**, 2276 (1992)

[91] A. S. Alexandrow and V. V. Kabanov, Cond-mat/9903071 (1999)

[92] D. Domínguez *et al.*, Phys. Rev. Lett. **74**, 2579 (1995)

[93] D. Domínguez *et al.*, Phys. Rev. B **53**, 6682 (1996)

[94] E. B Sonin, Phys. Rev. Lett. **76**, 2794 (1996)